

8-2017

Radioanalytical Methods for Characterization of the Surface Modification of Nanoparticles

Kathleen Davis

Clemson University, kathle5@g.clemson.edu

Follow this and additional works at: https://tigerprints.clemson.edu/all_dissertations

Recommended Citation

Davis, Kathleen, "Radioanalytical Methods for Characterization of the Surface Modification of Nanoparticles" (2017). *All Dissertations*. 1965.

https://tigerprints.clemson.edu/all_dissertations/1965

This Dissertation is brought to you for free and open access by the Dissertations at TigerPrints. It has been accepted for inclusion in All Dissertations by an authorized administrator of TigerPrints. For more information, please contact kokeefe@clemson.edu.

RADIOANALYTICAL METHODS FOR CHARACTERIZATION OF THE SURFACE
MODIFICATION OF NANOPARTICLES

A Dissertation
Presented to
the Graduate School of
Clemson University

In Partial Fulfillment
of the Requirements for the Degree
Doctor of Philosophy
Materials Science and Engineering

by
Kathleen Davis
August 2017

Accepted by:
Dr. O. Thompson Mefford, Committee Chair
Dr. Brian Powell
Dr. Igor Luzinov
Dr. Marek Urban
Dr. Christopher Kitchens

Abstract

The use of iron oxide nanoparticles for a variety of applications has grown over the past few decades. Manipulation of surface chemistry of these materials is critical to customizing the properties of the particles for desired applications. Ligand exchange is a common and versatile tool for surface modification. There are many factors which affect ligand exchange including ligand chain length, number of binding groups, binding group chemistry, and particle aging and oxidation. Furthermore, ligand exchange may not always occur to completion. Therefore, it is important to characterize the surface of the particles to determine the extent of exchange. Current techniques to confirm and monitor ligand exchange can be limited in sensitivity and versatility, and often these techniques must be used in combination to thoroughly characterize the exchange. To address this issue, radioanalytical techniques were developed to quantify ligand exchange on iron oxide nanoparticles and investigate the factors which affect ligand exchange. Oleic acid coated iron oxide nanoparticles were synthesized via thermal decomposition with trace amounts of ^{14}C -oleic acid on the surface. The particles were modified via ligand exchange with a variety of hydrophilic ligands. The modified particles were measured using liquid scintillation counting (LSC) to determine the activity and ultimately, the total number of ^{14}C -oleic acid chains remaining after exchange. These techniques were used to determine effects of head group chemistry with polymeric ligands and effects of head group chemistry, number of binding groups, and ligand exchange reaction parameters with small molecule ligands. Results revealed catechols displace the most oleic acid during exchange. Furthermore, multidenticity, or multiple binding groups, increases the

displacement of the oleic acid. Particle aging and oxidation was investigated using these techniques. Unlabeled, oleic acid coated particles which were aged in solution for 2, 7, and 30 days were mixed with ^{14}C -oleic acid in exchange reactions. Results revealed that aging of the particles at 30 days effected an increase in the amount of ^{14}C -oleic acid adsorbed on the particles after exchange. Kinetic analysis of these results indicated an increase in the desorption rate constant and a decrease in the adsorption rate constant with age but with no profound change in the overall reaction rates. A follow-up study with oxidized particles suggested that this behavior may be due to oxidation during aging. Overall, the results signify an increase in the number of available binding sites, possibly due to formation of a defective oxide shell during aging and/or oxidation.

Dedications

I would like to dedicate this dissertation to my friends and family without whom I would not be where I am today. Their support and guidance throughout my academic career has motivated me to pursue my interests in science. I would also like to dedicate this work to my grandfather, the late Selby Alsworth, and to the late Myree Cazentre. Their constant encouragement and belief in me has driven me towards achieving my goals in life.

Acknowledgements

First and foremost, I would like to thank my advisor Dr. Thompson Mefford for giving me the opportunity to work in his research group. His guidance and support has aided me in my endeavors to become a better researcher and scientist. I would not be where I am without his patience and commitment.

I would like to thank my committee members, Dr. Powell, Dr. Kitchens, Dr. Luzinov and Dr. Urban. They have contributed their time and expertise to help me learn and grow as a researcher. I would also like to extend a special thanks to Dr. Powell for allowing me to work in his lab and for helping me navigate the world of radiochemistry.

I am grateful to my lab mates Bin Qi, Roland Stone, Steven Saville, Akeem Cruickshank, Ben Fellows, and Michael Witmer. I would not have made it this far without their advice and support. Our collaboration and discussion of ideas, however ridiculous they were at times, was memorable and critical to me making it through grad school.

Finally, I would like to thank Kim Ivey for her expertise and assistance with my research and Dr. Gary Lickfield for his mentorship. Their technical skills and knowledge were invaluable to me. I enjoyed our many discussions on those long days of teaching lab.

Table of Contents

	page
ABSTRACT	ii
DEDICATIONS	iv
ACKNOWLEDGEMENTS	v
LIST OF FIGURES	x
LIST OF EQUATIONS	xvi
LIST OF TABLES	xvii
CHAPTER 1: INTRODUCTION: SYNTHESIS, SURFACE MODIFICATION, AND SURFACE CHARACTERIZATION OF IRON OXIDE NANOPARTICLES	
1	
1.1 INTRODUCTION	1
1.2 SYNTHETIC ROUTES FOR SYNTHESIS OF IRON OXIDE NANOPARTICLES	3
1.3 STRATEGIES FOR SURFACE MODIFICATION OF IRON OXIDE NANOPARTICLES	7
1.3.1 IMPACT OF SURFACE CHEMISTRY ON APPLICATIONS OF NANOPARTICLES	9
1.3.2 METHODS OF LIGAND EXCHANGE.....	13
1.3.3 FACTORS WHICH AFFECT LIGAND EXCHANGE	14
1.4 MECHANISMS OF LIGAND EXCHANGE.....	19
1.5 ANALYTICAL METHODS FOR SURFACE CHARACTERIZATION OF IRON OXIDE NANOPARTICLES	21
1.6 CONCLUSIONS AND FUTURE OUTLOOK.....	26
CHAPTER 2: DIRECT MEASUREMENT OF LIGAND EXCHANGE ON IRON OXIDES WITH POLYMERIC LIGANDS VIA RADIOANALYTICAL TECHNIQUES	28
2.1 INTRODUCTION	28
2.1.1 LSC THEORY	29

	page
2.2 EXPERIMENTAL.....	30
2.2.1 MATERIALS.....	31
2.2.2 NANOPARTICLE SYNTHESIS	32
2.2.3 POLYMER SYNTHESIS.....	33
2.2.4 LIGAND EXCHANGE	42
2.2.5 GEL PERMEATION CHROMATOGRAPHY (GPC) COLUMN	43
2.2.6 CHARACTERIZATION.....	44
2.2.7 CALCULATION OF OLEIC ACID SURFACE COVERAGE ON NANOPARTICLES.....	47
2.3 RESULTS AND DISCUSSION	48
2.3.1 TEM.....	48
2.3.2 DLS	50
2.3.3 TGA	52
2.3.4 VSM.....	57
2.3.5 LSC	58
2.3.6 GPC COLUMN.....	62
2.4 CONCLUSIONS.....	66
CHAPTER 3: DIRECT MEASUREMENT OF LIGAND EXCHANGE ON IRON OXIDES	
WITH SMALL MOLECULE LIGANDS VIA RADIOANALYTICAL	
TECHNIQUES.....	
	67
3.1 INTRODUCTION	67
3.2 EXPERIMENTAL.....	72
3.2.1 MATERIALS.....	72
3.2.2 RADIOLABELED NANOPARTICLE SYNTHESIS.....	72
3.2.3 SYNTHESIS OF ZWITTERIONIC DOPAMINE SULFONATE	73
3.2.4 LIGAND EXCHANGE WITH ZWITTERIONIC DOPAMINE SULFONATE	75
3.2.5 LIGAND EXCHANGE WITH APTES (PROCEDURE 1).....	76
3.2.6 LIGAND EXCHANGE WITH APTES (PROCEDURE 2).....	76
3.2.7 LIGAND EXCHANGE WITH CITRIC ACID	77
3.2.6 LIGAND EXCHANGE WITH DMSA AND 2-MERCAPTOETHANOL.....	77

	page
3.2.6 LIGAND EXCHANGE WITH CAFFEIC ACID.....	77
3.2.6 LIGAND EXCHANGE WITH PHOSPHONATE AND SULFONATE HEAD GROUPS	78
3.2.6 STANDARDIZED LIGAND EXCHANGE	78
3.2.6 CHARACTERIZATION	79
3.3 RESULTS AND DISCUSSION	82
3.3.1 TEM.....	82
3.3.2 DLS.....	82
3.3.3 ATR-FTIR	85
3.3.4 VSM.....	90
3.3.5 LSC	91
3.4 CONCLUSIONS.....	95

CHAPTER 4: THE EFFECT OF POST-SYNTHESIS AGING ON THE LIGAND

EXCHANGE ACTIVITY OF IRON OXIDE NANOPARTICLES..... 96

4.1 INTRODUCTION	96
4.2 EXPERIMENTAL	99
4.2.1 MATERIALS.....	99
4.2.2 NANOPARTICLE SYNTHESIS.....	99
4.2.3 AGING STUDY	100
4.2.4 KINETIC MODELLING.....	101
4.2.5 OXIDATION STUDY	104
4.2.6 CHARACTERIZATION.....	105
4.3 RESULTS AND DISCUSSION	108
4.3.1 TEM (AGING STUDY).....	109
4.3.2 TGA (AGING STUDY)	110
4.3.3 VSM (AGING STUDY).....	112
4.3.4 LSC (AGING STUDY)	113
4.3.5 KINETIC MODELLING.....	117
4.3.6 TEM (OXIDATION STUDY)	122
4.3.7 TGA (OXIDATION STUDY).....	123
4.3.8 LSC (OXIDATION STUDY)	124

	page
4.3.9 MÖSSBAUER SPECTROSCOPY.....	127
4.3.10 VSM (OXIDATION STUDY)	131
4.4 CONCLUSIONS.....	133
CHAPTER 5 CONCLUSIONS.....	135
CHAPTER 6 FUTURE WORK.....	138
6.1 FACTORS AFFECTING LIGAND EXCHANGE.....	141
6.2 RADIOLABELED POLYMERS.....	141
6.3 COLLOIDAL STABILITY STUDIES	142
6.4 OTHER METAL AND METAL OXIDE NANOPARTICLES.....	143
APPENDIX A	145
REFERENCES	166

List of Figures

	page
Figure 1.1 Schematic of ligand exchange. Represents a general ligand exchange reaction on the surface of a nanoparticle.	2
Figure 1.2 TEM images of iron oxide nanoparticles synthesized by (a) coprecipitation and (b) thermal decomposition. It can be seen that coprecipitation particles are more polydisperse than those synthesized via thermal decomposition.	4
Figure 1.3 Schematic of 1,3-dipolar cycloaddition of an alkyne and an azide resulting in the formation of a triazole.....	7
Figure 1.4 Representation of a general layer-by-layer deposition of polymers onto a nanoparticle.....	8
Figure 1.5 Illustration of ligands imparting a) colloidal stability and b) functionality to nanoparticles..	10
Figure 1.6 Illustration of colloidal stability through a) electrostatic forces and b) steric forces.....	12
Figure 1.7 Schematic of biphasic ligand exchange to modify nanoparticles.....	14
Figure 1.8 Illustration of factors which affect ligand exchange reactions of nanoparticles.	15
Figure 1.9 Illustration of common head groups for ligand exchange of iron oxides.....	16
Figure 1.10 Illustration of a) an associative ligand exchange mechanism and b) a dissociative ligand exchange mechanism.	20
Figure 2.1. Illustration of radioanalytical techniques to quantify ligand exchange.....	30

List of Figures (Continued)

	page
Figure 2.2 Modification of PEG with succinic anhydride.	35
Figure 2.3 Modification of PEG with NHS and nitroDOPA.	36
Figure 2.4 NMR spectra of a) PEG-COOH and b) PEG-nitroDOPA.	37
Figure 2.5 Modification of PEG-NHS with phosphonic acid.	38
Figure 2.6 Modification of PEG-NHS with L-DOPA.	39
Figure 2.7 NMR spectra of a) PEG-phosphonate and b) PEG-DOPA.	40
Figure 2.8 Synthesis and deprotection of PEG-amine.	41
Figure 2.9 NMR spectra of PEG-amine.	42
Figure 2.10 Illustration of a ligand exchange reaction. ¹⁴ C-oleic acid coated nanoparticles undergo a ligand exchange with one of the five monofunctional PEG ligands resulting in hydrophilic particles.	43
Figure 2.11 Nanoparticles passing through a GPC column.	44
Figure 2.12 TEM image (left) and size analysis (right) of the unlabeled nanoparticles (top) and the radiolabeled nanoparticles (bottom). The histogram shows the size distribution of the nanoparticles.	50
Figure 2.13 TGA curves of unlabeled, oleic acid coated nanoparticles a) before dialysis and b) after dialysis in chloroform.	54

List of Figures (Continued)

	page
Figure 2.14 TGA curves of unlabeled a) PEG-nitroDOPA modified nanoparticles and b) PEG-DOPA modified nanoparticles.	55
Figure 2.15 TGA curves of unlabeled a) PEG-phosphonate modified nanoparticles and b) PEG-COOH modified nanoparticles.....	56
Figure 2.16 TGA curves of unlabeled, PEG-amine modified nanoparticles.	57
Figure 2.17 Hysteresis loop of the unlabeled nanoparticles. Magnetic moment is measured in SI units of $A \cdot m^2/kg$ of magnetite as determined by ICP-MS.	58
Figure 2.18 Chains of oleic acid remaining on the surface of the nanoparticles before and after ligand exchange determined by LSC. The data for the PEG coated nanoparticles represent the amount of oleic acid remaining after dialysis.	61
Figure 2.19 TGA curves of unlabeled, oleic acid coated iron oxide nanoparticles a) passed through a GPC column and b) iron oleate precursor.....	64
Figure 3.1 Schematic of ligand exchange with small molecule ligands bearing different head groups.	68
Figure 3.2 Reaction scheme for synthesis of zwitterionic dopamine sulfonate.....	74
Figure 3.3 NMR spectra of a) dopamine sulfonate and b) zwitterionic dopamine sulfonate.....	75
Figure 3.4 TEM images (left) and histograms (right) of the unlabeled nanoparticles (a) and the radiolabeled nanoparticles (b).	82

List of Figures (Continued)

	page
Figure 3.5 ATR-FTIR spectra of nanoparticles modified using previously reported procedures for 2-aminoethylphosphonic acid, 2-mercaptoethanol, and APTES.....	87
Figure 3.6 ATR-FTIR spectra of nanoparticles modified using previously reported procedures for caffeic acid, the bisphosphonate ligand, and citric acid.	88
Figure 3.7 ATR-FTIR spectra of nanoparticles modified using previously reported procedures for the disulfonate ligand, ZDS, taurine, and DMSA.....	88
Figure 3.8 ATR-FTIR spectra of nanoparticles modified using a standardized procedure for DMSA, 2-aminoethylphosphonic acid, and citric acid.	89
Figure 3.9 ATR-FTIR spectra of nanoparticles modified using a standardized procedure for the disulfonate ligand, the bisphosphonate ligand, and caffeic acid.	89
Figure 3.10 ATR-FTIR spectra of nanoparticles modified using a standardized procedure for APTES, taurine, 2-mercaptoethanol, and ZDS.	90
Figure 3.11 VSM hysteresis loop of oleic acid coated, unlabeled nanoparticles.	91
Figure 3.12 Results of ligand exchange reactions using previously reported methods and a standardized procedure.....	93
Figure 4.1 TEM image (above) and histogram of size distribution (below) of different aged nanoparticles: a) nanoparticles aged 2 days b) nanoparticles aged 7 days c) nanoparticles aged 30 days.	110
Figure 4.2 TGA of aging study nanoparticles after initial purification.	111
Figure 4.3 TGA of aging study nanoparticles after GPC purification.....	112

List of Figures (Continued)

	page
Figure 4.4 VSM results of nanoparticles used for aging study.....	113
Figure 4.5 Amount of oleic acid (unlabeled and labeled) on the particles during exchange at different aging times and at a 1:1 molar ratio of oleic acid	114
Figure 4.6 Amount of oleic acid exchanged on the 2 days (a), 7 days (b), and 30 days (c) aged nanoparticles at all molar ratios and first-order fits to data. Green lines represent the 1:1 molar ratio, blue is 2:1, and red is the 3:1 molar ratio.	115
Figure 4.7 Amount of ^{14}C -oleic acid in solution during exchange with the 2 days, 7 days, and 30 days aged nanoparticles at a 1:1 molar ratio and model fits to the data.....	116
Figure 4.8 Amount of ^{14}C -oleic acid in solution during exchange with the 2 days, 7 days, and 30 days aged nanoparticles at a 2:1 and 3:1 molar ratio and model fits to the data.....	117
Figure 4.9 Linearized analytical solutions for 2 days, 7 days, and 30 days aged particles at a 1:1 molar ratio and the model fits based on linear regression analysis.....	119
Figure 4.10 Linearized analytical solutions for 2 days, 7 days, and 30 days aged particles at a 2:1 and 3:1 molar ratio and the model fits based on linear regression analysis..	119
Figure 4.11 Average, overall rate constants for particles aged for 2 days, 7 days, and 30 days.	121
Figure 4.12 TEM images (above) and histograms of size distributions (below) of a) unoxidized and b) oxidized nanoparticles.....	122

List of Figures (Continued)

	page
Figure 4.13 TGA results of unoxidized nanoparticles.....	123
Figure 4.14 TGA results of oxidized nanoparticles.....	124
Figure 4.15 Adsorption of ^{14}C -oleic acid onto the oxidized and unoxidized nanoparticles.	126
Figure 4.16 Loss of ^{14}C -oleic acid from the solution during exchange with the unoxidized and oxidized nanoparticles.....	126
Figure 4.17 Mössbauer spectral results of the unoxidized (b, c, and e) and the oxidized (a, d, f, g, and h) particles at 12 K.....	130
Figure 4.18 Mössbauer spectral results of unoxidized (a and c) and oxidized (b, d, e, and f) samples at 300 K.	131
Figure 4.19 VSM results of the unoxidized nanoparticles.....	132
Figure 4.20 VSM results of the oxidized nanoparticles.....	133
Figure 6.1 Exposure of sample to alternating magnetic field through copper coil. Setup for measuring specific absorption rate.....	140
Figure 6.2 Synthesis of radiolabeled PEG via anionic ROP of ethylene oxide with ^{14}C - labeled potassium methoxide.....	142

List of Equations

	page
Equation 1.1 Traditional DLVO theory equation	12
Equation 1.2 Extended DLVO theory equation	12
Equation 2.1 Calculation of moles of ^{14}C -oleic acid per milliliter of solution	47
Equation 4.1 Equation for reversible adsorption of ^{14}C -oleic acid on aged particles	101
Equation 4.2 Rate of change of ^{14}C -oleic acid in the liquid phase.	102
Equation 4.3 Equation describing concentration of [$^{14}\text{OA-np}$]	102
Equation 4.4 Equation to express reaction rate	102
Equation 4.5 Equation for equilibrium concentration of aqueous ^{14}C -oleic acid	103
Equation 4.6 Equations 4.4 and 4.5 combined	103
Equation 4.7 Final analytical solution.	103
Equation 4.8 Linear expression of analytical solution	103
Equation 4.9 Calculation of moles of ^{14}C -oleic acid/ml of solution	107

List of Tables

	page
Table 2.1 Hydrodynamic diameters and zeta potentials of the unlabeled and labeled modified and unmodified nanoparticles.	51
Table 2.2 Weight percent loss and corresponding grafting densities of nanoparticles obtained from TGA analysis.	53
Table 2.3 Weight percent loss and corresponding grafting densities of unlabeled, oleic acid coated nanoparticles obtained from TGA analysis and LSC results for radiolabeled, oleic acid coated nanoparticles to compare removal of excess oleic acid by dialysis and GPC.	62
Table 3.1 Ligand exchange procedures and references for the small molecule ligands. .	69
Table 3.2 DLS size and zeta results of nanoparticles modified using varied procedures.	84
Table 3.3 DLS size and zeta results of nanoparticles modified using a standardized procedure.	84
Table 3.4 ATR-FTIR results of nanoparticles modified using previously reported procedures and a standardized procedure.	86
Table 4.1 TGA results and surface coverages of nanoparticles used for aging study. ..	112
Table 4.2 Rate constants from exchange reactions as determined from modelling.	120
Table 4.3 TGA results and surface coverages of unoxidized and oxidized nanoparticles.	124
Table 4.4 Results of fitted Mössbauer spectra. The table contains values for the isomeric shift (IS), hyperfine interactions (HI), and the quadrupole splitting (QS).	128

List of Tables (Continued)

	page
Table 4.5 Compositions of representative oxidized and unoxidized nanoparticle samples as determined by Mössbauer spectroscopy.	129

CHAPTER 1: INTRODUCTION: SYNTHESIS, SURFACE MODIFICATION, AND SURFACE CHARACTERIZATION OF IRON OXIDE NANOPARTICLES

1.1 Introduction

Iron oxide nanoparticles have gained significant interest over the past few decades for use in environmental and biomedical applications. The magnetic properties and biocompatibility of these materials may be exploited for use in magnetic resonance imaging (MRI) contrast agents,^{1,2} magnetically modulated energy delivery (MagMED),^{3,4} drug delivery,^{5,6} and environmental remediation.^{7,8} Manipulation of surface chemistry of these nanoparticles is critical to achieve desirable properties for these applications.

There are various methods of synthesis and surface modification that allow for control over size, shape, hydrophilicity or hydrophobicity, chemical functionality, and colloidal stability of iron oxide nanoparticles.^{4,9} One synthesis method of particular interest is thermal decomposition of an iron precursor, which allows for optimal control over size and size distribution.¹⁰⁻¹² This method results in monodisperse particles with a hydrophobic surface. The hydrophobic ligands are often replaced with hydrophilic ligands through a process called ligand exchange to modify the nanoparticle surface.^{13,14}

There are multiple methods of nanoparticle surface modification. Some particle synthesis techniques allow for in-situ control of surface chemistry, while others may require a post-synthesis technique like ligand exchange (Figure 1.1) or multi-step techniques using a

grafting-to or grafting-from approach. Ligand exchange is a commonly used technique in which an initial or sacrificial ligand is displaced by another ligand which competitively binds to the surface of the particle.^{15, 16} This technique allows for change of the surface chemistry without compromising the integrity of the core particle. Ligands used for these reactions may be hydrophobic, hydrophilic, or ionic. The ligands may also bear multiple functional groups which allow for reactive chemistries or for binding to biomolecules. Furthermore, ligands may be used to control or manipulate particle size for certain applications. Ligand chemistry is key to influencing particle stability and interactions with the environment.

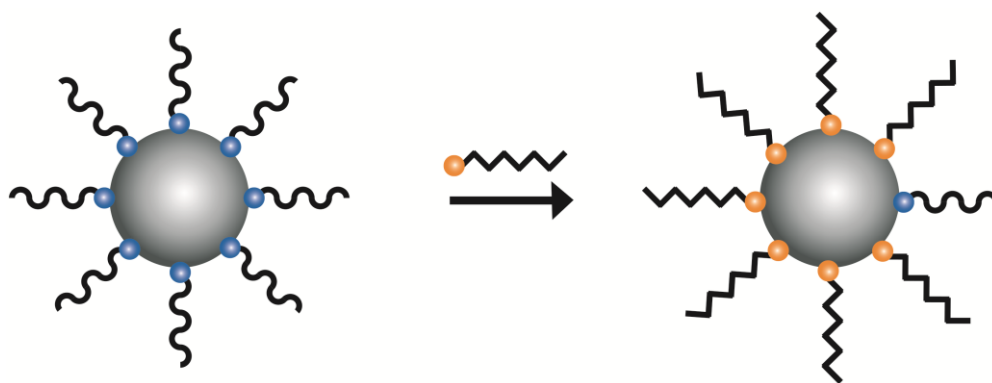


Figure 1.1. Illustration of general ligand exchange reaction on a nanoparticle.

Ligand exchange is dependent upon many factors. Ligand properties such as chain length,¹⁷ head group chemistry,¹⁵ charge,¹⁸ and tail group chemistry¹⁹ can greatly affect exchange and the rate of the reaction. Properties of the particle such as size, morphology, surface defects, and oxidation state may also affect binding and exchange of the ligands.^{20, 21} Several techniques exist which allow for analysis of ligand exchange and the factors which influence it. These techniques include thermogravimetric analysis

(TGA),^{22, 23} Fourier transform infrared spectroscopy (FTIR),^{22, 24} and x-ray photoelectron spectroscopy (XPS).^{25, 26} However, some of these techniques are limited to qualitative or semi-quantitative analysis only. Other techniques may have limited detection sensitivity. Therefore, it is prudent to develop a technique which allows for quantitative analysis of exchange with identifiable ligands at low detection limits. This dissertation focuses on the use of radioanalytical methods for investigation and quantification of ligand exchange of iron oxide nanoparticles and the factors that contribute to the reactions.

1.2 Synthetic Methods for Synthesis of Iron Oxide Nanoparticles

There are multiple approaches to synthesizing iron oxide nanoparticles. Some methods are beneficial due to ease of synthesis and greater control of surface chemistry during the reaction. Other methods allow for greater control of size and size distribution. However, each of these methods have drawbacks which can affect the properties of the particles and subsequent surface modifications. Coprecipitation is a common and easy route for synthesizing iron oxide nanoparticles (Fe_3O_4 and $\gamma\text{-Fe}_2\text{O}_3$).^{27, 28} This technique involves coprecipitation of ferrous and ferric salts in aqueous solutions at an adjusted pH.²⁹ Magnetite (Fe_3O_4) particles can be made using a stoichiometric ratio of 2:1 ($\text{Fe}^{3+}/\text{Fe}^{2+}$) in a pH range from 8 to 14.³⁰ The first synthesis of superparamagnetic iron oxide nanoparticles using co-precipitation was performed by Massart.³¹ Massart's work illustrated the importance of pH and the ratio of iron salts on size and size distribution of the particles. Furthermore, his work and the work of others has demonstrated the ability to synthesize coated particles with ligands such as dimercaptosuccinic acid (DMSA),^{32, 33}

citric acid,^{34, 35} and polymers like poly(ethylene glycol) (PEG)³⁶ and PEG-b-poly(vinyl phosphonic acid) (PVPA).³⁷ Despite ease of synthesis and in-situ control of surface chemistry, coprecipitation techniques do not typically yield particles with highly uniform size, shape, and size distribution.³⁸⁻⁴⁰ Figure 1.2 demonstrates the relatively high the polydispersity of co-precipitation particles.³⁶ Control of these particle properties is key for biomedical applications of iron oxides. High temperature methods like thermal decomposition offer size and size dispersity control.

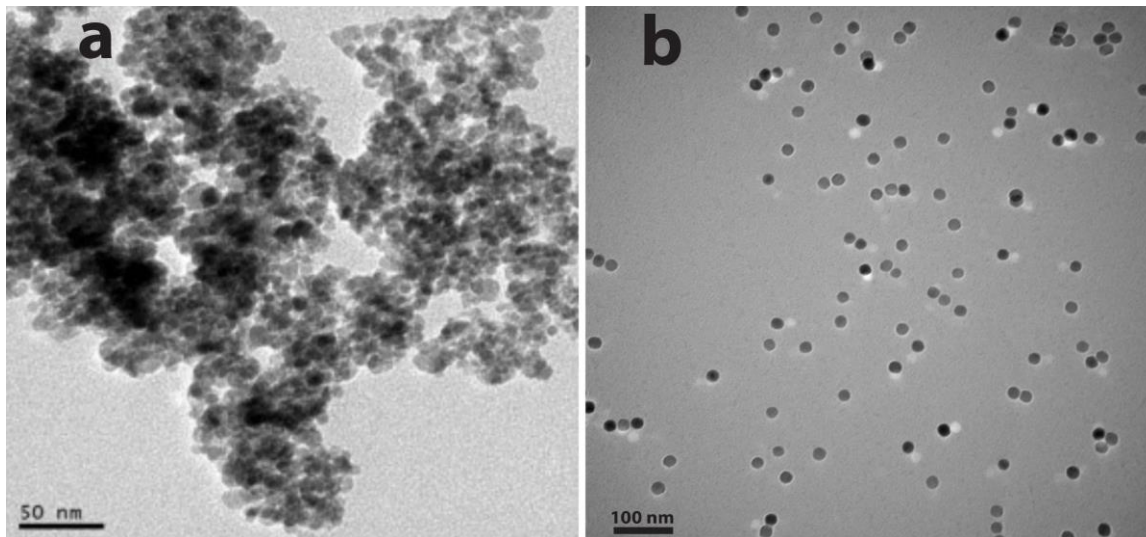


Figure 1.2. TEM image of iron oxide nanoparticles synthesized by a) coprecipitation³⁶ and b) thermal decomposition.

Thermal decomposition of an iron precursor is another common method which allows for greater control and tuning of particle size and size dispersity (Figure 1.2). Hyeon and coworkers synthesized monodisperse γ -Fe₂O₃ nanoparticles via subsequent oxidation of iron nanoparticles.⁴¹ They heated iron pentacarbonyl and oleic acid in octyl ether at 100°C for 1 hour, then oxidized the particles using trimethylamine oxide. This procedure

yielded monodisperse, spherical particles which could be tuned to sizes between 4 and 16 nm. Sun et al. utilized thermal decomposition to synthesize magnetite (Fe_3O_4) nanoparticles.⁴² Iron acetylacetonate was combined with oleic acid, oleylamine, and 1,2-hexadecanediol in phenyl ether and heated to reflux under nitrogen. The reaction resulted in particles which were 4 nm in diameter and were used in a seed-mediated growth method to create larger particles. The nanoparticles were characterized via transmission electron microscopy (TEM) and x-ray diffraction (XRD) and were shown to be highly monodisperse.

Park et al. demonstrated a larger scale synthesis of iron oxide nanoparticles using a two-step approach.⁴³ In their method, iron oleate was synthesized by mixing iron chloride (FeCl_3) and sodium oleate in ethanol, water, and hexane and heating the mixture to 70°C. The resulting precursor was purified, dried, and combined with oleic acid in octadecene. The dissolved precursor was then thermally decomposed at 320°C. This method was used to generate monodisperse particles of varying sizes between 5 and 22 nm in diameter. A group at Sandia National Laboratories has recently improved upon these methods and developed a more highly controlled and reproducible synthesis of magnetite nanoparticles.⁴⁴ Vreeland et al. first synthesized an iron oleate precursor by heating iron acetylacetonate and oleic acid in a molten metal bath to 320°C. The resulting precursor was adjusted to a concentration of 0.22 M using 1-octadecene. The precursor solution was then injected at a constant rate into a flask containing oleic acid and docosane which had been heated to 350°C under a nitrogen atmosphere. The particle size was tuned by

the duration of the reaction. The reproducible method allowed for synthesis of particles up to 34.5 nm in diameter with low standards of deviation as determined by TEM image analysis. Despite these remarkable advances in particle size tuning, thermal decomposition results in particles which are hydrophobic. The high temperatures necessitate the use of high-boiling, hydrocarbon solvents and ligands. Therefore, control of surface chemistry is only achieved after synthesis of the nanoparticles.

Hydrothermal techniques require high temperatures for synthesis but allow for direct formation of hydrophilic nanoparticles. Iron salts or hydroxides are heated to temperatures which can exceed 200°C and, therefore, are reacted at high pressures due to the necessity of a closed reactor.²⁹ Particle size and shape may be tuned by controlling solvent conditions, temperature and time of reaction,⁴⁵ and using additives like poly(vinyl alcohol)⁴⁶ or n-decylamine.⁴⁷

Sol-gel is a wet-synthesis technique for synthesizing nanoparticles in a network or gel. Typically, metal alkoxides are reacted with water to form metal hydroxides.²⁹ Then the metal hydroxides are condensed and polymerized with other metal hydroxides or alkoxides to form a 3-dimensional network or gel. The gels are then dehydrated by heat-treatment to obtain the nanoparticles.⁴⁸ Manipulation of temperature, precursor concentrations, and pH can result in formation of particles which are size-controlled and fairly monodisperse.⁴⁹

1.3 Strategies for Surface Modification of Iron Oxide Nanoparticles

Control of surface chemistry is key to tailoring the properties of nanoparticles for various applications. This can be achieved via several techniques including introduction of ligands in-situ,^{32, 34, 36} click chemistry,⁵⁰⁻⁵² layer-by-layer deposition,^{53, 54} ligand exchange,^{11, 12} and grafting-from approaches like, atom transfer radical polymerization (ATRP)⁵⁵⁻⁵⁸ and reversible addition-fragmentation chain-transfer polymerization (RAFT).^{51, 59, 60} As previously mentioned, co-precipitation of iron oxide nanoparticles allows for introduction of desired ligands in-situ. However, if greater control of particle size and shape uniformity is critical to the application, then other particle synthesis methods may be required necessitating the use of post-synthesis, surface modification techniques.

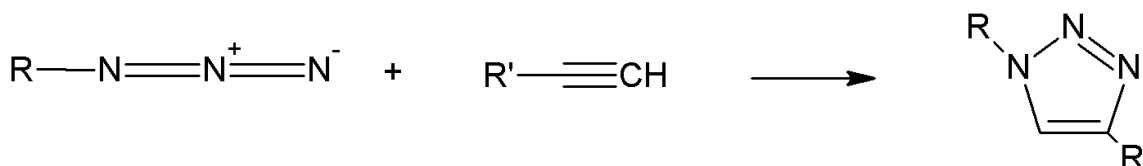


Figure 1.3. Schematic of 1,3-dipolar cycloaddition of an alkyne and an azide resulting in the formation of a triazole.

Click chemistry is a robust method which allows for fast and simple addition of functional ligands onto nanoparticles. Shao et al. utilized azide-alkyne click chemistry to modify polymer-coated iron oxide nanoparticles with carbohydrates.⁶¹ Dextran coated nanoparticles were synthesized via coprecipitation and were subsequently modified via perfluorophenylazide photochemically induced C-H insertion. Azide functional carbohydrates were clicked on to the nanoparticles and they were investigated for their

binding affinity to proteins and cells. Layer-by-layer (LbL) deposition is a slower, albeit effective method which allows for modification of particles with multiple layers through sequential adsorption of polymers with opposite charges (Figure 1.6).^{53, 62, 63} Choi and coworkers modified amine-functional iron oxide nanoparticles using a centrifugation layer-by-layer method for application as protein carriers.⁵³ The particles were either modified with poly(allylamine) hydrochloride and poly(acrylic acid), positive and negatively charged graphene oxides, or poly-L-lysine and hyaluronic acid. Characterization of the particles revealed successful depositions.

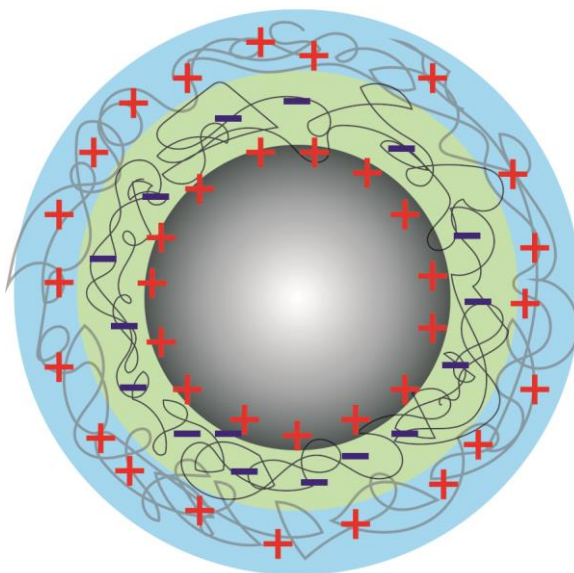


Figure 1.4. Representation of a general layer-by-layer deposition of polymers onto a nanoparticle.

Grafting-from approaches offer precise control of structure and chain length of ligands on the surface of nanoparticles. Polymers with specific architectures can be grown directly from the surfaces of particles via highly controlled syntheses. For example,

superparamagnetic iron oxide nanoparticles were modified by Eyiler et al. using surface-initiated ATRP.⁵⁵ Briefly, amine functional nanoparticles were reacted with bromopropionyl bromide. Itaconic acid and N-isopropylacrylamide were then copolymerized from the bromine-initiated nanoparticles. Results revealed successful modification of the particles with thermally and pH responsive copolymers.

Ligand exchange is a widely used and versatile technique for alteration of surface chemistry without affecting the particle size or shape.⁶⁴ Incidentally, this method is often used in combination with the aforementioned techniques.⁵⁷ Particles which were synthesized with oleic acid may need to be modified via exchange with a ligand which will serve as an initiator for polymerization or as a linker for other chemistries.⁵⁷ Prai-in and coworkers exchanged oleic acid with 3-aminopropyltriethoxysilane on the surface of iron oxide nanoparticles which allowed for further conjugation of block co-polymers containing azlactone rings which react with amines.⁶⁰ Ligand exchange can be performed in a variety of solvent systems and in the presence of catalysts or in high temperature conditions to enhance the rate of the reaction.⁶⁵⁻⁶⁸ Furthermore, exchange is heavily dependent upon the functionality of the ligands. The group which will bind to the particle must have a higher affinity than that of the initial ligand.

1.3.1 Impact of Surface Chemistry on Applications of Nanoparticles

Manipulation of surface chemistry of nanomaterials is important, and in many cases, required for generating materials which have all the necessary properties for desired applications. Ligands may be used to confer solubility, colloidal stability, and

functionality to the surfaces of nanoparticles (Figure 1.3). Ligands can be used to control hydrophilicity or hydrophobicity, charge, functional groups for reactive chemistries or adsorption, size, shape, and polydispersity. Control over the particle interface directly impacts its behavior in any environment.

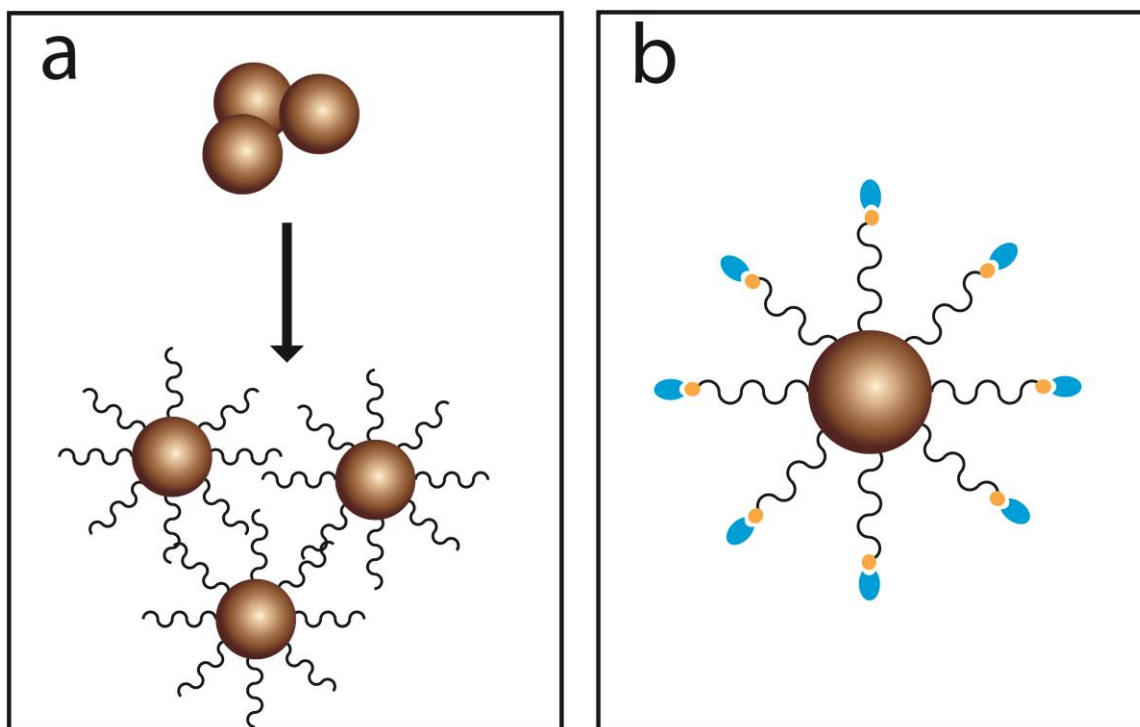


Figure 1.5. Illustration of ligands imparting a) colloidal stability and b) functionality to nanoparticles.

Oleic acid-coated iron oxide nanoparticles cannot be dispersed in aqueous environments for biomedical or environmental applications as synthesized. They must be modified with natural or synthetic hydrophilic ligands. Synthetic ligands such as poly(ethylene glycol) (PEG),^{69, 70} poly(vinyl alcohol) (PVA),⁷¹ poly(acrylic acid) (PAA),⁷² dimercaptosuccinic acid (DMSA),^{73, 74} and 3-aminopropyltriethoxysilane (APTES)⁷⁵ are commonly employed for biological applications and for environmental remediation.

PEG is particularly useful for these applications because it's biocompatible and helps to increase circulation time of therapeutic materials.^{76, 77} Natural ligands like citric acid,¹³ alginates,⁷⁸ natural organic matter (NOM),⁷⁹ and chitosan⁸⁰ have also been useful for modification of nanoparticles for biomedical and environmental applications. Surface ligands can also impart functionality and chemical reactivity to nanoparticles. As mentioned in a previous section, iron oxide nanoparticles can be functionalized for further polymerization from the surface. Polymers with functional tail groups like carboxylic acids and amines can be used to conjugate biomolecules which can then be used to target other moieties like cell receptor proteins.⁸¹ Nanoparticles may also contain ligands which adsorb environmental contaminants.⁷ Whatever the application may be, surface chemistry is critical to designing nanoparticles with the required properties.

Colloidal Stability

Surface ligands are not just important for solubility and functionality of nanoparticles; they also provide colloidal stability. Aggregation of particles can be detrimental to their purpose. Surface coatings can mediate this effect. The Derjaguin, Landau, Verwey and Overbeek (DLVO) theory is useful for modelling the interactions of particles in solution (i.e. colloidal stability).⁸² Traditional theory states interparticle interactions are governed by attractive forces or van der Waals forces (V_a) and repulsive forces or electrostatic forces (V_e). The interaction potential is determined by adding these forces together as shown in Equation 1.1.

$$\text{Eq. 1.1) } V_{total} = V_a + V_e$$

Particles with a surface charge attract counterions in the solution and layers of charges form. This is referred to as the electrical double layer. According to DLVO theory, stability can be achieved by balancing the double layer with attractive forces. However, this theory has since been modified to include steric repulsive forces (V_s) and magnetic interactions (V_m).⁸³⁻⁸⁶

$$\text{Eq. 1.2) } V_{total} = V_a + V_e + V_s + V_m$$

Ligands of sufficient size or length can provide enough steric hindrance to repel the particles and overcome the attractive forces. Steric and electrostatic repulsion can be achieved through surface modification (Figure). Ligands such as poly(acrylic acid), citric acid, and zwitterionic dopamine sulfonate can provide both steric and electrostatic stability. Polymers like PEG, which unless modified only provide steric stability, are useful because the molecular weight of the chains can be tailored to optimize the stability of particles of varying core sizes.

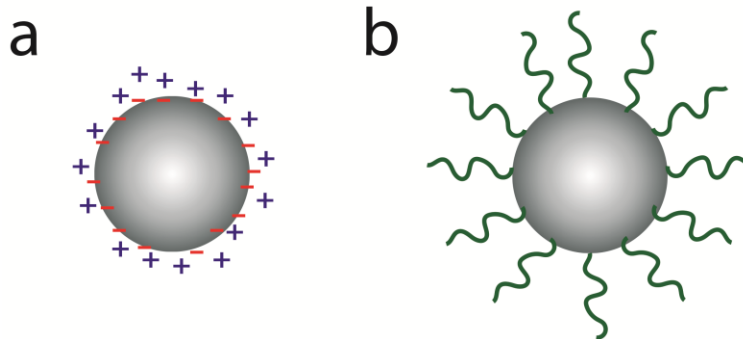


Figure 1.6. Illustration of colloidal stability through a) electrostatic forces and b) steric forces.

1.3.2 Methods of Ligand Exchange

There is no single method of ligand exchange that is used amongst all researchers. The ligand and the particle properties may even dictate the conditions of the ligand exchange. However, there are some general methods that apply to most ligand exchange reactions. Often, ligand exchange is performed in a homogeneous solution of either a single solvent or two miscible liquids.^{87, 88} The coated particles and the incoming ligand are combined in a medium which suits both. Ligand exchange reactions with oleic acid-coated particles may be done in organic solvents like chloroform, toluene, or dimethylsulfoxide (DMSO) depending on the solubility of the incoming ligand.^{15, 89, 90} The solutions of ligands and particles are mixed through some mechanical action for a given period of time. The particles may then be transferred to water after purification. These are common conditions for many ligand exchange reactions.

In some cases, the new or incoming ligand may not be soluble in the same solvent or one that is miscible with a solvent in which the particles are soluble. Therefore, a method referred to as biphasic ligand exchange may be necessary as shown in Figure 1.7. This method allows for a more direct transfer of the particles to the desired phase without the use of harsh solvents for purification.⁹¹⁻⁹³ Briefly, the particles are dispersed in either an aqueous or organic phase depending on the initial surface chemistry. The incoming ligand is dispersed in the opposite phase, and the two phases must be vigorously mixed for the duration of the exchange reaction. The particles will slowly migrate to the desired phase as they are coated with the new ligand. Phase transfer agents are sometimes used

to achieve this exchange. Solvents like acetone may be added to decrease surface tension at the interface of the phases.^{94, 95} Addition of acids or bases can alter the charge of the ligands or nanoparticle surfaces and thus the solubility of the ligands and nanoparticles.^{94, 96, 97} However, extra steps may need to be taken in order to remove these agents from the final particle solution.



Figure 1.7. Schematic of biphasic ligand exchange to modify nanoparticles.

1.3.3 Factors Which Affect Ligand Exchange

The ability to design and tune properties of ligands for optimal control of nanoparticle surface chemistry is advantageous. Ligand properties greatly impact ligand exchange reactions and their rates. Furthermore, solution conditions such as ionic strength and pH may impact the behavior of the ligands and whether or not they bind to the particles. Likewise, properties of the particle core can affect the nature of ligand binding. It is imperative that all of these factors be considered when modifying nanoparticles through ligand exchange (Figure 1.8).

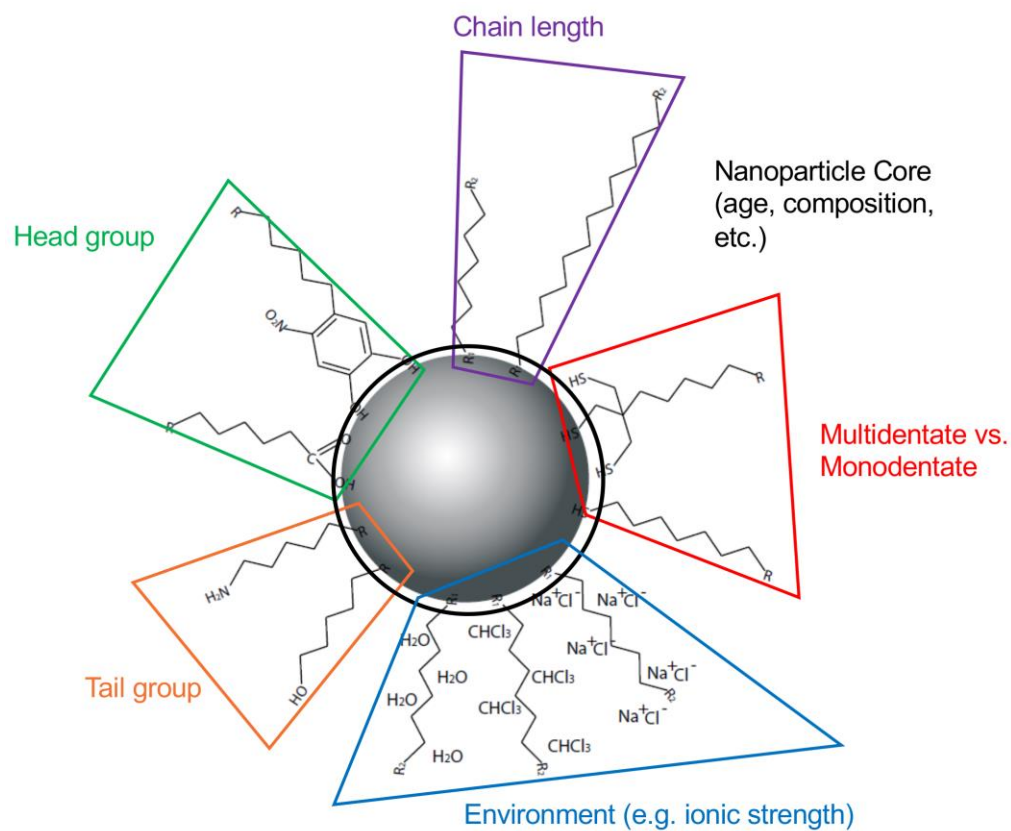


Figure 1.8. Illustration of factors which affect ligand exchange reactions of nanoparticles.

Head Group and Tail Group Chemistry

Selection of head group or binding group is key to controlling ligand exchange.

Functional groups such as carboxylic acids,⁹⁸ phosphonic acids,⁹⁹ catechols,^{100, 101} sulfonic acids,¹⁰² and silanes¹⁷ are widely investigated for their ability to bind to iron oxides. The affinity of these anchoring groups for the surface of iron oxide particles is critical to displacement of sacrificial ligands. Higher affinity anchoring groups will more

readily anchor to the surface of the particle and drive the exchange reaction in a favorable direction. Furthermore, these anchoring groups will not be as easily displaced by other incoming ligands. Works by Amstad et al. have shown the high binding affinity of catechol-derived anchoring groups for iron oxide surfaces versus other groups like carboxylic acids.¹⁰⁰ Furthermore, their work revealed that substitution of the catechols affects binding with nitrocatechols having higher affinity than dopamine and mimosine having such an affinity for iron oxide that it can cause dissolution of the particles.¹⁰³ These investigations demonstrate the importance of choosing the appropriate binding chemistry.

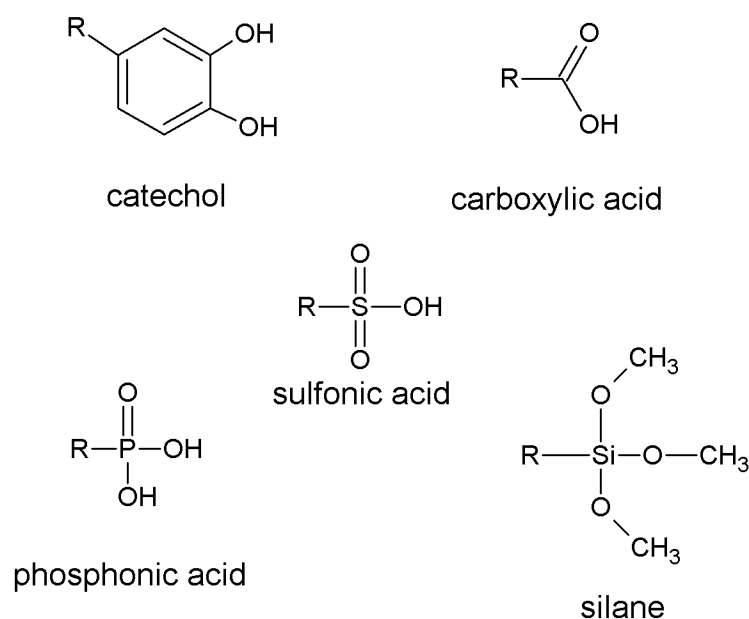


Figure 1.9. Illustration of common head groups for ligand exchange with iron oxides.

Although the impacts of end group chemistry on ligand exchange with iron oxides have not been widely studied, effects on ligand exchange with gold particles have been

investigated. End groups have been shown to impact rate of exchange depending on the electronic nature of the substituents. Guo and coworkers used nuclear magnetic resonance (NMR) spectroscopy to observe effects of NO₂, CH₃, and Br tail groups on ligand exchange with phenylethanethiolates.¹⁹ Results revealed that ligand binding was not affected by the tail group, but an activation barrier for initiation of exchange was dependent on this chemistry with NO₂-functionalized ligands exhibiting the highest rate of exchange. These findings could suggest that there are impacts of tail groups on other types of metal and metal oxide nanoparticles and should be further explored.

Multidentate Ligands, Chain Length, and Nanoparticle Environment

Not all ligands contain a single binding group. Some ligands have two or more head groups which can bind to nanoparticle surfaces and are referred to as multidentate. These types of ligands have been shown to bind more robustly than their monodentate counterparts. In a study by Zhang and Han, FTIR and TGA were used to confirm modification of iron oxide nanoparticles with two carboxyl-functional ligands. One of the ligands had two groups and the other had only one functional group.¹⁰⁴ Results revealed greater surface coverage and the distinct presence of the multidentate ligand compared to the monodentate version. A similar trend was seen by Miles et al. Their work studied the effects of multidenticity on the modification of iron oxide nanoparticles with PEO ligands which were anchored using a carboxylate group, an ammonium group, a zwitterionic ammonium phosphonate group, and their trifunctional counterparts.¹⁸ Results showed greater stability of the multidentate-stabilized nanoparticles in DI water.

Further studies in phosphate buffer saline (PBS) explored the nature of this enhanced stability and the effects of nanoparticle environment on exchange. The particles which were modified with the zwitterionic-anchored ligands showed the greatest stability in PBS. This was due to the ability of the phosphonate anchoring groups to compete with the phosphate salts in the medium for the surface of the particles. Furthermore, desorption of the multi-anchored ligands due to this competition was much slower owing to the increased number of binding groups per ligand. Introduction of sodium chloride into the solutions of zwitterionic-anchored nanoparticles in DI water prevented aggregation of the particles. This was attributed to a reduction in the “attractive electrostatic interactions” of the zwitterionic groups on the negatively charged particle surface. This work indicates not only the importance of multidenticity but also the influence of environmental conditions on the surface exchange and stability of nanoparticles.

The effect of chain length on ligand exchange of iron oxide nanoparticles can be largely attributed to enhanced colloidal stability with increasing chain length. This was evidenced by Barrera et al. in a study which looked at effects of increasing molecular weight of PEG-silane ligands.¹⁷ Stability studies using dynamic light scattering (DLS) showed aggregation of particles coated with 750 g/mol PEG versus those coated with 1000 g/mol, 2000 g/mol, and 5000 g/mol PEG ligands. They reasoned that the PEG 750 did contribute sufficient steric stabilization to overcome the attractive forces. Therefore, since ligand exchange occurs in solution it should follow that insufficient steric

stabilization could contribute to agglomeration of particles and thus, a less successful ligand exchange reaction.

Nanoparticle Age and Oxidation State

Again, the effects of particle aging and oxidation of iron oxide nanoparticles on ligand exchange are not widely understood. However, some studies of iron oxides and gold nanoparticles could suggest the impacts of these processes. Chechik et al. observed a decrease in ligand exchange reactivity of thiol-coated gold nanoparticles.¹⁰⁵ Analysis via TGA, UV-Vis, and electron paramagnetic resonance (EPR) confirmed that the thiols were bound more strongly to the aged particles resulting in a stabilization of defect sites where ligand exchange would normally occur. A study on aging of cobalt ferrite nanoparticles resulted in changing the Fe/Co cation distribution and the formation of an iron rich layer.¹⁰⁶ This caused in an increase in crystallinity of the particles. A change in metal ion distribution could result in an alteration of ligand binding due to selectivity of metals for certain anchoring groups. Amstad et al. observed selectivity based on oxidation state of iron.¹⁰⁷ In their study, EPR measurements revealed a preferential binding scheme of catechols to the Fe²⁺ oxidation state first then to the Fe³⁺ state. This suggests that oxidation could increase or decrease ligand exchange reactivity depending on the anchoring group.

1.4 Mechanisms of Ligand Exchange

Currently, understanding and agreement of a single ligand exchange mechanism of nanoparticles is debated amongst the scientific community. Some groups have reported associative (S_N2) mechanisms of exchange wherein an incoming ligand adsorbs or binds to the surface of the particle while, at the same time, an outgoing ligand is desorbed and leaves the surface (Figure 1.8a).^{108, 109} Others have reported dissociative (S_N1) mechanisms describing the desorption of the outgoing ligand before the adsorption of the incoming ligand can occur (Figure 1.8b)¹¹⁰ Furthermore, truly mechanistic studies of ligand exchange have been mostly limited to metal nanoparticles.⁶⁴

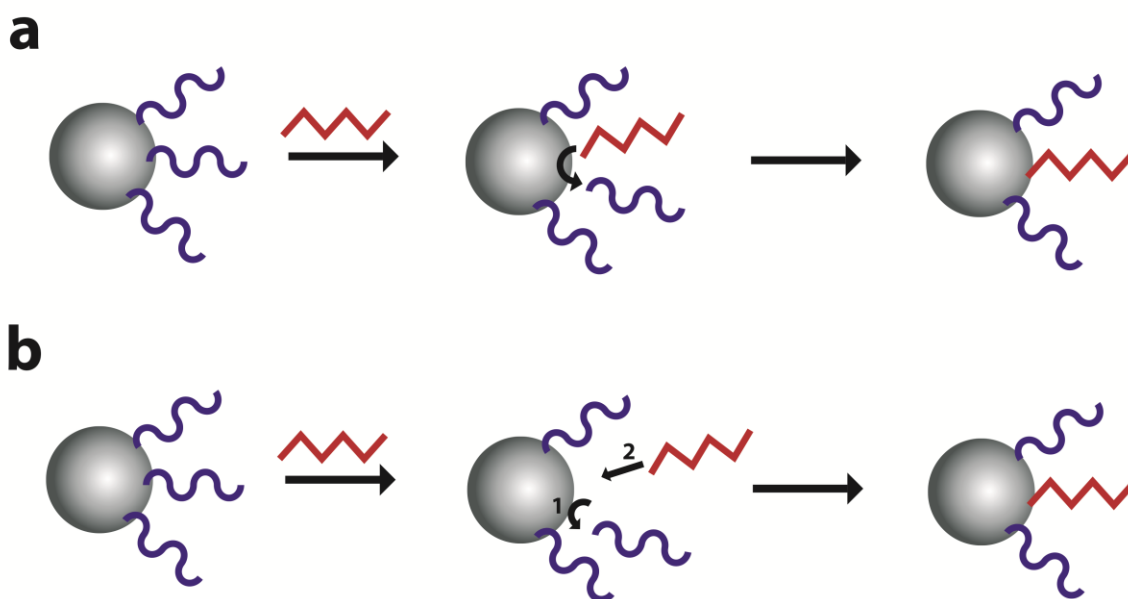


Figure 1.10. Illustration of a) an associative ligand exchange mechanism and b) a dissociative ligand exchange mechanism.

Despite a lack of research in mechanisms of ligand exchange of iron oxide nanoparticles, some groups have sought to understand mechanisms of exchange on metal (hydr)oxides, including hydrated iron complexes.¹¹¹ In these studies, ligand exchange occurs in two

steps. First, a weak and easily broken outer-sphere complex forms between the incoming ligand and the metal (hydr)oxide. Second, displacement of a water molecule in an inner coordination sphere allows for the incoming ligand to adsorb. In many cases this is considered to be a dissociative mechanism whereby the second step is the rate-determining step. Some researcher groups have shown that trivalent metal (hydr)oxides like $\text{Fe}(\text{H}_2\text{O})_6^{3+}$ exhibit selectivity towards certain incoming ligands resulting in an associative mechanism of exchange.^{112, 113} Selective binding of certain functional groups to iron and iron oxides has been well established and is a driving force of ligand exchange. Likewise, the binding affinity of the outgoing ligand may also affect the rate of exchange. For example, Tofan-Lazar and Al-Abadleh studied the effects of phosphate adsorption of iron (oxyhydr)oxide films with arsenic already adsorbed to the surfaces.¹¹⁴ They used an attenuated total reflectance-Fourier transform infrared spectrometer (ATR-FTIR) specially equipped with a flow through system to compare adsorption of phosphates on oxide surfaces which were coated with arsenate and surfaces which were coated with dimethylarsinic acid (DMA). A first-order, Langmuir adsorption kinetic model was used to fit their data. Results showed concentration dependent, phosphate adsorption rates on DMA coated films were up to 5 times higher than that of the arsenate coated films. They attributed this to the structure of the arsenate molecules and the ability for the ligands to leave. The methyl substitution of the DMA increased the proportion of weakly bonded complexes in the outer-sphere.

1.5 Analytical Methods for Surface Characterization of Iron Oxide Nanoparticles

Characterization of nanoparticle surface chemistry is important for confirmation of the presence of surface bound ligands and for better understanding the processes used to modify the particle surfaces. Analytical methods such as Fourier transform infrared spectroscopy (FTIR), thermogravimetric analysis (TGA), X-ray photoelectron spectroscopy (XPS), energy dispersive x-ray spectroscopy (EDX or EDS), ultraviolet-visible spectroscopy (UV-Vis), and fluorescence spectroscopy may be used to qualitatively or quantitatively characterize the surface of iron oxide nanoparticles. These methods are used to confirm ligand exchange took place, confirm extent of ligand exchange, determine kinetics of exchange, and observe binding of ligands. Each of these methods offer advantages over others, but also maintain some limitations. Often, these methods are used in combination to ensure a more complete analysis of the exchange.

FTIR

FTIR is a common method of characterizing surface modification of iron oxide nanoparticles.^{115, 116} This technique is often used to qualitatively confirm ligand exchange took place by identification of peaks due to key functional groups and identification of peak shifts due to ligand binding.^{117, 118} This technique may be used to monitor and quantify exchange reactions. As previously mentioned, Tofan-Lazar and Al-Abadleh used ATR-FTIR to observe kinetics of exchange. Guenin et al. utilized FTIR to determine surface coverage of a bisphosphonate ligand which was exchanged onto the surface of iron oxide nanoparticles.¹¹⁹ They normalized their spectra to the iron oxide vibration band at $500\text{-}600\text{ cm}^{-1}$ and utilized area measurements of the phosphonic

function vibration bands to ascertain the bisphosphonate ratio per particle. The difficulty with this method is that the iron oxide vibration band is not always easy to distinguish, and this method cannot be used for accurate quantification of ligand exchange with ligands of similar functionality due to peak overlap.

TGA

TGA is another common technique which is used to quantify modification of iron oxide nanoparticles.^{120, 121} TGA is used to measure the total mass loss of the organic material on the nanoparticles as the sample is heated. The mass loss can be used to further determine average surface coverage of the ligands on the nanoparticles. In one study, Durdureanu-Angheluta and coworkers utilized TGA to characterize organic mass loss on oleic acid-coated iron oxide nanoparticles which were modified in an exchange process with 3-aminopropyltriethoxysilane (APTES).¹²² They further characterized the particles using FTIR and XPS to identify the presence of the ligands on the particles. Combining characterization methods for analysis is common practice and often necessary due to a disadvantage of TGA. TGA is not a qualitative technique. This method does not allow for accurate distinction between different types of organic ligands present on the particles.

UV-Vis and Fluorescence Spectroscopy

UV-Vis is a less typical method of ligand exchange characterization. Iron oxide nanoparticles absorb in the UV-visible range making this method difficult for

characterization of ligands bound to the particles. However, this method can be used in cases where the ligands have been removed from the surface of the particles. For example, oleic acid-coated iron oxide nanoparticles were modified with tetraethylene glycol-based phosphonate ligands which were previously synthesized using click chemistry.¹²³ The ligand exchange was monitored using UV-Vis. The supernatant solutions generated from purification of the modified particles were analyzed to determine the quantity of the hydrophilic ligands which remained and were not exchanged onto the particles. The issue with this method is that it relies on ligands which exhibit signatures in the UV-Vis spectral range. The ligands in this study were synthesized using click chemistry which incorporated benzyl and triazole rings into the ligands.

Fluorescence spectroscopy is yet another technique which can only be used with ligands which exhibit unique spectral properties. This technique is used to monitor surface modification and ensure binding of ligands to the particles. Qu et al. utilized fluorescence spectroscopy to confirm modification with amine and carboxylic acid-capped iron oxide nanoparticles.¹²⁴ They conjugated fluorescein or rhodamine B to the functional ligands. Observed decreases in the quantum efficiency and lifetime of fluorescein after conjugation to citric acid-capped particles confirmed successful modification due to quenching from the covalent attachment of the fluorescein molecules. However, in order to determine the absorbance of the fluorescent molecule-conjugated nanoparticles, the particles had to be dissolved in hydrochloric acid. The poor optical properties of iron oxide nanoparticles make this technique more difficult for analysis of

ligand exchange. Another drawback of this method is the requirement of fluorescent molecules which may limit the available surface chemistries.

XPS and EDX

XPS and EDX are techniques which can be used to obtain elemental composition on the surface of iron oxide nanoparticles.^{125, 126} XPS measures kinetic energy and the number of electrons which are emitted after irradiation of the particle surface with an x-ray beam.¹²⁷ EDX or EDS measures x-rays emitted due to excitation of inner shell electrons.¹²⁸ De Palma and coworkers used XPS to characterize amino, carboxylic acid, and PEG-terminate silanes.¹¹⁶ They were able to determine elemental composition on the surface, thicknesses of the silane layers, and measure the binding energies of the ligands. The binding energies revealed the binding mechanisms or schemes of the functional groups to the iron oxide surfaces. These techniques can be combined with the other previously discussed methods to develop a more complete quantitative analysis of the particle surface. In one study EDS and TGA were used in combination to determine surface coverage of APTES-coated magnetite nanoparticles for further modification with polyamidoamine dendrimers.¹²⁹ Elemental analysis and mass loss from TGA measurements allowed for calculation of approximately 610 APTES ligands per nanoparticle. Despite the quantitative advantage of these techniques, they maintain some disadvantages. Techniques which rely on elemental analysis to identify surface ligands are highly sensitive to contaminants. EDX is limited due to spectral overlap of different

elements. Furthermore, elemental analysis alone may not be sufficient if multiple types of ligands are present on the surface.

1.6 Conclusions and Future Outlook

Ligand exchange is a widely applicable method of surface modification with iron oxide nanoparticles. This technique is critical for transforming hydrophobic particles to well-designed, hydrophilic particles for a variety of applications. Furthermore, characterization of the nanoparticles is imperative to qualitatively and quantitatively confirm the ligand exchange reaction occurred and to what extent. However, current characterization techniques are limited by detection sensitivity, limited to being only qualitative or quantitative, or limited by the available chemistries. Herein, radioanalytical methods for quantitative analysis of ligand exchange on iron oxide nanoparticles are described. The following chapters discuss the use of a radiotracer (^{14}C) to label nanoparticle ligands and radiometric detection of those ligands via liquid scintillation counting. Various factors which affect ligand exchange were investigated using these techniques. Chapter 2 includes studies of ligand exchange of radiolabeled, iron oxide nanoparticles with PEG ligands containing different head groups. Chapter 3 expands these techniques to investigations of ligand exchange with various small molecule ligands. Techniques commonly used with these ligands are compared to a standardized ligand exchange technique to isolate the contribution of head group chemistry on exchange. Chapter 4 contains a kinetic study of ligand exchange and discusses the effects of particle aging and oxidation on the exchange of oleic acid. Chapter 5 extends

the application of these radioanalytical techniques to the modification of drugs with radiolabeled polymers. LSC is a highly sensitive technique which can be used to detect even low levels of polymer-drug conjugate in a biodistribution study. Finally, this document will conclude with a discussion of future directions of this research.

CHAPTER 2: DIRECT MEASUREMENT OF LIGAND EXCHANGE ON IRON OXIDES WITH POLYMERIC LIGANDS VIA RADIOANALYTICAL TECHNIQUES

Reproduced with permission from [Davis, K.; Witmer, M.; Qi, B.; Powell, B. A.; Kitchens, C. L.; Mefford, O. T., Quantitative measurement of ligand exchange on iron oxides via radiolabeled oleic acid. *Langmuir* **2014**, *30*, 10918-10925.] Copyright [2014] American Chemical Society

2.1 Introduction

Control of surface chemistry and colloidal properties is critical for applications of iron oxide nanoparticles. Ligand exchange is a particularly useful tool for surface modification of these materials. Hydrophobic, iron oxide nanoparticles synthesized via thermal decomposition are not suitable for direct application in aqueous or biological media. The particles must be modified for transfer to water, and this is often done through ligand exchange with hydrophilic polymers. PEG is a commonly used ligand for coating iron oxide nanoparticles, especially for biomedical applications.^{17, 69, 130, 131} PEG has relatively high stability, water solubility, and low immunogenicity.^{76, 132, 133} Furthermore, it has been shown to enhance circulation time of biomolecules.^{77, 134, 135} Despite these advantages of PEG, if a full ligand exchange does not occur, the result is a heterogeneous mix of hydrophilic and hydrophobic patches on the surface of the nanoparticle, which can affect the colloidal stability of the particles in solution. Relatively little research has been done to quantify the amount of hydrophobic ligand that

is exchanged and determine the binding hierarchy of different ligands. Furthermore, typical methods for measuring ligand exchange such as FTIR, EDS, and TGA may not be sufficient for accurate quantification of exchange due to detection or sensitivity limits or inherent assumptions of complete exchange.

This chapter introduces radioanalytical methods, which we have previously published, to synthesize iron oxide nanoparticles with radiolabeled capping ligands and use liquid scintillation counting (LSC) to measure how much radiolabeled oleic acid has been displaced on the surface of the nanoparticles through exchange with a hydrophilic PEG ligand.¹⁵ Radiolabeled and unlabeled magnetite iron oxide core nanoparticles (Fe_3O_4) were synthesized with oleic acid as the capping ligand. During the synthesis of the radiolabeled nanoparticles unlabeled oleic acid and oleic acid [$1\text{-}^{14}\text{C}$] were added as to the reaction mixture. As illustrated in Figure 1, the labeled and unlabeled particles were then modified in chloroform with PEG ligands terminated with either a carboxylic acid group ($-\text{COOH}$), a nitroDOPA group, a DOPA group, a phosphonate group ($-\text{PO}(\text{OH})_2$), or an amine group ($-\text{NH}_2$) as the group that binds to the surface of the nanoparticle. The particles were purified to remove excess unbound ligands. The amounts of radioactive oleic acid in samples of each particle solution before and after ligand exchange were determined using LSC. The radiolabeled particles were further characterized by dynamic light scattering (DLS) and transmission electron microscopy (TEM). The unlabeled particles were synthesized and modified to compare LSC to other methods commonly used to characterize modified particles. The unlabeled particles were characterized by

dynamic light scattering (DLS), transmission electron microscopy (TEM), vibrating sample magnetometry (VSM), and thermogravimetric analysis (TGA).

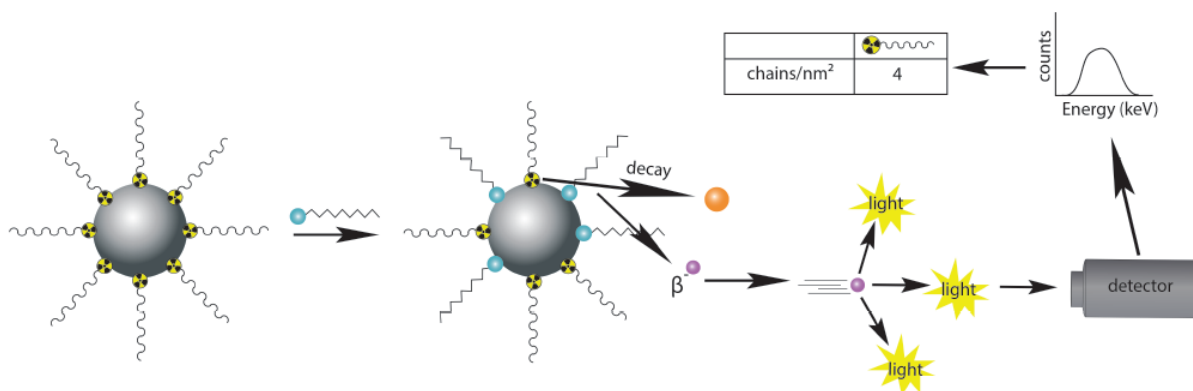


Figure 2.1. Illustration of radioanalytical techniques to quantify ligand exchange.

2.1.1 LSC Theory

LSC is a technique used to detect the presence of emitted low and high energetic beta particles and some alpha and gamma-ray emitters. This technique is used to determine activity of a radioactive sample and in some cases, can be used to identify an unknown radionuclide.¹³⁶ LSC works based on detection of photons generated from interactions of emitted particles with the surrounding liquid scintillation cocktail. Beta or alpha beta particles resulting from decay produce excited molecules in solution. The excited molecules either produce photons or transfer energy to an acceptor which will then emit photons.¹³⁷ The number of photons generated is dependent upon the number of excited molecules produced by the alpha or beta particles. The photons are detected by photomultiplier tubes which convert them to an electrical signal. Liquid scintillation counters can determine the number of photons generated over a specific amount of time

or counts per minute (cpm). These counts per minute can be converted to decays per minute (dpm) using a determined counting efficiency of the observed radionuclide.

Decays per minute can be directly related to activity.

Liquid scintillation cocktails are typically composed of aromatic organic solvents, surfactants or emulsifying agents, and fluorescent molecules or scintillators. While aromatic solvents may aid in the transfer of energy, fluorescent molecules such as 2-(4-*tert*-Butylphenyl)-5-(4-phenylphenyl)-1,3,4-oxadiazole (butyl-PBD) or p-terphenyl, act as efficient scintillators or acceptors in the solution.¹³⁷ Interaction of beta or alpha particles with the π cloud of an aromatic ring results in capture of the energy which can then be transferred to another solvent molecule or to a fluorescent molecule. This results in excitation of electron levels in the fluorescent. Photon emission from the scintillator molecule results from decay from the excited singlet state to the ground state.¹³⁷ This technique allows for sensitive detection of ionized particles due to the proximity and close interactions of the particles, solvents, and fluorescent molecules.

2.2 Experimental

2.2.1 Materials

Iron (III) chloride hexahydrate (ACS, 97, 0-102.0%), 3,4-dihydroxy-DL-phenylalanine (DL-DOPA; crystalline, 98%), and sodium nitrite ($\geq 97\%$) were purchased from Alfa Aesar. Poly(ethylene glycol) methyl ether (avg. Mn 5000), ethylene oxide monomer

($\geq 99.5\%$), 4-(dimethyl amino) pyridine ($\geq 99\%$), N-hydroxysuccinimide (98%), N,N'-dicyclohexyl carbodiimide (99%), potassium bis(trimethylsilyl)amide (95%; 1 M in THF), and succinic anhydride ($\geq 99\%$ (GC)) were purchased from Aldrich. (2-aminoethyl) phosphonic acid (99%), dimethylformamide (99.8%, extra dry over molecular sieves, AcroSeal®), and 1-octadecene (90%, technical grade) were purchased from Acros Organics. Ethyl ether ($>95\%$) and chloroform (CHCl_3 , 99.8%) were purchased from Avantor™ Performance Chemicals. Ethanol (anhydrous, histological grade) and hexanes (99.3%) were purchased from Fisher Chemical. Oleic acid was purchased from EMD. Tetrahydrofuran (99%) was purchased from BDH chemicals. Sodium oleate ($\geq 97\%$) was purchased from TCI America. Optiphase 'HISAFE' 3 liquid scintillation cocktail and oleic acid [$1\text{-}^{14}\text{C}$] ($>97\%$) were purchased from PerkinElmer. Bio-Beads™ SX-1 support (styrene-divinylbenzene copolymer beads) were purchased from Bio-Rad Laboratories, Inc.

2.2.2 Nanoparticle Synthesis

In order to synthesize oleic acid coated Fe_3O_4 nanoparticles for ligand exchange that were approximately 10 nm in diameter, we modified a procedure reported by Park et al.⁴³ The procedure was performed twice in order to synthesize radiolabeled and unlabeled particles separately. To synthesize the iron oleate precursor 0.811 g (5 mmol) of FeCl_3 , 4.56 g (15 mmol) of sodium oleate, 10 mL of ethanol, 7.5 mL of DI water, and 17.5 mL of hexane were added into a three-neck, round bottom flask. The reaction mixture was stirred via a magnetic stir bar as the solution was heated to 60 °C at 5 °C/min and

refluxed for four hours. The top, organic layer containing the iron oleate was washed with DI water.

To synthesize the Fe₃O₄ nanoparticles the iron oleate precursor (5 mmol, assuming 100% conversion), 2.5 mL of oleic acid, and 50 mL of octadecene were added to a three-neck, round bottom flask. To synthesize the ¹⁴C-oleic acid coated Fe₃O₄ nanoparticles, 50 μCi of ¹⁴C-Oleic acid was added during this step. Given the high concentration of stable oleic acid, the ¹⁴C-oleic acid serves as a tracer and does not significantly add to the total mass of oleic acid in the system. The reaction mixture was stirred via a magnetic stir bar and heated to 110°C at 5 °C/min and held at that temperature for one hour. The reaction was then heated at 3 °C/min to 320 °C and held to reflux for two hours. The resulting nanoparticles were washed 5 times with ethanol and hexane then dispersed in chloroform. Some of these nanoparticles were injected into 12,000-14,000 MWCO Spectra/Por® dialysis tubing, placed in chloroform, and put on a shake plate to stir for 72 hours. The amount of ¹⁴C-oleic acid was monitored in each purification step using LSC.

2.2.3 Polymer Synthesis

In this study a series of five, modified poly(ethylene glycol) (PEG) polymers were synthesized for use in the ligand exchange with oleic acid on the surface of the nanoparticles. The structures of these polymers are shown in Figures 2.2, 2.3, 2.5, 2.6, and 2.8. Two catechol-derived anchor groups, DOPA and nitroDOPA, were of particular interest to this study as they have been shown by Amstad et. al. to bind with great affinity to iron oxide nanoparticles.^{100, 107} Results from these studies on various catechol groups

indicated strong, irreversible binding of nitroDOPA to iron oxide thus providing good colloidal stability of the nanoparticles. The nitroDOPA was bound strongly to the surface but not with an affinity so high to cause dissolution of the nanoparticles as with the mimosine. These polymers and a carboxylic acid terminated PEG polymer were synthesized according to previously published procedures.¹⁰¹ A phosphonate terminated PEG was synthesized by a modified version of those published procedures. An amine terminated PEG was synthesized according to a procedure reported by Stone et al.¹³⁸ Following synthesis each polymer was purified by vacuum filtration. The polymers were further purified 3 times each by precipitation in ethyl ether, re-dispersion in chloroform, and isolation by centrifugation at 10,000 rpm. The polymers were dried at room temperature in a vacuum oven at 30 in.Hg (14.7 psi) overnight to remove solvent. A carboxylic acid (-COOH) terminated PEG polymer was synthesized by first drying 5 g of poly(ethylene glycol) methyl ether (avg. M_n 5000) in an Erlenmeyer flask in a vacuum oven at 80°C overnight. The polymer was then dissolved in 20 mL of tetrahydrofuran (THF) and reacted with succinic anhydride in a 1:1.5 molar ratio of PEG to succinic anhydride (Figure 2.2). 4-(dimethyl amino) pyridine was used as a catalyst in a 1:0.01 molar ratio of PEG to 4-(dimethyl amino) pyridine. The solution was stirred via a magnetic stir bar for eight hours and was purified by the aforementioned procedure. Polymer modification was verified by nuclear magnetic resonance (NMR) spectroscopy by peaks at 2.65 ppm ($O=C-CH_2-CH_2-C=O$, addition of succinic anhydride), 3.4 ppm ($O-CH_3$, methoxy end group), 3.67 ppm ($O-CH_2-CH_2-O$, PEG).

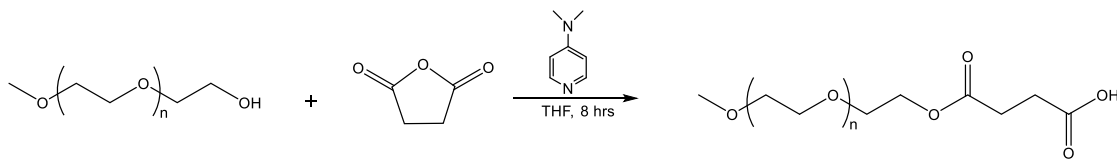


Figure 2.2. Modification of PEG with succinic anhydride.

A nitroDOPA terminated PEG polymer (5000 MW) was synthesized from the previously synthesized PEG-COOH (Figure 2.3). The dried PEG-COOH polymer was dissolved in 20 mL of anhydrous THF and reacted with N-hydroxysuccinimide (NHS) in a 1:1 molar ratio. N,N'-dicyclohexyl carbodiimide (DCC) was used as a catalyst in a 1:1.25 molar ratio of PEG-COOH to DCC. The solution was stirred via a magnetic stir bar for four hours. The resulting PEG-NHS product was filtered by vacuum filtration. The collected filtrate was rotary evaporated, precipitated with ethyl ether, centrifuged, and left to dry in a vacuum oven overnight. The dried polymer was dissolved in 20 mL of dry dimethylformamide (DMF). The DMF was dried over molecular sieves prior to dissolving the polymer. NitroDOPA was added to the polymer solution in a 1:1.5 molar ratio of PEG-NHS to nitroDOPA. The solution was stirred via a magnetic stir bar overnight and purged with nitrogen for the first ten minutes of the reaction. The final product was purified before use. NMR was used to verify the polymer modification by peaks at 2.65 ppm (O=C-CH₂-CH₂-C=O, addition of succinic anhydride), 2.88 and 2.95 ppm (CH₂-CH₂, DOPA), 3.4 ppm (O-CH₃, methoxy end group), 3.7 ppm (O-CH₂-CH₂-O, PEG), 8.0 ppm (CH, ring, DOPA).

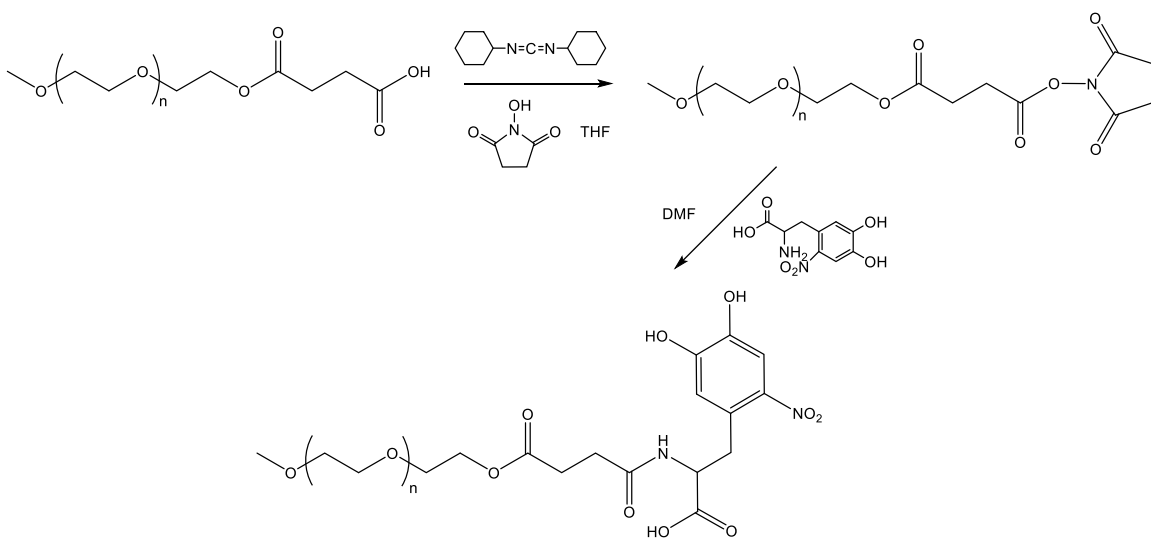


Figure 2.3. Modification of PEG with NHS and nitroDOPA.

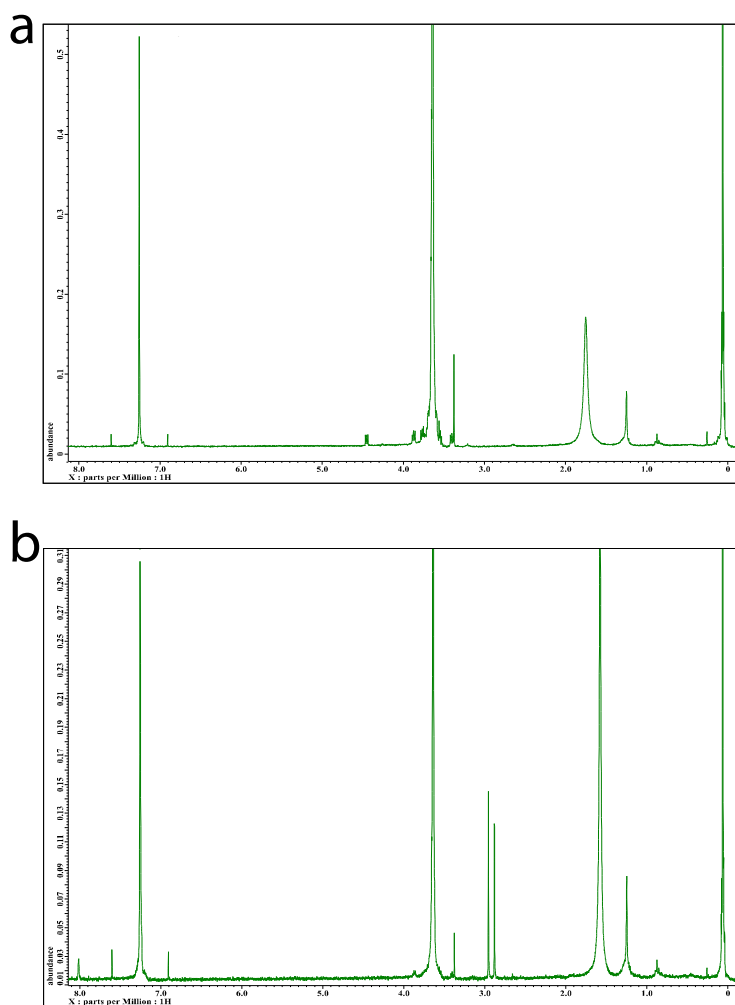


Figure 2.4. NMR spectra of a) PEG-COOH and b) PEG-nitroDOPA.

The nitroDOPA utilized in the PEG-nitroDOPA synthesis was synthesized prior to polymer synthesis. First, a 250 mL round bottom flask containing 100 mL of DI water and a magnetic stir bar was placed in an ice bath at 0 °C. 1.97 g (9.99 mmol) of DL-DOPA was added to the flask as the solution stirred. Following that, 1.52 g (17.88 mmol) of sodium nitrite was added to the flask while stirring. 0.92 mL of sulfuric acid (96 wt%) in 10 mL of DI water was added dropwise to the mixture via an additional funnel until it became a yellow, golden color. The resulting product was vacuum filtered

and washed with water and methanol to remove impurities. The product was dried in a vacuum oven.

The first two steps of the synthesis of a phosphonate terminated PEG were the same as those for the synthesis of the nitroDOPA terminated PEG. The previously synthesized PEG-NHS polymer was reacted with (2-aminoethyl) phosphonic acid in a 1:1 molar ratio of PEG-NHS to acid (Figure 2.5). The reaction occurred in DI water with a pH adjusted to seven by addition of NaOH. The solution was stirred via a magnetic stir bar for four hours. The resulting solution was poured into a separatory funnel. DI water was added to the separatory funnel in a 1:1 volume ratio of polymer solution to water. The mixture was allowed to sit overnight and the bottom layer containing the polymer was collected, precipitated with ethyl ether, centrifuged, and dried in a vacuum oven overnight. The polymer modification was verified with NMR by peaks at 1.9 ppm ($\text{CH}_2\text{-P(=O)(OH)}_2$), 2.7 ppm ($\text{O=C-CH}_2\text{-CH}_2\text{-C=O}$, addition of succinic anhydride), 4.15 ppm (HO-), 3.4 ppm (O-CH_3 , methoxy end group), 3.7 ppm ($\text{O-CH}_2\text{-CH}_2\text{-O}$, PEG).

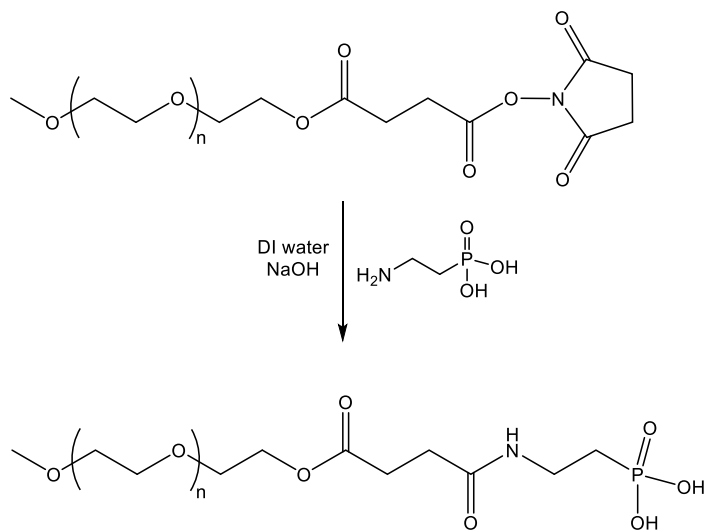


Figure 2.5. Modification of PEG-NHS with phosphonic acid.

Again, the first two steps of the synthesis of a L-DOPA modified PEG were the same as those for the synthesis of PEG-nitroDOPA and PEG-phosphonate. The previously synthesized PEG-NHS polymer was reacted with 3,4-dihydroxy-phenylalanine in a 1:1 molar ratio of PEG-NHS to L-DOPA (Figure 2.6). The reaction was performed in 20 mL of dry DMF which was purged with nitrogen for the first ten minutes of the reaction. The solution was stirred via a magnetic stir bar for 8 hours and purified after reaction. The polymer modification was verified using NMR by peaks at 2.65 ppm (O=C=CH₂-CH₂=C=O, addition of succinic anhydride), 2.9 and 2.95 ppm (CH₂-CH₂, DOPA), 3.4 ppm (O-CH₃, methoxy end group), 3.65 ppm (O-CH₂-CH₂-O, PEG), 8.0 ppm (CH, ring, DOPA).

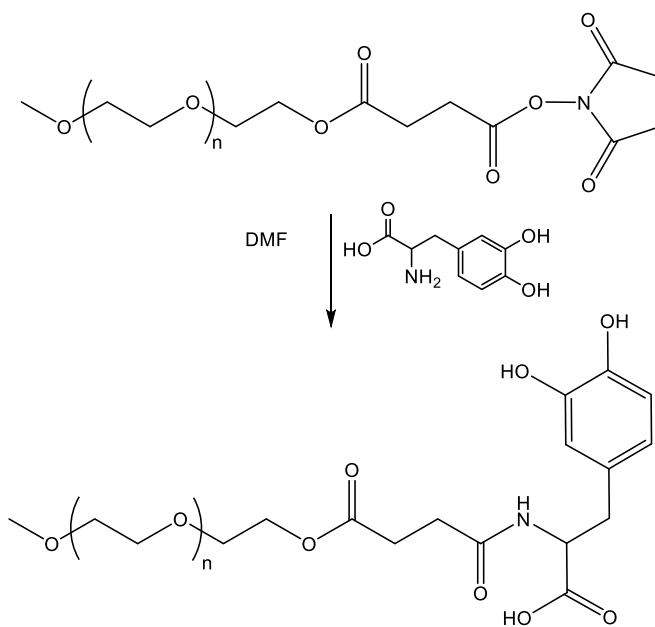


Figure 2.6. Modification of PEG-NHS with L-DOPA.

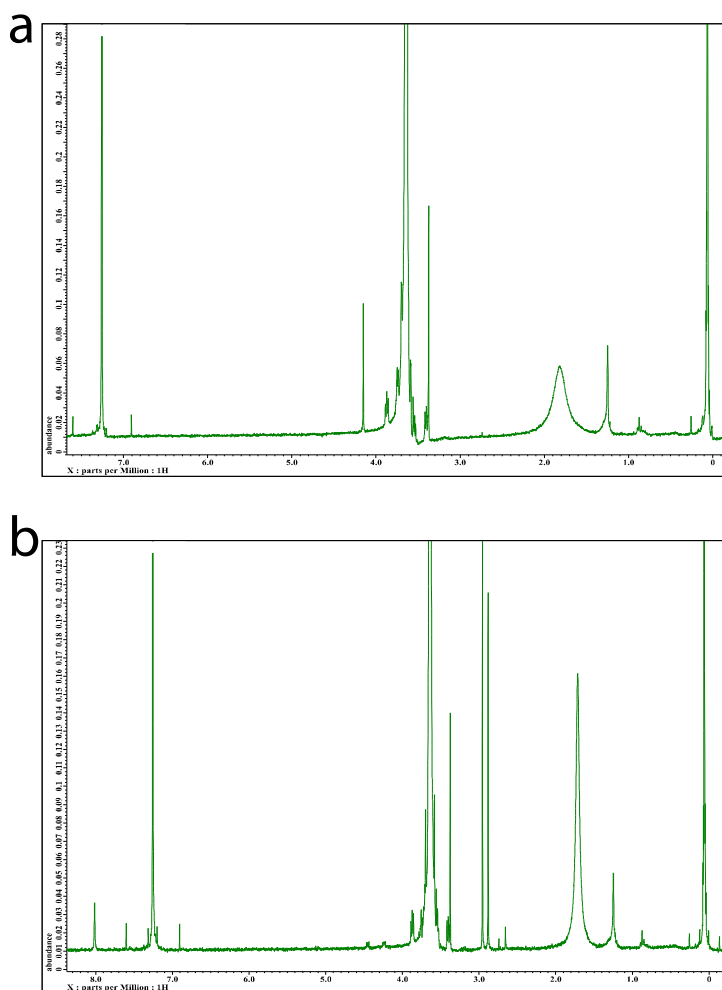


Figure 2.7. NMR spectra of a) PEG-phosphonate and b) PEG-DOPA.

A protected, NH_2 terminated poly(ethylene oxide) (PEO) polymer with a molecular weight of 5,000 g/mol was synthesized via anionic polymerization using a high pressure, stirred, model 4566 mini bench top Parr reactor to create a closed, oxygen and water free environment (Figure 2.8). First, the reactor was purged and vacuum was pulled three times. The temperature of the reactor was lowered to -35°C using acetone and liquid nitrogen. At this low temperature 8.61 g (195.46 mmol) ethylene oxide (EO) was distilled into the reactor. Tetrahydrofuran (THF, 110 mL) was added via syringes to the

reactor and the solution began stirring. At approximately 40 °C 0.31 g (1.55 mmol) of potassium bis(trimethyl silyl amide) NH_2 was added via a syringe followed by 10 mL of THF. The reactor was then brought to room temperature and stirred for 72 hours. The resulting product was purified, dried, and deprotected with HCl. To deprotect the polymer 1 g of polymer was added to an Erlenmeyer flask and dissolved in 10 mL of THF. As the solution stirred via a magnetic stirrer approximately 10 to 20 drops of HCl was added and the reaction mixture was stirred overnight and purified after reaction. The modification of the polymer was confirmed by NMR with peaks at 2.4 ppm ($\text{CH}_2\text{-NH}_2$, protons next to amine end group), 3.3 ppm ($\text{CH}_2\text{-OH}$, protons next to hydroxyl end group), and 3.7 ppm ($\text{O-CH}_2\text{-CH}_2\text{-O}$, PEG).

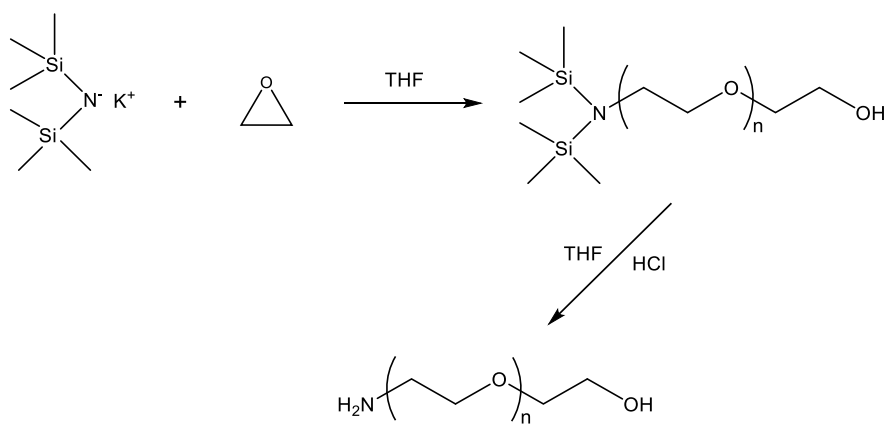


Figure 2.8. Synthesis and deprotection of PEG-amine.

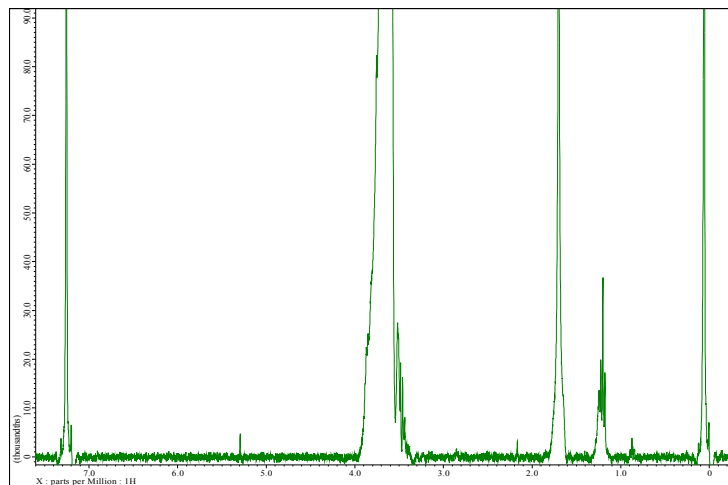


Figure 2.9. NMR spectra of PEG-amine.

2.2.4 Ligand Exchange

Equal amounts of the synthesized particles were modified with either PEG-COOH, PEG-nitroDOPA, PEG-phosphonate or PEG-NH₂ to monitor the displacement of ¹⁴C-oleic acid via ligand exchange (Figure 2.10). To modify the particles, 0.02 mmol of each modified PEG polymer was dissolved in chloroform in a 20 mL scintillation vial. The vial was capped with a rubber septum and sonicated while 10 mg of nanoparticles in chloroform was added dropwise to the polymer solution. After addition of the particles, the polymer-particle solution was put on a shake plate to mix overnight. The resulting particles were precipitated using ethyl ether, centrifuged, and re-dispersed into water. The polymer-particle solutions were further purified using dialysis to remove excess ligand. The solutions were injected into 12,000-14,000 MWCO Spectra/Por® dialysis tubing, placed in water, and put on a shake plate to stir for 72 hours. The waste from

purification was monitored using LSC. The ligand exchange procedures using each of the five different ligands were performed simultaneously.

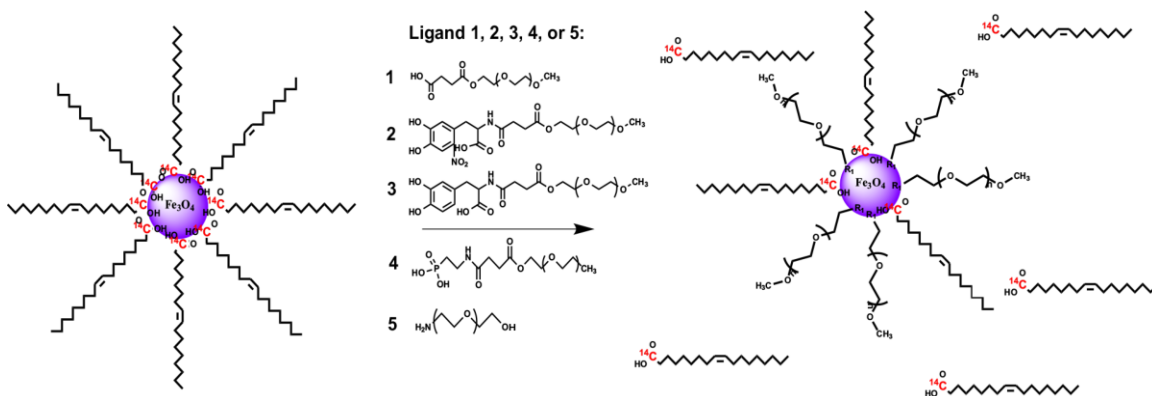


Figure 2.10. Illustration of a ligand exchange reaction. ^{14}C -oleic acid coated nanoparticles undergo a ligand exchange reaction with one of the five monofunctional PEG ligands resulting in hydrophilic particles.

2.2.5 Gel Permeation Chromatography (GPC) Column

LSC and TGA of the purified and dialyzed oleic acid coated particles indicated a large amount of oleic acid remained on the surfaces despite efforts to remove much of it.

Although these dialyzed particles containing excess oleic acid were used in the ligand exchange reactions, the need for a better method of removal in future studies remains. In order to remove the excess oleic acid, the radiolabeled and unlabeled as synthesized, oleic acid coated particles were each passed through burettes containing styrene-divinylbenzene copolymer beads swollen in toluene (Figure 2.11).¹³⁹ The beads were swollen in toluene overnight and poured into the burette in order to pack the column with the gel. The burette or column through which the unlabeled particles were passed was larger and contained more beads than the column that the radiolabeled particles were

passed through. A concentrated sample of nanoparticles in toluene was added to the top of the column, allowed to pass completely through the column as a dark band, and collected at the bottom for further analysis. The radiolabeled particles were characterized by liquid scintillation counting and the unlabeled particles were characterized by thermogravimetric analysis.

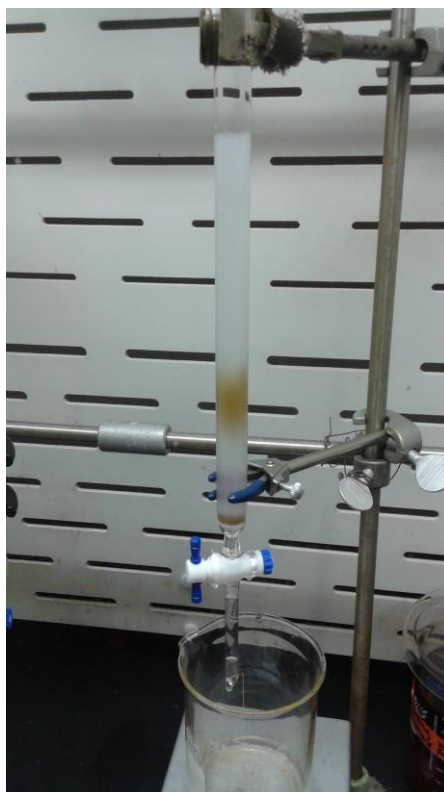


Figure 2.11. Nanoparticles passing through a GPC column.

2.2.6 Characterization

Transmission electron microscopy (TEM) was used to determine the core size of the labeled and unlabeled nanoparticles. The samples were prepared by dilution of the nanoparticle solution and application to a copper grid with carbon mesh. TEM images were obtained on a Hitachi H7600 with an accelerating voltage of 120 kV. Image

analysis to determine particle size and distribution was performed using Adobe Photoshop® and Kaleidograph®. Lognormal fits of the particle distributions were performed using MATLAB to determine average particle surface area and average core diameter.

Dynamic light scattering (DLS) was used to determine the hydrodynamic diameter of the modified and unmodified particles. The nanoparticle solutions were diluted with water or hexane and put into a cuvette. Each unlabeled sample was measured three times at 25 °C using a Malvern Zetasizer Nano ZS to determine the intensity average size distribution and z-average diameter. Each radiolabeled sample was measured three times at 25 °C using a Brookhaven 90Plus with ZetaPALS to determine the size distribution and effective diameter. Although the Malvern instrument reports a z-average diameter and the Brookhaven reports an effective diameter, studies by Jaeger et. al. show that both instruments report the same average diameter of the particles.¹⁴⁰

The surface potential of the nanoparticles was determined using zeta potential measurements. The modified and unmodified particles were measured before and after dialysis. The nanoparticle solutions were diluted with water or hexane and put into a zeta cell or a cuvette with a dip cell. Each sample was measured three times at 25 °C. Again, the particles without radiolabeled ligands were measured using a Malvern Zetasizer Nano ZS and the radiolabeled particles were measured using a Brookhaven 90Plus with ZetaPALS.

Thermogravimetric analysis (TGA) was used to determine surface coverage of the ligands on the surface of the nanoparticles before and after modification. Approximately

5 to 10 mg of sample was placed in a TGA pan, which was analyzed using a TA Instruments Hi-Res 2950 Thermal Gravimetric Analyzer. The samples were heated to 110 °C at 20 °C/minute, held at that temperature for 30 minutes, then heated to 800 °C at 15 °C/minute. The surface coverage of the ligands on the nanoparticles in chains/nm² was determined by a series of calculations. First, the total surface area of the nanoparticles in 1 gram of nanoparticle/polymer complex was determined using the average particle diameter and average surface area yielded by TEM image analysis. The TGA percent weight loss value and the density of magnetite were used to determine the total volume of nanoparticles in 1 gram of complex. This value divided by the volume of one nanoparticle multiplied by the surface area of one nanoparticle yielded the total surface area. Second, the number of chains in 1 gram of complex was determined using the molecular weight of the polymer and Avogadro's number. Finally, the number of chains was divided by the total surface area to yield the total surface coverage in chains/nm².

Vibrating sample magnetometry was used to verify the magnetic properties of the particles. The VSM sample was prepared by adding a few drops of the unlabeled, oleic acid coated nanoparticles onto a piece of scotch tape and drying it overnight. The sample was analyzed at 300K in a 3T field with a Quantum Design VSM which runs on the physical property measurement system 6000 (PPMS 6000).

Inductively coupled plasma-mass spectroscopy (ICP-MS, ThermoScientific MS XSeries 2) was used to determine the concentration of the nanoparticles in solution. Aliquots of the samples were digested with a 2% nitric acid solution in a 15 mL centrifuge tube.

Liquid scintillation counting (LSC) was employed as the method of tracking the exchange of the radiolabeled ligand with the unlabeled, hydrophilic ligands. Samples of the nanoparticle particle solutions were digested with concentrated nitric acid (HNO₃) to minimize color quenching and added to a 20 mL vial. Samples of the waste solutions from purification were not digested due to their minimal color quenching. These aliquots from the waste solutions were also added to 20 mL vials. A scintillation cocktail was then added to the vials and mixed with the sample. The samples were analyzed using a Hidex 300 SL automatic liquid scintillation counter. MikroWin Hidex 2000 v.4.43 software was used to view and analyze the sample data. Furthermore, the amount of color quenching in each sample was determined using a Perkin Elmer TriCarb 2910 TR LSC instrument. The quench data was used to verify or correct the counting efficiency determined using triple-to-double coincidence counting measured in situ on the Hidex.

2.2.7 Calculation of Oleic Acid Surface Coverage on Nanoparticles

The LSC data and ICP-MS data were used to calculate the amount of oleic acid present on the surface of the nanoparticles before and after ligand exchange. The calculated amounts were compared to determine a hierarchy of binding of the different hydrophilic ligands utilized in the procedures. The LSC results are initially reported in counts per minute. This data can be converted to decays per minute (dpm) and used to determine the moles of ¹⁴C-oleic acid per milliliter of solution using the equation below:

$$\text{Eq. 2.1) } \frac{\text{moles } ^{14}\text{C}}{\text{ml}} = \frac{(\text{sample cpm} - \text{background cpm}) / \text{TDCR/ml}}{\frac{\ln(2)}{t^{1/2}} \times (6.022 \times 10^{23})}$$

where the numerator represents dpm, TDCR is the triple-to-double coincidence ratio used to account for detection efficiency, cpm is counts per minute, the denominator is the decay constant (λ) is $2.3 \times 10^{-10} \text{ min.}^{-1}$ for ^{14}C) multiplied by Avogadro's number, and the half-life ($t^{1/2}$) is 5,730 years for ^{14}C . This value was used to determine the total amount of oleic acid per milliliter of sample, assuming a constant ratio of radiolabeled to unlabeled oleic acid and accounting for oleate ligands from the precursor. The ICP-MS data was used to determine the concentration of particles in solution. Knowing the average surface area of the particles determined from the lognormal fit of the size distribution, a normalized surface area per unit volume of sample was calculated. Finally, using the oleic acid concentration and the surface area concentration, the total amount of oleic acid per nm^2 of Fe was calculated.

2.3 Results and Discussion

Nanoparticles were synthesized via thermal decomposition and modified via ligand exchange. The particles were characterized to determine size, hydrodynamic diameter, surface potential, magnetic properties, and surface coverage of the ligands. The particles were also analyzed by LSC to quantify the amount of radioactive oleic acid present on the surface of the particles before and after ligand exchange.

2.3.1 TEM

Analysis of the TEM images yielded size distributions (Figure 2.6) for the unlabeled and labeled particles. Lognormal fits of the distributions produced the average surface area from which the average diameters of the particles could be determined. The average core diameter of the unlabeled particles was 10.6 nm with a standard deviation of 2.24 nm and

10.0 nm with a standard deviation of 2.26 nm for the labeled particles. (Figure 2.12) The wide size distributions of the particles can be explained by the inability to perform syntheses of these particles under nitrogen while purging which would have allowed for greater control of size and size distribution. Purging the radiolabeled reaction might have released radionuclides into the atmosphere. Furthermore, the synthesis of the unlabeled particles was performed the same for procedural consistency. The size distributions were accounted for in the average surface area calculations by the lognormal fits of the histograms. The sizes, determined from the average surface areas, were used in the calculations to determine the amount of ligand present on the surface of the nanoparticles. These calculations for surface coverage by TGA are discussed in an earlier section and calculations for surface coverage by LSC are discussed in a later section.

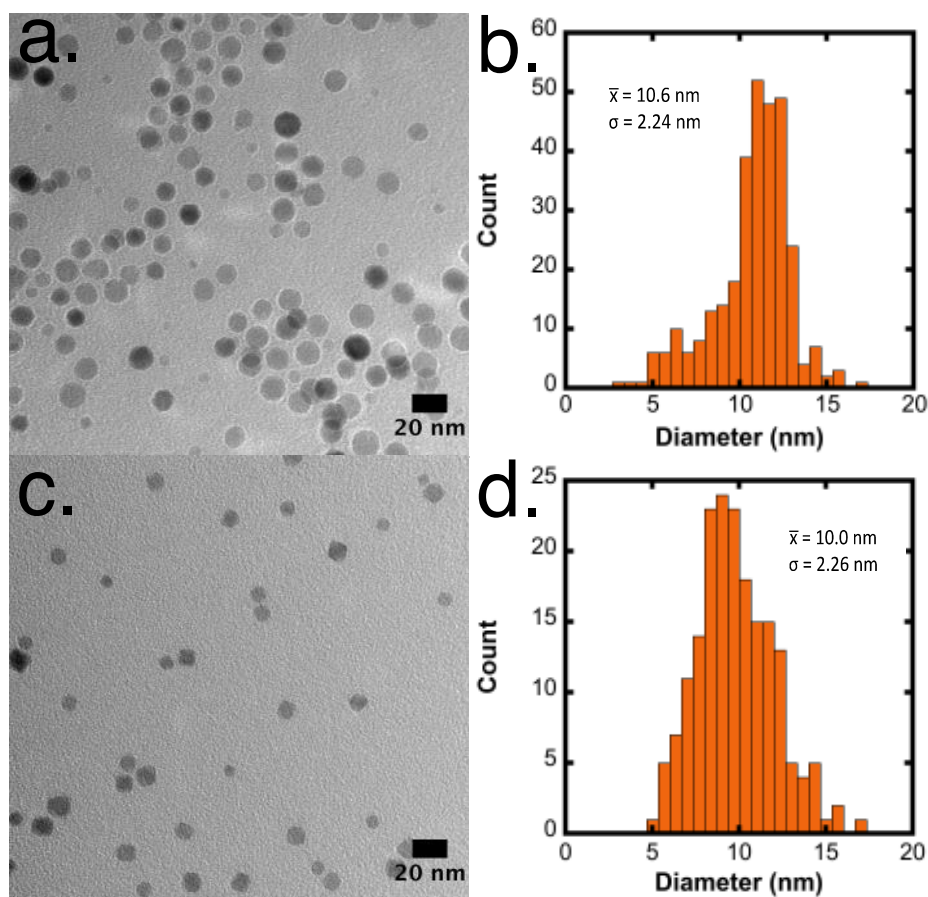


Figure 2.12. TEM image (left) and size analysis (right) of the unlabeled nanoparticles (top) and the radiolabeled nanoparticles (bottom). The histogram shows the size distribution of the nanoparticles.

2.3.2 DLS

The hydrodynamic diameters of the particles were determined using DLS. This yielded information about the size of the particles with oleic acid on the surface and with the new hydrophilic ligands on the surface. The data in Table 2.1 summarizes the results for the particles and shows good agreement in trends and values between the labeled and unlabeled particles. The addition of the PEG brushes yields an increased hydrodynamic diameter between 80 nm and 100 nm for the PEG-DOPA and PEG-nitroDOPA particles, which agrees with previous studies by our group.^{101, 141} The zeta potentials of the PEG-

DOPA and PEG-nitroDOPA particles are not very negative and are relatively close to zero indicating that electrostatic repulsion does not play a large role in particle stabilization. This is expected for particles coated in PEG as the methoxy end groups exposed to the water do not carry a charge. However, the more negative zeta potentials of the PEG-Phosphonate, PEG-COOH, and PEG-NH₂ particles may indicate the presence of excess ligands in solution or at the surface of the particles yielding a surface charge. The increased hydrodynamic diameters for PEG-Phosphonate, PEG-COOH, and PEG-NH₂ particles also indicates that the particles may have excess ligands on the surface or are agglomerating in solution. The larger uncertainty ranges of these particles indicate that they are not very stable in water and are likely precipitating and agglomerating during the measurements. Instability and unwanted surface charge of the nanoparticles can have a negative impact depending on the desired application such as drug delivery.

Table 2.1. Hydrodynamic diameters and zeta potentials of the unlabeled and labeled modified and unmodified nanoparticles.

Unlabeled particles	Fe₃O₄-oleic acid np	PEG-nDOPA np	PEG-DOPA np	PEG-Phosphonate np	PEG-COOH np	PEG-NH₂ np
Z-avg. diameter (nm)	35.4±4.3	90.3±5.2	84.7±3.2	203±12.7	220±14.3	176±10.1
Zeta potential (mV)	n/a	-6	-5	-15	-22	-23

Labeled particles	Fe₃O₄-oleic acid np	PEG-nDOPA np	PEG-DOPA np	PEG-Phosphonate np	PEG-COOH np	PEG-NH₂ np
Effective diameter (nm)	41.2±5.4	100±7.1	89.1±5.1	214±11.5	232±15.2	184±11.6
Zeta potential (mV)	n/a	-7	-6	-18	-25	-24

2.3.3 TGA

TGA data yielded percent weight loss of material on the surface of the unlabeled, oleic acid coated nanoparticles before and after dialysis and on the surface of unlabeled, PEG coated nanoparticles after dialysis (Figures 2.13-2.16). These values were used to calculate the grafting density of the ligands on the nanoparticles under the assumption that only one type of ligand, PEG or oleic acid, was present on the surface of the particles. Table 2.2 contains a summary of the data. The TGA data illustrates a trend similar to the DLS data with the more stable particles (i.e. PEG-nDOPA and PEG-DOPA) having a higher surface coverage than the PEG-COOH and PEG-NH₂ particles. Again, the calculations of surface coverage are made assuming that only 5000 g/mol PEG is present on the modified particles. If the PEG-COOH and PEG-NH₂ particles still have a large amount of oleic acid on the surface relative to the amount of PEG chains, then this assumption could explain why the calculated surface coverage values for these particles are so low. The values were calculated using the larger molecular weight of the PEG and

not the molecular weight of the oleic acid which would have yielded more reasonable surface coverage values. The PEG-Phosphonate particles have a higher surface coverage like the PEG-DOPA and PEG-nitroDOPA particles. However, the DLS and zeta values for these particles may attribute this higher surface coverage to the presence of excess ligand and a mix of oleic acid and PEG chains.

Table 2.2. Weight percent loss and corresponding grafting densities of nanoparticles obtained from TGA analysis.

	Np before dialysis	Np after dialysis	PEG-nDOPA np	PEG-DOPA np	PEG-Phosphonate np	PEG-COOH np	PEG-NH₂ np
Weight loss (%)	59.9	51.2	74.2	79.2	76.8	37.9	40.2
Surface coverage (chains/nm ²)	29.1	20.4	3.16	4.18	3.65	0.67	0.74
LSC corrected surface coverage (chains/nm ²)	n/a	n/a	3.13	4.16	3.60	0.61	0.70

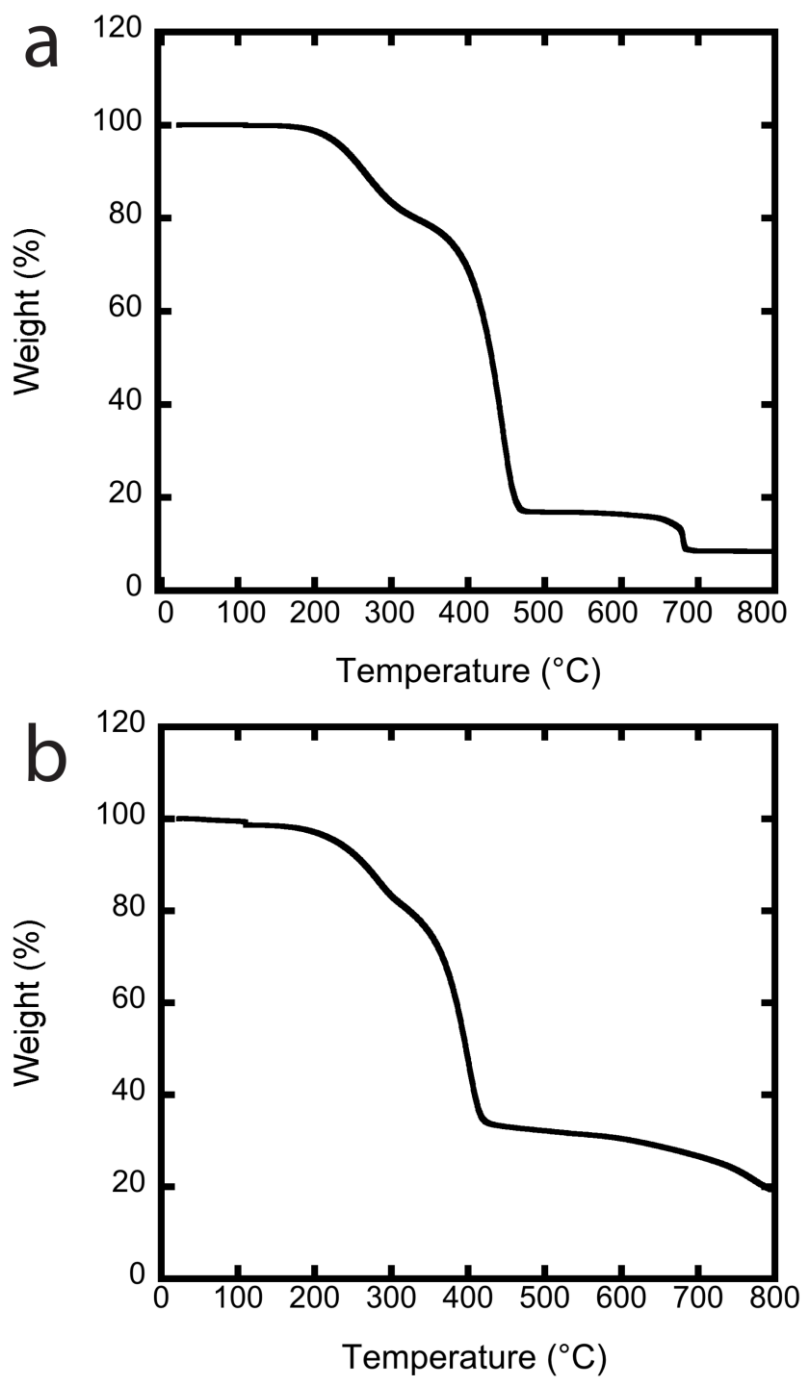


Figure 2.13. TGA curves of unlabeled, oleic acid coated nanoparticles a) before dialysis and b) after dialysis in chloroform.

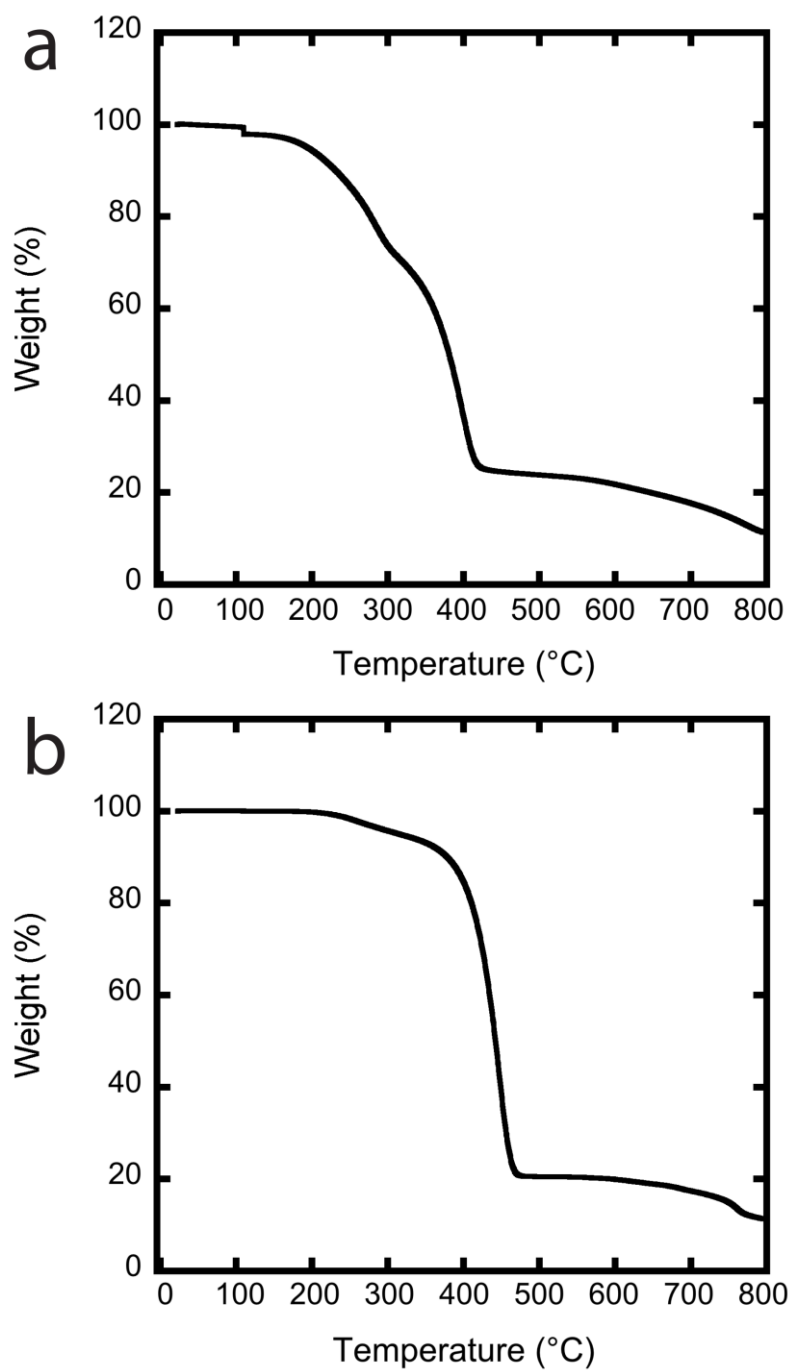


Figure 2.14. TGA curves of unlabeled a) PEG-nitroDOPA modified nanoparticles and b) PEG-DOPA modified nanoparticles.

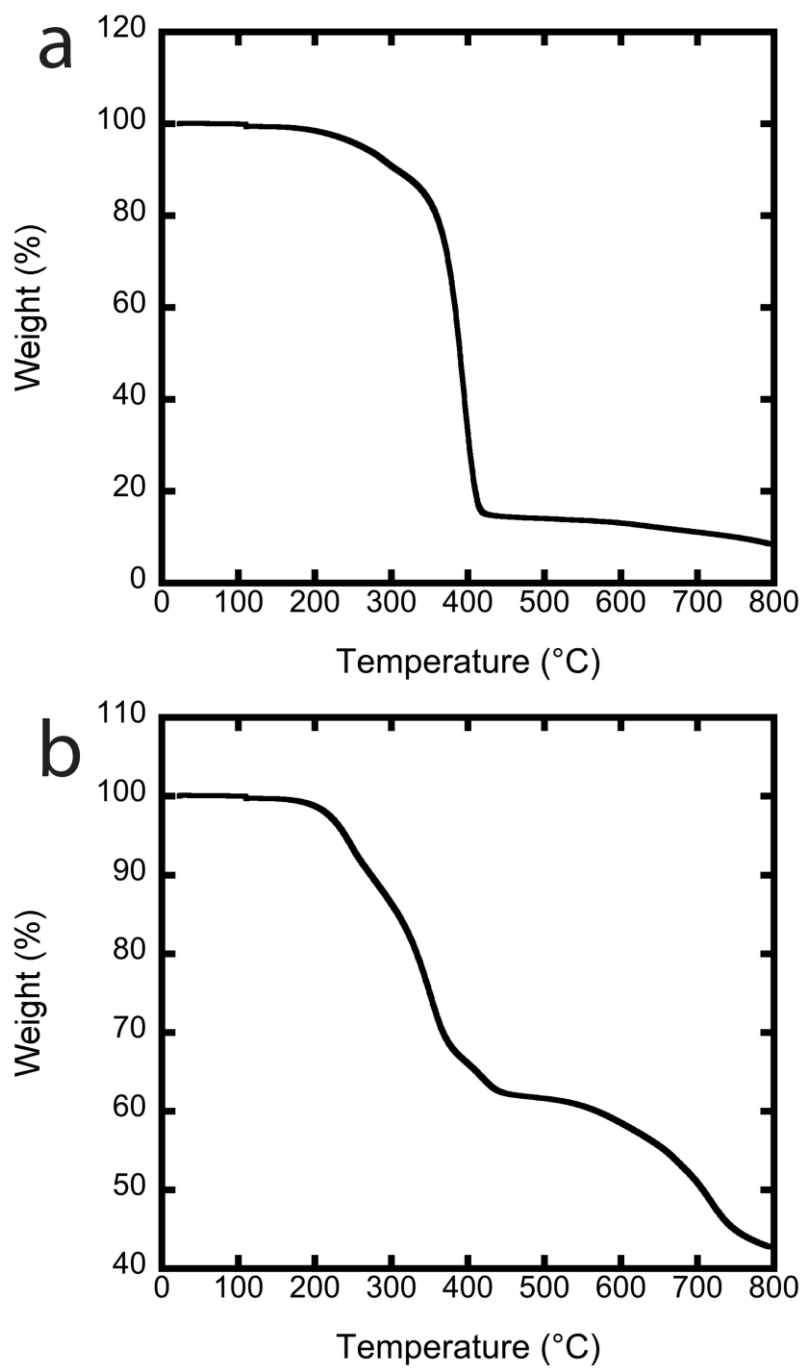


Figure 2.15. TGA curves of unlabeled a) PEG-phosphonate modified nanoparticles and b) PEG-COOH modified nanoparticles.

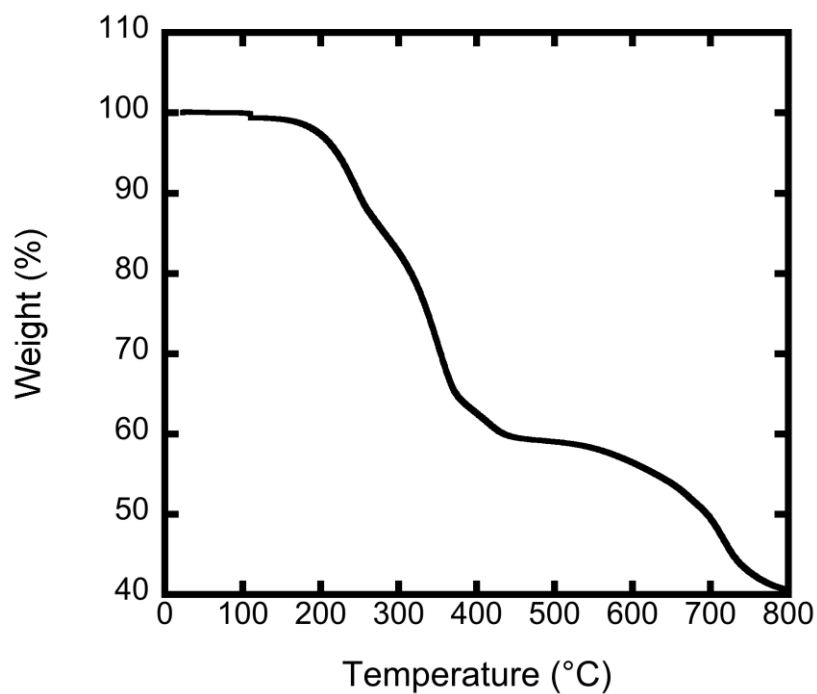


Figure 2.16. TGA curve of unlabeled, PEG-amine modified nanoparticles.

2.3.4 VSM

VSM hysteresis loops of the unlabeled, oleic acid coated nanoparticles (Figure 2.17) indicate the particles are magnetic with a saturation magnetization of approximately 66.85 emu/g of nanoparticles. This is within the range of 60-90 emu/g expected of magnetite (Fe_3O_4) nanoparticles.¹⁴² The coercivity was found to be less than the accuracy of the instrument indicating that there is little to no hysteresis in this sample at room temperature.

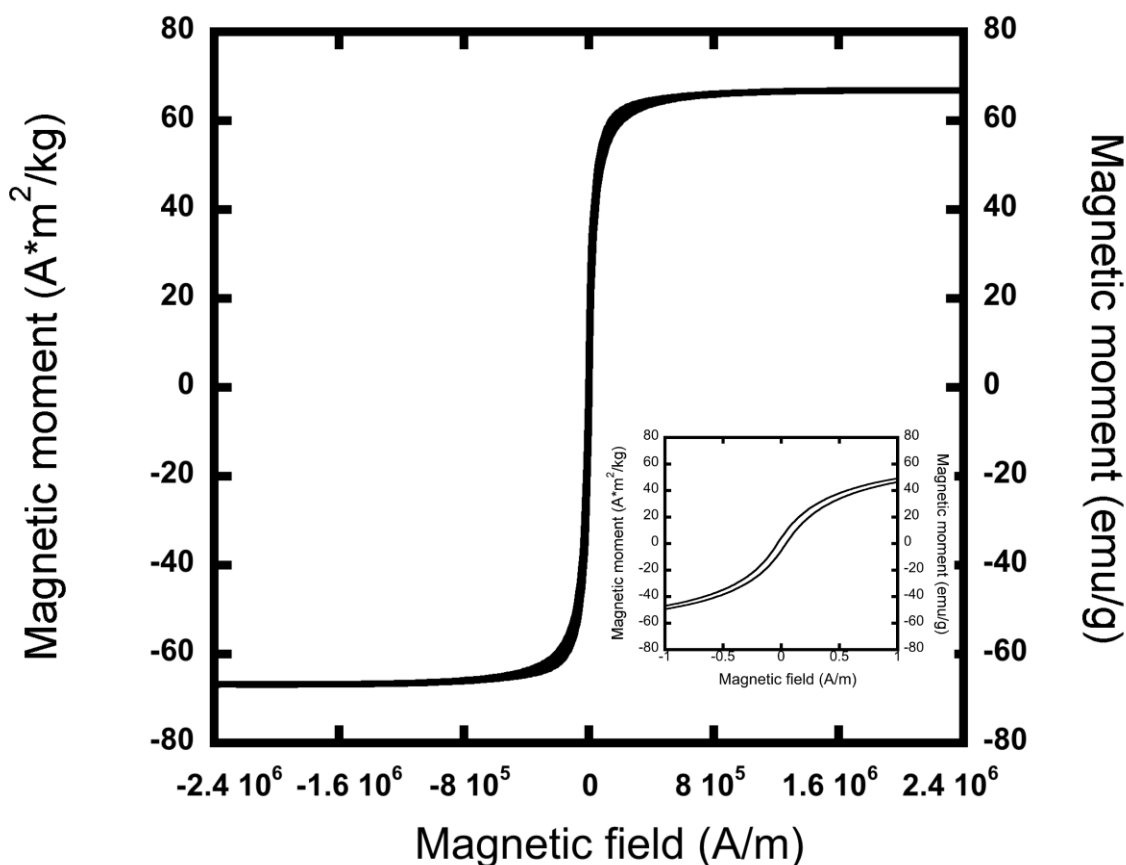


Figure 2.17. Hysteresis loop of the unlabeled nanoparticles. Magnetic moment is measured in SI units of $A \cdot m^2/kg$ of magnetite as determined by ICP-MS.

2.3.5 LSC

The amount of radiolabeled oleic acid in each sample was determined using LSC. The data for each sample was normalized to the number of nanoparticles present in the sample (based on determination of total Fe via ICP-MS), and the measured radioactivity was used to ultimately calculate the amount of oleic acid present on the surface of the particles before and after modification. The amount of oleic acid on the surface of the oleic acid coated nanoparticles before and after dialysis and on the modified particles after dialysis is shown in Figure 2.18. The results indicate a large amount or excess of

oleic acid on the surface of the particles after dialysis and before modification. Dialysis was not useful for removing much of this excess oleic acid as shown in the figure and demonstrated by GPC (seen in a later section). Differences in surface coverage values between TGA and LSC can be explained by differences between the batches of nanoparticles synthesized. However, as expected the amount of oleic acid is dramatically decreased on the particles that were modified indicating that ligand exchange took place. The results show a trend that agrees with the TGA and DLS data. The PEG-nitroDOPA, PEG-DOPA, and PEG-Phosphonate particles have lower amounts of oleic acid than the PEG-COOH and PEG-NH₂ particles signifying a more successful modification or ligand exchange. This data reveals a hierarchy of binding of the functional groups to the surface of magnetite. The catechol groups (i.e. nitroDOPA and DOPA) and the phosphonate group bind and modify better than the carboxylic acid and the amine groups with no statistical difference (two sample t-test, $t(4)=1.44$, $\alpha=0.05$) between the amounts of oleic acid remaining on the PEG-nitroDOPA and PEG-DOPA modified particles. This relationship agrees with previous studies that show the ability to modify particles well with catechol derived anchor groups.^{100, 103} The LSC data in combination with the TGA results for the catechol-derived PEG ligands indicates greater displacement of the oleic acid and increased surface coverage of the PEG on the nanoparticles.

The LSC results were used to adjust the TGA results of the unlabeled nanoparticles to account for the oleic acid remaining on the surface after modification. Although TGA is useful for determining the amount of ligand present on the surface, it does not differentiate the types of ligands present. LSC is a sensitive technique and was used to

counter the assumption that all of the ligand on the surface of the unlabeled particles was PEG. The TGA values were corrected by subtracting the mass of oleic acid (as determined from chains/nm² by LSC) from the mass of organic material lost on the nanoparticles by TGA. Specifically, the surface coverage values determined by LSC were used to calculate the total number of oleic acid chains present on the total mass of the unlabeled nanoparticles in each respective TGA sample. Dividing the number of chains by Avogadro's number yielded the moles of oleic acid, which when multiplied by the molecular weight of oleic acid gave the amount of oleic acid in milligrams. That mass of oleic acid was subtracted from the total mass of organic material on the nanoparticles, and a new weight loss (%) was determined. From these new weight loss values the corrected surface coverages were calculated using the previously described TGA surface coverage calculations.

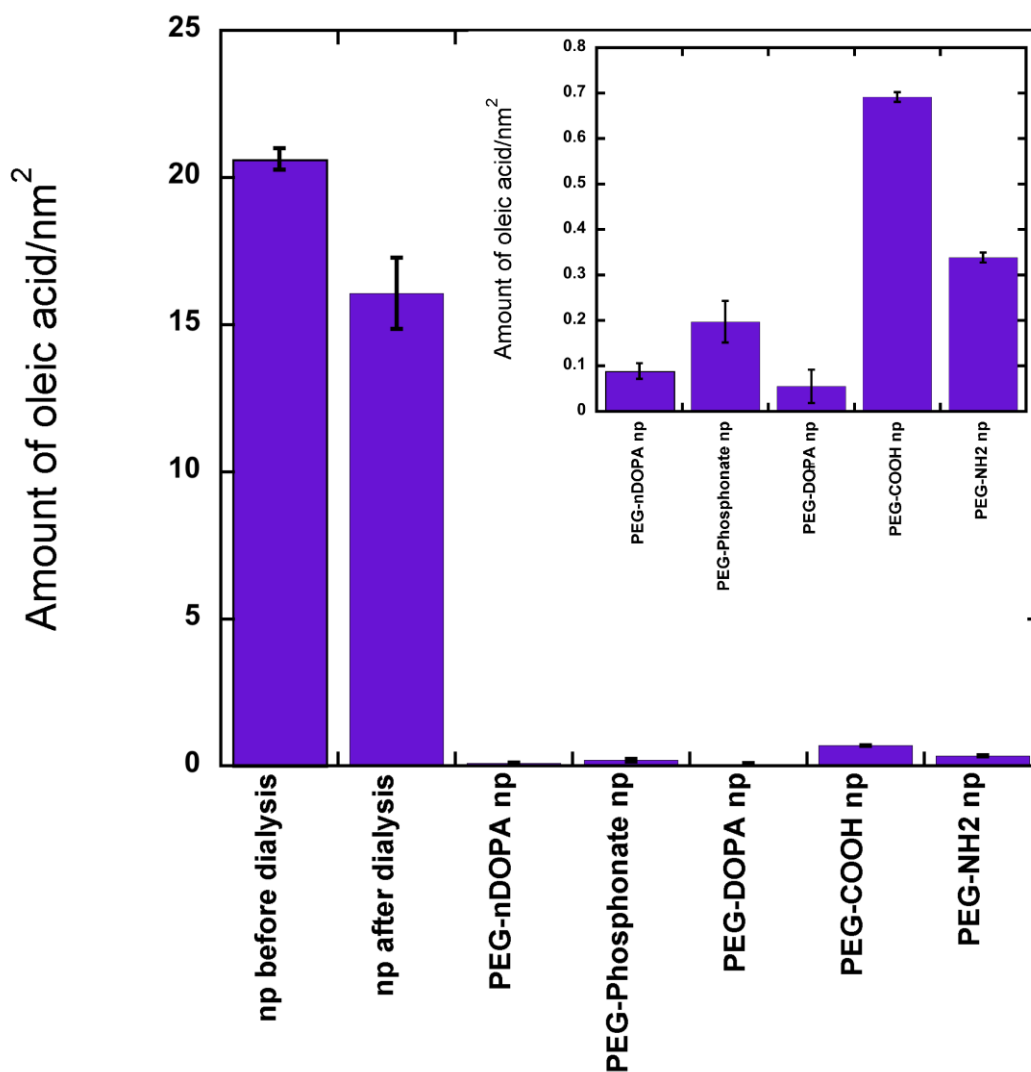


Figure 2.18. Chains of oleic acid remaining on the surface of the nanoparticles before and after ligand exchange determined by LSC. The data for the PEG coated nanoparticles represent the amount of oleic acid remaining after dialysis.

Although the results in Table 2.3 reveal a very small scale change in surface coverage for the nanoparticles, by comparison, the corrected values for the PEG-nitroDOPA and PEG-DOPA particles reveal that the majority of the organic material present on the particles was PEG. The corrected number of chains on the surface of the PEG-Phosphonate and PEG-NH₂ particles indicate a difference of 0.05-0.06 chains/nm² from the original TGA

surface coverage values. These values may seem small, but when applied to the bulk nanoparticle solution these differences could have a significant effect on the particles due to the inhomogeneity on the surfaces. Furthermore, the results indicate that all of the organic material on the PEG-COOH coated particles is in fact oleic acid and not PEG. Therefore, these particles would not be useful for any applications which require dispersion into water. The use of the LSC results to adjust the TGA data emphasizes the importance of this method for quantification and qualification of the ligand exchange.

Table 2.3. Weight percent loss and corresponding grafting densities of unlabeled, oleic acid coated nanoparticles obtained from TGA analysis and LSC results for radiolabeled, oleic acid coated nanoparticles to compare removal of excess oleic acid by dialysis and GPC.

	Np before dialysis	Np after dialysis	Np through GPC column
TGA Weight loss (%)	59.9	51.2	35.8
TGA Surface coverage (chains/nm ²)	29.1	20.4	10.8
LSC Surface coverage (chains/nm ²)	20.6	16.0	12.1

2.3.6 GPC Column

The oleic acid coated, non-dialyzed nanoparticles were passed through a GPC column of swollen beads in order to determine if the use of this method might successfully remove

more excess oleic acid than purification or dialysis. The excess oleic acid on the particles can contribute to agglomeration of the particles and may contribute to a slower rate of ligand exchange. The particles were purified and dialyzed in chloroform to remove any excess that may be present before modifying them by ligand exchange. However, as shown in Figure 2.19a and 2.19b the dialysis did not remove much if any of the excess ligand on the particles. The GPC column was used to compare methods and determine if one might be more successful than the other.

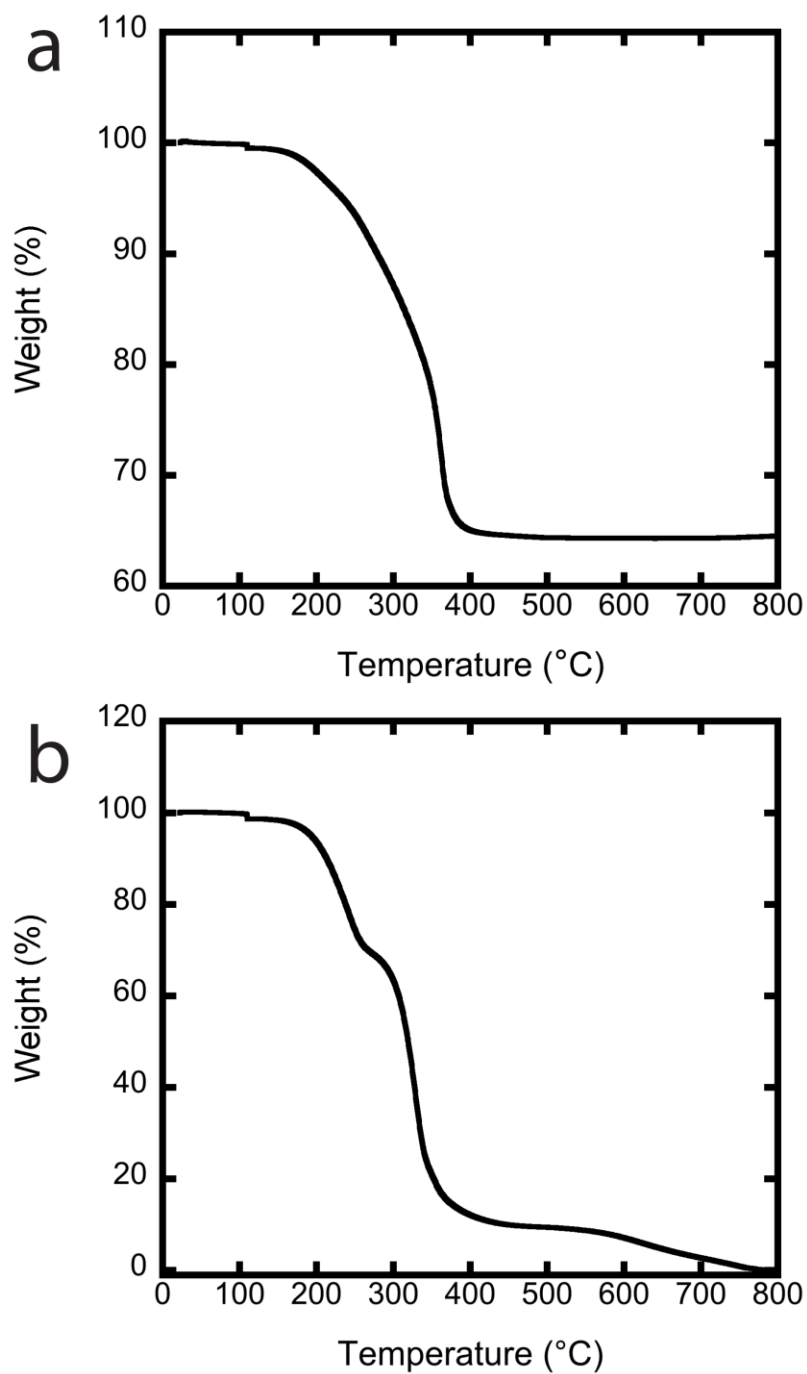


Figure 2.19. TGA curves of unlabeled, oleic acid coated iron oxide nanoparticles a) passed through a GPC column and b) iron oleate precursor.

The TGA results reveal the presence of a large amount of oleic acid on the surface of the particles before modification and little removal by dialysis. Furthermore, the TGA data

reveals the presence and removal of iron oleate precursor in the nanoparticle solutions before dialysis, after dialysis, and after the particles were passed through a GPC column (Figures 2.13 and 2.19a). The weight loss or step transition that occurs between 200 and 300°C for the nanoparticles before dialysis (Figure 2.13a) is similar to the transition seen in TGA results of iron oleate (Figure 2.19b). The dialyzed nanoparticles show a decreased transition in this region indicating that the removal of the undesired iron oleate was successful during dialysis. The TGA curves and the data in Table 3 reveal the GPC column was successful in removing iron oleate and a large amount of excess oleic acid on the surface of the nanoparticles.

The TGA and LSC results of the particles passed through the GPC columns illustrate the removal of a large amount of oleic acid on the surface of the as-synthesized nanoparticles. The TGA results in Table 2.3 and Figure 2.19a reveal a large decrease from 29.1 chains/nm² to 10.8 chains/nm² after the particles were passed through the GPC column. The LSC results in Table 2.3 reveal a decrease of almost 50% in the oleic acid chains covering the surface of the radiolabeled nanoparticles. The differences between the amounts of oleic acid removed from the unlabeled and radiolabeled nanoparticles passed through GPC columns can be attributed to the differences in the size and volumes of the columns that the particles were passed through. The larger column that the unlabeled nanoparticles were passed through allowed for more contact of the sample with the beads and more removal of excess ligand. Overall, these results indicate that the GPC column is a more effective method for removing excess, unwanted ligands on the surface of the particles. This information implies the passing of the particles through the GPC

column before ligand exchange may enhance the ligand exchange further by removing excess material which may slow down the reaction time.

2.4 Conclusions

This study provides insight into the binding hierarchy of functional groups on the surface of magnetite. LSC was used to track radiolabeled ligand on the surface of particles thereby yielding information about the efficiency or success of modification of these nanoparticles to make them suitable for certain applications. The trend shown in the data agrees well with previous studies done with catechol derived anchor groups and other functional groups attached to PEG chains. Unlike other commonly used methods, this radiotracer method using ^{14}C -oleic acid clearly indicates the presence of a specific ligand on the surface of the nanoparticles and can be used to quantify the amount of that material. The results showed that even the strongly binding catechol anchor groups (DOPA and nitroDOPA) did not remove 100% of the oleic acid. Therefore, it is not always safe to assume complete ligand exchange. Further investigation is necessary to ensure a full modification of the nanoparticles so that they exhibit the desired properties in appropriate environments. This method yielded information about the ligand composition on the surfaces of the nanoparticles which affects their stability. This method can be used to verify and even explain the results of other methods used to characterize the ligand exchange on nanoparticles. Understanding more about the surface chemistry of these nanoparticles can lead to better control in the applications of them.

CHAPTER 3: DIRECT MEASUREMENT OF LIGAND EXCHANGE ON IRON OXIDES WITH SMALL MOLECULE LIGANDS VIA RADIOANALYTICAL TECHNIQUES

Reproduced with permission from [Davis, K.; Cole, B.; Ghelardini, M.; Powell, B. A.; Mefford, O. T., Quantitative Measurement of Ligand Exchange with Small-Molecule Ligands on Iron Oxide Nanoparticles via Radioanalytical Techniques. *Langmuir* **2016**, *32* (51), 13716-13727.] Copyright [2016] American Chemical Society

3.1 Introduction

Ligand exchange using small molecules has been accomplished via different routes and moieties. For instance, small molecule ligands may be used as linkers or starting molecules for further modification.^{13, 143} In one such example, magnetite nanoparticles were modified with (3-aminopropyl)triethoxysilane (APTES) to link to poly(ethylene glycol) (PEG) chains to provide a suitable surface for MRI contrast agents.¹⁴⁴ Small molecule ligands may also be used to minimize size for different applications.^{145, 146} Portet et al. compared phosphate, phosphonate, sulfonate, and carboxylate functional molecules in MRI contrast agents due to their reduced size for enhanced tissular diffusion of nanoparticles.¹⁰² Results revealed that coating with bisphosphonate functional molecules allowed for small, stable particles across a wide pH range (2.5-13). Furthermore, competition-adsorption experiments indicated little desorption of the bisphosphonate molecules and thus promise for future physiological studies. Complete ligand exchange of these small molecules is necessary for peak performance of the nanomaterials. However, accurate determination of ligand exchange completion can

present a challenge. Previous attempts have been made to quantify ligand exchange of these materials using techniques like FTIR,^{24, 147} TGA,^{15, 148} XPS,^{25, 122} UV-Vis,^{149, 150} and photoluminescence spectroscopy.^{150, 151} Methods like these are common but may have limitations and/or may not accurately represent the extent of exchange. In the previous chapter, quantification of ligand exchange using sensitive, radioanalytical techniques exposed incomplete reactions with hydrophilic polymer ligands. This chapter introduces the utility of these radioanalytical techniques for quantification of ligand exchange with small molecule ligands.¹⁵² The ligands were chosen based on head groups which are commonly used to modify these materials, such as catechols,¹⁰⁷ thiols,¹⁵³ and silanes,¹⁵⁴ carboxylic acids,⁸⁹ sulfonates,¹⁰² and phosphonates (Figure 3.1).¹⁰²

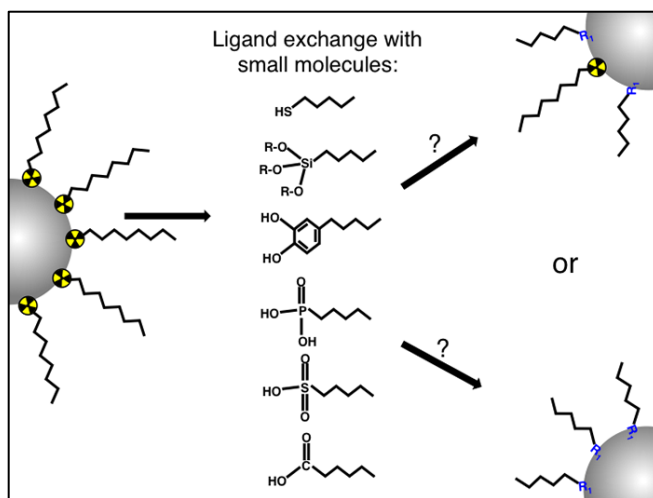
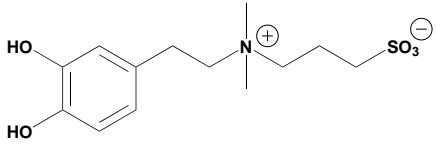
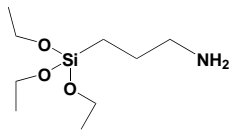


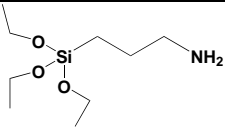
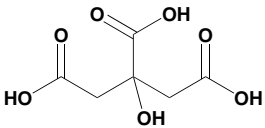
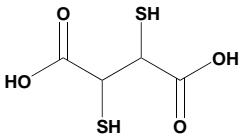
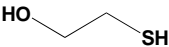
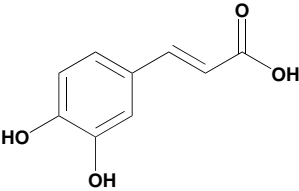
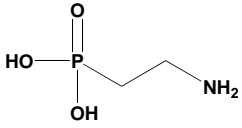
Figure 3.1. Schematic of ligand exchange with small molecule ligands bearing different head groups.

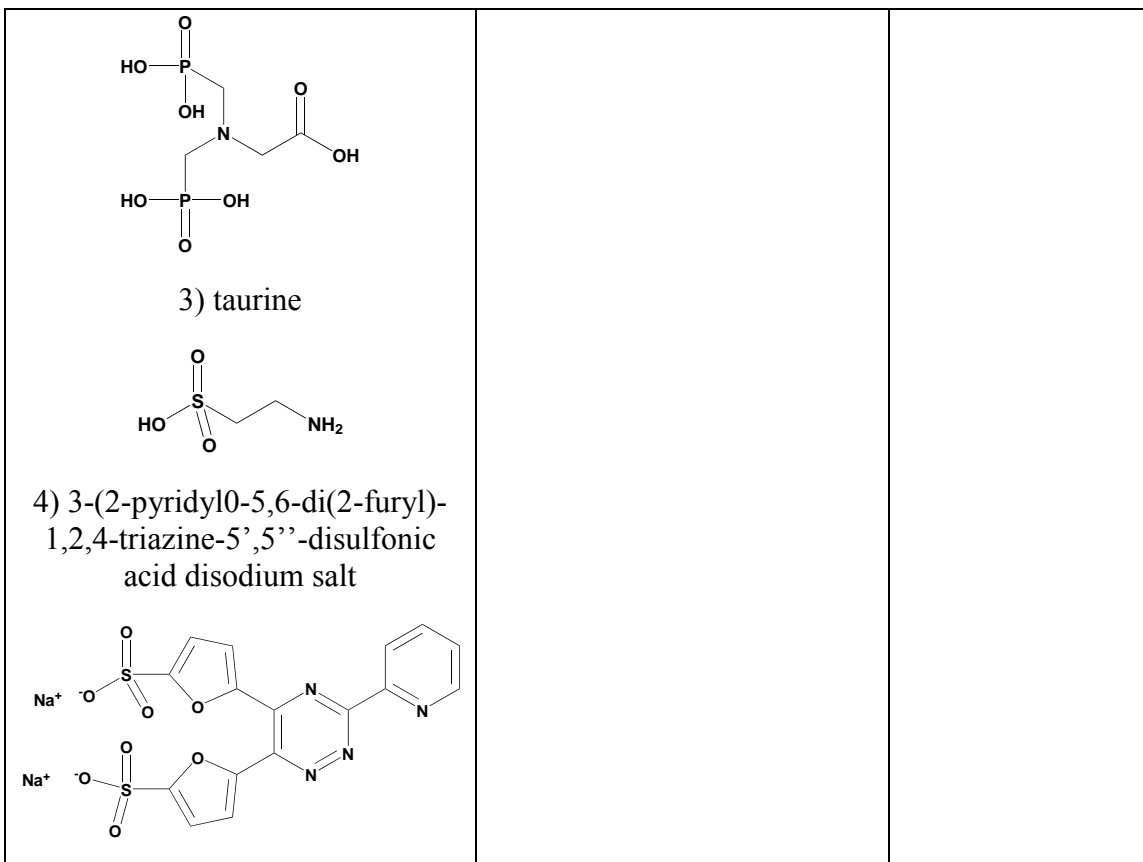
Furthermore, these ligands were employed in exchange reactions using procedures which have been previously reported and used by many other researchers. Table 3.1 contains 92 references for the previously reported ligand exchange procedures used for each of these ligands as well as references of other works which cited the original procedure. The

original procedures were shown to be useful for achieving what is claimed as complete modification of the nanoparticles, and thus, have been continually employed in other studies. However, the methods used to verify the exchange reactions may not have been sensitive enough to detect residual oleic acid after exchange which resulted in inaccurate representations of the success of the procedures and of the binding affinities of the anchor groups. Furthermore, comparison of these techniques does not allow for determination of a true binding hierarchy due to multiple uncontrolled exchange parameters. To overcome this issue, a standardized ligand exchange protocol was used to establish a hierarchy of the functional groups and to verify the success of the well established protocols.

Table 3.1. Ligand exchange procedures and references for the small molecule ligands.

Small molecule ligand	Procedure Summary	References
zwitterionic dopamine sulfonate 	2-step ligand exchange: 1) 2-[2-(2-methoxyethoxy)ethoxy]acetic acid in methanol reacted at 70°C for 5 hours 2) zwitterionic dopamine sulfonate in DMF/water solution reacted at 70°C for 12 hours	145, 146, 155-164
(3-aminopropyl)triethoxy silane (APTES) Procedure 1 	nanoparticles and APTES in toluene (6 ml) with 10 µl of acetic acid; shaken for 72 hours at room temperature	3, 14, 17, 65, 66, 88, 91, 116, 165-186
(3-aminopropyl)triethoxy silane (APTES) Procedure 2	nanoparticles in toluene exchanged with APTES in water and triethylamine	12, 122, 131, 187

	(TEA) for 15 minutes at room temperature	
<p>citric acid</p> 	nanoparticles in a 50:50 chlorobenzene and N,N'-dimethylformamide solution with citric acid, agitated at 100°C for 18 hours	13, 65, 67-69, 87, 181, 188-199
<p>1) meso-2,3-dimercaptosuccinic acid</p>  <p>2) 2-mercaptoethanol</p> 	nanoparticles in toluene with ligand in dimethylsulfoxide stirred for 48 hours at room temperature	74, 89, 90, 98, 200-206
<p>caffeic acid</p> 	caffeic acid/water solution adjusted to pH 10 using NaOH; solution added to nanoparticles in hexane; sonicated for 30 minutes and stirred for 2 hours	88, 91, 92, 119, 207-214
<p>1) 2-aminoethyl phosphonic acid</p>  <p>2) (N,N-bis(phosphono methyl) glycine)</p>	nanoparticles and ligand dispersed in THF, stirred for 24 hours under nitrogen at reflux	215-218



To quantify the extent of the exchange reactions radiolabeled iron oxide nanoparticles were synthesized via thermal decomposition with ^{14}C -oleic acid as a radiotracer. These particles were modified with citric acid, caffeic acid, zwitterionic dopamine sulfonate, dimercaptosuccinic acid (DMSA), (3-aminopropyl)triethoxysilane (APTES), 2-mercaptoethanol, (N,N-bis(phosphono methyl) glycine), 2-aminoethyl phosphonic acid, 3-(2-pyridyl)-5,6-di(2-furyl)-1,2,4-triazine-5',5''-disulfonic acid disodium salt, and taurine. The particles were modified via ligand exchange using the varied methods referenced in table 3.1 and using a standardized exchange procedure. The particles were purified and measured using liquid scintillation counting (LSC) to quantify the ligand exchange. The particles were further characterized via TEM, DLS, ATR-FTIR, and VSM

to determine size, hydrodynamic diameter and colloidal stability, qualify the modifications, and verify the magnetic properties of the particles respectively.

3.2 Experimental

3.2.1 Materials

Iron (III) acetylacetonate (99%) was purchased from Strem Chemical. Ethanol (anhydrous, histological grade), acetone (99.9%), ammonium hydroxide (29 wt%), and methanol (laboratory grade) were purchased from Fisher Chemical. Oleic acid (90%), iodomethane (99+%) and 1,3-propanesultone (99%) were purchased from Alfa Aesar. 3-aminopropyltriethoxysilane (APTES; 99%), taurine (99%), 2-aminoethyl phosphonic acid (99%) and N,N-dimethylformamide (anhydrous, 99.8%) were purchased from Acros Organics. N, N-bis(phosphonomethyl)glycine (>98%) was purchased from Aldrich Chemistry. Citric acid (>99.5%), 2-mercaptoethanol ($\geq 99\%$), dopamine hydrochloride, sodium carbonate ($\geq 99.99\%$) and 3-(2-pyridyl)-5,6-di(2-furyl)-1,2,4-triazine-5',5''-disulfonic acid disodium salt were purchased from Sigma Aldrich. Caffeic acid (3,4-dihydroxy cinnamic acid) and meso-2,3-dimercaptosuccinic acid (>98%) were purchased from Tokyo Chemical Industry (TCI). Toluene (>99.5%) and tetrahydrofuran (99%) were purchased from BDH Chemicals. Bio-Beads™ S-X1 Support (200-400 mesh) were purchased from Bio-Rad. [2-(2-methoxy)ethoxy] acetic acid was purchased from EMD Millipore. Hexanes were purchased from BD Chemical. Optiphase Ultima Gold AB liquid scintillation cocktail and oleic acid [$1\text{-}^{14}\text{C}$] (>97%) were purchased from PerkinElmer.

3.2.2 Radiolabeled Nanoparticle Synthesis

Magnetite (Fe_3O_4) nanoparticles were synthesized via a method previously reported by Vreeland et al.⁴⁴ In order to synthesize radiolabeled nanoparticles with a target diameter of 20 nm 1.074 g (3.04 mmol) of iron (III) acetylacetonate, 13.305 g (47.1 mmol) of oleic acid, and 1 μCi of ^{14}C -oleic acid were added to a 3-necked round-bottom flask. The flask was placed in a metal bath containing a low melting point metal alloy which allows for good thermal control. The reaction was heated to 200°C and purged with nitrogen. The nitrogen was passed through bubblers to prevent the release of radiolabeled materials. The solution in the flask was stirred using an overhead stirrer at 400 rpm. After the solution stirred for 10 minutes it was heated to 350°C for 3.5 hours.

The nanoparticles were purified by dispersion in 5 ml of hexane and addition of 15 ml of ethanol and 25 ml of acetone. The solution was shaken, the particles were separated using a magnet, and the remaining solvents were poured off. This process was repeated two more times to ensure removal of excess oleic acid. The particles were further purified by passage through a gel permeation chromatography (GPC) column containing styrene-divinylbenzene copolymer beads.^{15, 139} The beads were swollen in toluene overnight and poured into a burette to pack the column with the gel. A concentrated sample of nanoparticles in toluene was added to the top of the column and collected at the bottom as a dark band.

3.2.3 Synthesis of Zwitterionic Dopamine Sulfonate

Zwitterionic dopamine sulfonate was prepared using a previously reported method (Figure 3.2).¹⁴⁵ Dopamine hydrochloride (6 mmol) was dissolved in 150 ml of ethanol in a 500 ml round-bottom flask. The flask was purged with nitrogen while 28% ammonium

hydroxide (3 mmol) and 1,3-propanesultone (6.5 mmol) were slowly added to the flask. The solution was heated to 50°C and stirred for 18 hours. The resulting precipitate was filtered and washed with ethanol three times. The product, dopamine sulfonate, was dried in a vacuum oven and stored for further analysis and use. NMR was used to verify synthesis of the dopamine sulfonate by peaks at 6.6-6.8 ppm (aromatic -CH), and 3.25 ppm (-CH₂-S-) (Figure 3.3).

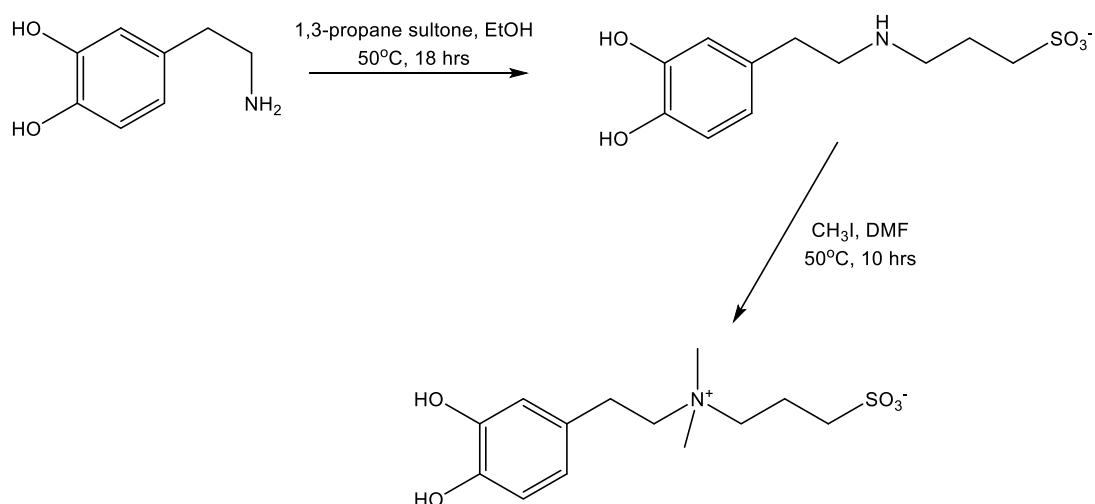


Figure 3.2. Reaction scheme for synthesis of zwitterionic dopamine sulfonate.

Dopamine sulfonate (1 mmol) was dissolved in 150 ml of dimethylformamide (DMF) in a 500 ml round-bottom flask. Anhydrous sodium carbonate (2.4 mmol) was added to the solution as it stirred via magnetic stir bar. The flask was purged with nitrogen, followed by the addition of iodomethane (35 mmol). The solution was stirred for 10 hours at 50°C. To precipitate the product, ethyl acetate was added to the solution in a 1:10 v/v ratio. The product was filtered and 50 ml DMF/acetone (1:10 v/v) was added to the product and refluxed at 55°C for 2 hours. The solution was filtered and precipitate collected. This process was repeated two more times. The final product was dried in a

vacuum oven for future analysis and use. NMR was used to verify synthesis of the zwitterionic dopamine sulfonate by peaks at 6.6-6.8 ppm (aromatic -CH), 3.25 ppm (-CH₂-S-), and ~3.12 ppm (CH₃-N⁺-).

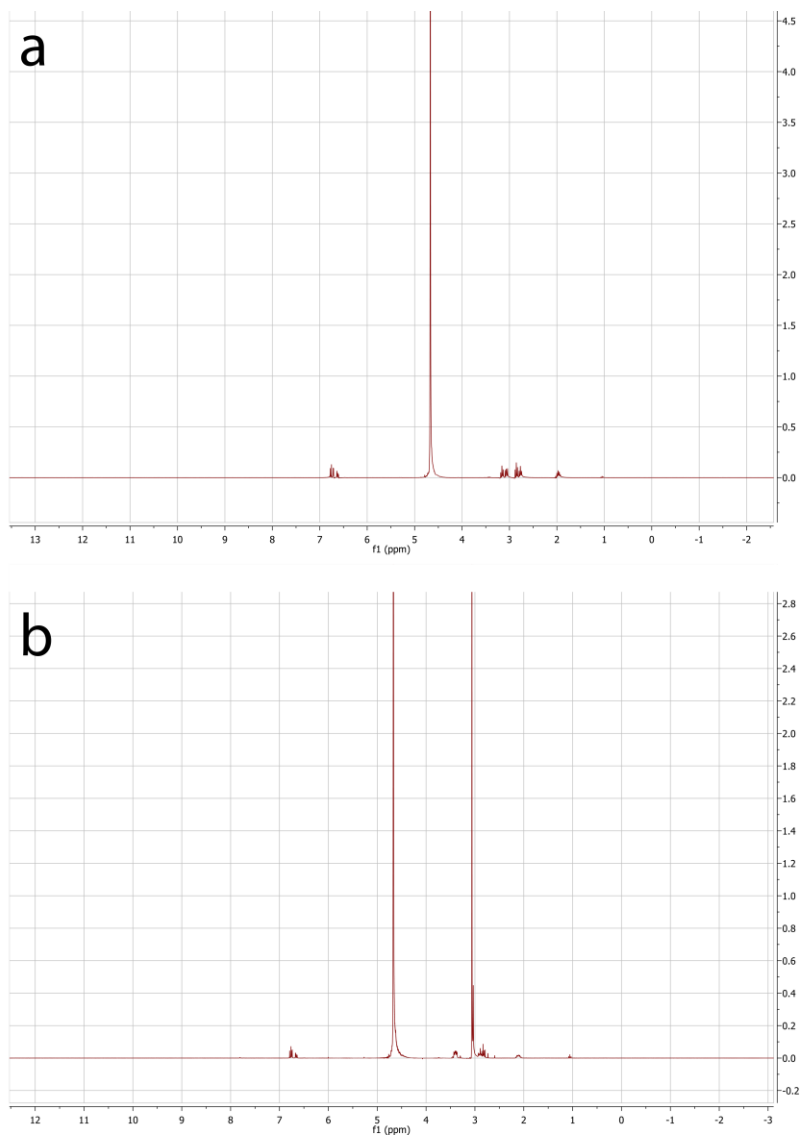


Figure 3.3. NMR spectra of a) dopamine sulfonate and b) zwitterionic dopamine sulfonate.

3.2.4 Ligand Exchange with Zwitterionic Dopamine Sulfonate

According to a previously reported procedure the nanoparticles were modified via a two-step ligand exchange.¹⁴⁵ The oleic acid was first exchanged with 2-[2-(2-methoxyethoxy)ethoxy] acetic acid in methanol at 70°C for 5 hours. Second, this ligand was replaced with the zwitterionic dopamine sulfonate in a DMF/water solution at 70°C for 12 hours. The particles from the first reaction were purified by addition of acetone and hexane to precipitate the product and centrifugation at 10,000 rpm for 5 minutes to isolate the particles. The resulting product from the second reaction was purified by addition of acetone to precipitate the particles and centrifugation at 10,000 rpm for 5 minutes to isolate the particles. These particles were then dispersed into DI water.

3.2.5 Ligand Exchange with APTES (Procedure 1)

The surfaces of the nanoparticles were modified via ligand exchange using a combination of two procedures with some variation.^{116, 165} The nanoparticles (50 mg) were dispersed in toluene (6 ml) and combined with APTES (1.5 ml). The particles were shaken on a shake plate for 72 hours at ambient conditions. The particles were separated using a magnet and washed three times using hexanes to remove excess ligands. The particles were dispersed in DI water for further characterization.

3.2.6 Ligand Exchange with APTES (Procedure 2)

Nanoparticles were modified via ligand exchange with APTES according to a previous procedure.¹²² The nanoparticles were dispersed in toluene (50 ml). The nanoparticle solution, 5 ml of TEA, and 1 ml of distilled water were added to a 100 ml, three-neck, round flask under nitrogen flow and mechanical stirring. 5 ml of APTES was added as

the solution stirred for 15 minutes. The resulting particles were purified by several washes in toluene and dispersed into DI water.

3.2.7 Ligand Exchange with Citric Acid

Nanoparticles were modified with citric acid using a previously reported procedure for ligand exchange.⁶⁵ 120 mg of dried nanoparticles were dispersed in 15 ml of a 50:50 mixture of chlorobenzene and N,N'-dimethylformamide and mixed with 0.1 g of citric acid. The mixture was agitated at 100°C for 18 hours. The particles were precipitated in diethyl ether and collected by magnetic separation. The particles were redispersed in acetone and recovered again by magnetic separation three times. The particles were dried with nitrogen to remove acetone then dispersed in water.

3.2.8 Ligand Exchange with DMSA and 2-mercaptoethanol

According to a previously reported procedure nanoparticles were modified with DMSA via ligand exchange.⁸⁹ The same procedure was used to modify the particles with 2-mercaptoethanol. The synthesized nanoparticles were dispersed in 80 ml of toluene and added to a solution of DMSA in dimethyl sulfoxide (DMSO; 20 ml). The mixture was stirred for 48 hours, and the DMSA coated nanoparticles precipitated during the reaction. The supernatant was removed and the particles were washed with ethanol and redispersed in water. Sodium hydroxide was then added to increase the pH to ~10. The resulting black, homogeneous dispersion was dialyzed for 3 days, filtered (0.22 μm) and pH adjusted to 7.

3.2.9 Ligand Exchange with Caffeic Acid

Ligand exchange with caffeic acid was performed according to a previously reported procedure by de Montferrand et al.⁹² One ml of an aqueous caffeic acid solution was adjusted at pH 10 using NaOH solution (10^{-1} mol/L). This solution was added to 1 ml of the hydrophobic nanoparticles dispersed in cyclohexane. The mixture was sonicated for 30 minutes then stirred for 2 hours. The organic, non-polar surfactant was diluted by adding 2 ml of cyclohexane, followed with centrifugation. The supernatant was discarded and the resulting particles were water dispersible.

3.2.10 Ligand Exchange with Phosphonate and Sulfonate Head Groups

According to a previously reported procedure by Lartigue et al., nanoparticles were modified with (N,N-bis(phosphono methyl) glycine) and 2-aminoethyl phosphonic acid.²¹⁵ Modifications with 3-(2-pyridyl)-5,6-di(2-furyl)-1,2,4-triazine-5',5''-disulfonic acid disodium salt and taurine were performed using the same procedure. The nanoparticles were dispersed in tetrahydrofuran and mixed with the hydrophilic ligands. The mixture was stirred under nitrogen for 24 hours at reflux. Pentane was added to the solution to precipitate and the sample was centrifuged. The product was redispersed, precipitated with ethanol, and centrifuged again to isolate the particles. The final product was dispersed into DI water.

3.2.11 Standardized Ligand Exchange

Ligand exchange reactions with all of the small molecule ligands were performed again using a more standardized method. The particles and ligands were mixed together in homogeneous solutions and allowed to react on a shake plate at ambient conditions for three days. To prepare ligand exchange reactions 5 mg of the nanoparticles were

dispersed in 8 ml of either THF or toluene and combined with the 100 mg of the ligands dispersed in either water, toluene, or DMSO. The phosphonate and sulfonate-containing ligands, citric acid, and ZDS were dispersed in 2 ml of DI water. The caffeic acid was dispersed in 2 ml of water and the pH was adjusted to 10 using NaOH (10^{-1} mol/L) in order to solubilize the ligand. DMSA and 2-mercaptoethanol were prepared by dispersion in 2 ml of DMSO, and APTES was prepared by dispersion into 2 ml of toluene. The reaction solutions were agitated on a shake plate for 3 days, collected via magnetic separation and centrifugation, dried and redispersed in water. The particles that were successfully dispersed into water were used for further analysis.

3.2.12 Characterization

TEM was used to determine the core diameter of the nanoparticles and to compare aged particles. The samples were prepared by dilution of the nanoparticle solutions and application of the solutions to copper grids with carbon mesh. TEM images were obtained using a Hitachi H7600 TEM with an accelerating voltage of 120 kV. Image analysis to determine particle size and distribution was performed using Image J.

TGA was used to determine surface coverage of the oleic acid on the nanoparticles. 5 to 10 mg of each sample was placed in the TGA pan, which was analyzed using a TA Instruments 2950 TGA. The samples were heated at 20°C/minute under nitrogen purge to 110°C, held at 110°C for 30 minutes, then heated at 15°C/minute to 800°C. According to a previously reported procedure the weight percent loss of organic material was used in a series of calculations to determine the oleic acid surface coverage of the particles.¹⁵

To determine the iron concentrations of each individual aliquot removed during the aging study ICP-MS was performed using a ThermoScientific XSeries 2 ICP-MS. The concentrated HNO₃ used to digest the samples was evaporated and the samples were dispersed in 10 ml of a 2% solution of nitric acid in DI water. The samples were measured using ⁴⁵Sc as an internal standard.

DLS and zeta potential measurements were performed to determine hydrodynamic diameter and surface potential of the unmodified and modified nanoparticles. The nanoparticle solutions were diluted with water or hexane and put into a cuvette or a zeta cell. Each unlabeled sample was measured three times at 25 °C using a Malvern Zetasizer Nano ZS to determine the intensity average size distribution, z-average diameter, and the zeta potential. The labeled particles were measured three times at 25°C using a Brookhaven 90Plus with ZetaPALS to determine size distribution, effective diameter, and zeta potential. A study by de Jaeger et al. showed that both of these instruments report the same average diameter of the particles.¹⁴⁰

ATR-FTIR was performed to qualitatively analyze the nanoparticles after modification. This technique was used to confirm the presence of the hydrophilic ligands after exchange. The nanoparticle samples were dried to remove water and/or solvent before measurement. The samples were measured using a Thermo Fisher Scientific Nicolet FTIR with ATR attachment and a diamond ATR crystal.

VSM was used to analyze the magnetic properties of the samples. The samples were prepared by adding a few drops of nanoparticle solution onto the end of a cotton swab.

The samples were analyzed at 300K in a 3T field with a Quantum Design VSM which runs on the physical property measurement system 6000 (PPMS 6000).

LSC was utilized to determine the amount of ^{14}C -oleic acid contained in the nanoparticle samples separated from each aliquot solution. A 150 μl aliquot of each nanoparticle sample in 2% HNO_3 was added to scintillation cocktail in 20 ml scintillation vials. The samples and background samples were counted for 30 minutes using a PerkinElmer TriCarb 2910 TR LSC instrument. The results, reported in counts per minute (cpm), were used to calculate the moles of oleic acid per milliliter of solution using Equation 2.1.

3.3 Results and Discussion

Nanoparticles were synthesized via thermal decomposition, modified via widely reported ligand exchange procedures and via a standardized procedure. The particles were purified and dispersed into water. The particles were characterized to determine size, hydrodynamic diameter, zeta potential, and magnetic properties, then subsequently analyzed by LSC to quantify the amount of radioactive oleic acid present on the surface of the particles after ligand exchange.

Some samples dispersed into water more easily than others, and all exchanges resulted in a large quantity of particles which would not disperse into water at all. The amount of particles that did not transfer to water from all of the reactions ranged from 75-98% of the initial particle samples. This indicates that regardless of the reaction parameters, ligand exchange does not result in high yields. Furthermore, a large number of particles and polymer must be used to insure collection of sufficient quantities of modified particles for

desired applications. Quantitative investigation of ligand exchange could lead to improvement of these reactions and increased yields.

3.3.1 TEM

The unlabeled and radiolabeled nanoparticles were imaged using TEM. (Figure 3.4) Analysis of the TEM images using ImageJ revealed a size distribution of $17.1 \text{ nm} \pm 1.8$ for the unlabeled particles and 17.8 ± 1.9 for the radiolabeled nanoparticles. These values are statistically different per a two-tailed t-test ($p < 0.0001$). The particles were synthesized via two different reactions so the sizes were not expected to be the same. The sizes, determined from the average surface areas, were used in the calculations to determine the amount of ligand present on the surface of the nanoparticles.

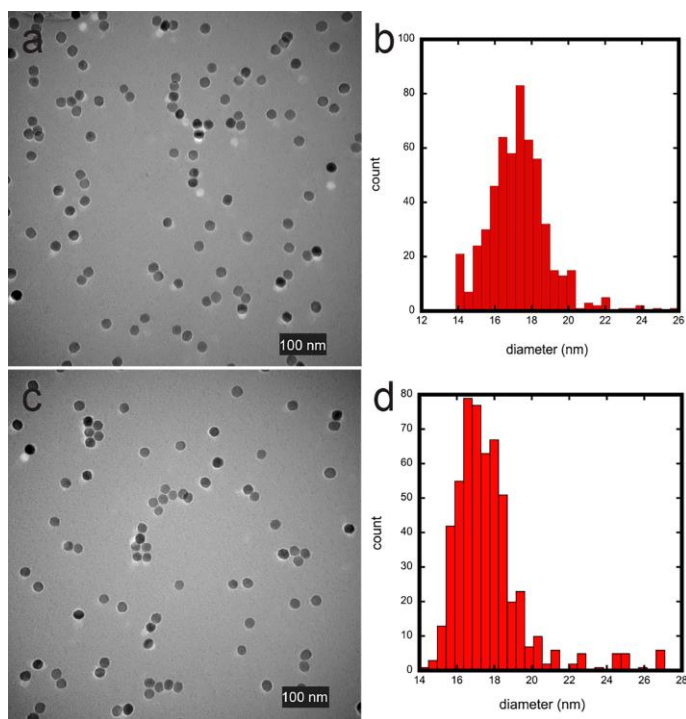


Figure 3.4. TEM images (left) and histograms (right) of the unlabeled nanoparticles (a) and the radiolabeled nanoparticles (c).

3.3.2 DLS

The hydrodynamic diameters and zeta potentials of the nanoparticles were measured using DLS. This yielded information about the stability of the particles before and after modification with the small molecule ligands. Table 3.2 shows the results of the nanoparticles modified using varied exchange protocols. Comparison of results between the oleic acid-coated particles and the modified particles reveals a decrease in hydrodynamic diameter for some of the samples modified with smaller ligands. The zeta potential values of the DMSA, APTES, bisphosphonate, and disulfonate-coated particles are around ± 30 mV which indicates moderate to good colloidal stability relative to the less stable (between -30 and 30 mV) taurine, 2-aminoethyl phosphonic acid, and 2-mercaptoethanol coated particles.²¹⁹ This trend corresponds with the increase in standard deviations of the hydrodynamic diameters of the less stable particles. The ZDS modified particles appear to be colloidally stable with a zeta potential close to zero due to the electrically neutral quality of the ligand. Table 3.3 contains the results of the nanoparticles modified using a standardized exchange procedure. The results are in good agreement with those previously discussed (Table 3.2). The zeta potential values of the APTES, caffeic acid, and citric acid modified nanoparticles in Table 3.3 indicate an increase in stability (i.e. more positive or more negative) as compared to those in Table 3.2. This is likely due to the different reaction parameters. The longer exchange time used for the standardized procedure may have allowed for increased modification (i.e., increased ligand exchange), and thus, improved colloidal stability.

Table 3.2. DLS size and zeta results of nanoparticles modified using varied procedures.

Unlabeled particles	Z-avg. diameter (nm)	Zeta potential (mV)	Labeled particles	Effective diameter (nm)	Zeta potential (mV)
oleic acid	36±3	n/a	oleic acid	38±2	n/a
ZDS	35±2	-1	ZDS	37±3	-2
APTES	39±4	31	APTES	35±5	34
citric acid	27±5	-27	citric acid	29±4	-25
DMSA	28±2	-35	DMSA	30±3	-37
2-mercaptoethanol	33±7	10	2-mercaptoethanol	35±8	13
caffeic acid	25±2	-33	caffeic acid	23±3	-36
2-aminoethyl phosphonic acid	31±5	-12	2-aminoethyl phosphonic acid	34±4	-15
bisphosphonic acid	30±2	-31	bisphosphonate	34±2	-32
taurine	29±7	-16	taurine	32±6	-19
disulfonate	50±4	35	disulfonate	55±5	32

Table 3.3. DLS size and zeta results of nanoparticles modified using a standardized procedure.

Unlabeled particles	Z-avg. diameter (nm)	Zeta potential (mV)	Labeled particles	Effective diameter (nm)	Zeta potential (mV)
oleic acid	36±3	n/a	oleic acid	38±2	n/a
ZDS	32±2	-1	ZDS	34±2	-1
APTES	33±3	34	APTES	31±2	35
citric acid	24±3	-33	citric acid	25±4	-30
DMSA	30±3	-32	DMSA	33±4	-35

2-mercaptoethanol	34±6	14	2-mercaptoethanol	37±7	17
caffeic acid	26±2	-36	caffeic acid	24±2	-37
2-aminoethyl phosphonic acid	28±4	-11	2-aminoethyl phosphonic acid	30±5	-13
bisphosphonic acid	33±2	-30	bisphosphonate	37±3	-34
taurine	35±6	-13	taurine	37±5	-14
disulfonate	54±4	33	disulfonate	57±4	34

3.3.3 ATR-FTIR

ATR-FTIR was used to qualify the modifications of the nanoparticles. The results are shown in Table 3.4. These results correspond to the spectra illustrated in Figures 3.5-3.10. The tables contain significant peaks that indicate the presence of the specific ligands on the surface of the particles. However, the spectral results also indicate the presence of oleic acid remaining on some of the particles. The results of the particles modified with APTES using a varied protocol indicate the presence of oleic acid with a peak at 1693 cm^{-1} . Results of the particles modified with taurine and 2-mercaptoethanol using both the individual procedures and the standardized procedure also indicate the presence of oleic acid remaining bound to the surface of the particles with peaks occurring around $1520\text{-}1540\text{ cm}^{-1}$. This correlates with the DLS data and could explain the colloidal instability of these particles. The results of the particles modified using varied procedures compare well with the results of those modified using a standardized

procedure. The ATR-FTIR results are only qualitative and must be used in combination with a quantitative method to confirm exchange.

Table 3.4. ATR-FTIR results of nanoparticles modified using previously reported procedures and a standardized procedure.

Small molecule ligand	Charac teristic peaks (cm^{-1}) for referenced procedures <i>Characteristic peaks (cm^{-1}) for standardized procedure</i>
ZDS	1693-1407 (ar omatic C=C bend ing), 887-640 (ar omatic C-H bending), 1033 and 943 (S-O-R), 1149 (S=O) <i>1600-1398 (ar omatic C=C bending), 900-595 (ar omatic C-H bending), 1037 and 942 (S-O-R), 1151 (S=O)</i>
APTES	1076 (Si-O-R), 929 (C-N) <i>1092 (Si-O-R), 917 (C-N)</i>
citric acid	1740 and 1697 (C=O str etch), 1139 (alkoxy C-O) <i>1732 and 1691 (C=O stretch), 1152 (alkoxy C-O)</i>
DMSA	2445 and 2528 (-SH), 1704 (C=O str etch) <i>2547 (-SH), 1700 (C=O stretch)</i>
2-mercaptoethanol	1045 (C-S str etch) <i>1036 (C-S stretch)</i>
caffeic acid	1336 (phenol C-O), 1552 (ar omatic C=C bending), 883-640 (ar omatic C-H bending) <i>1328 (phenol C-O), 1569 (ar omatic C=C bending), 890-656 (ar omatic C-H bending)</i>
2-aminoethyl phosphonic acid	1641 (N-H bend), 1068 (C-N), 1133 (P=O), 2850 ((O=)PO-H)

	<i>1628 (N-H bend), 1073 (C-N), 1123 (P=O), 2845 ((O=)PO-H)</i>
bisphosphonate	<i>1712 (C=O str etch), 1126 (P=O), 2805 ((O=)PO-H) 1703 (C=O stretch), 1137 (P=O), 2810 ((O=)PO-H)</i>
taurine	<i>1168 and 1200 (S=O), 1033 and 962 (S-O-R), 1612 (N-H bend) 1156 and 1205 (S=O), 1028 and 956 (S-O-R), 1620 (N-H bend)</i>
disulfonate	<i>1480 and 1570 (N=N), 1700-1600 (C=N stretch), 1600-1410 (C=C bending), 1040 and 937 (S-O-R), 1200 (S=O) 1490 and 1576 (N=N), 1701-1610 (C=N stretch), 1598-1423 (C=C bending), 1041 and 946 (S-O-R), 1207 (S=O)</i>

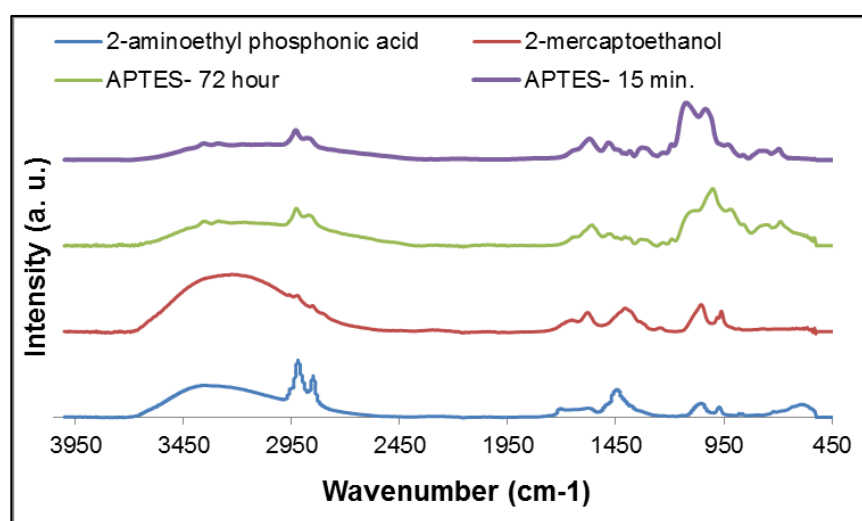


Figure 3.5. ATR-FTIR spectra of nanoparticles modified using previously reported procedures for 2-aminoethylphosphonic acid, 2-mercaptoethanol, and APTES.

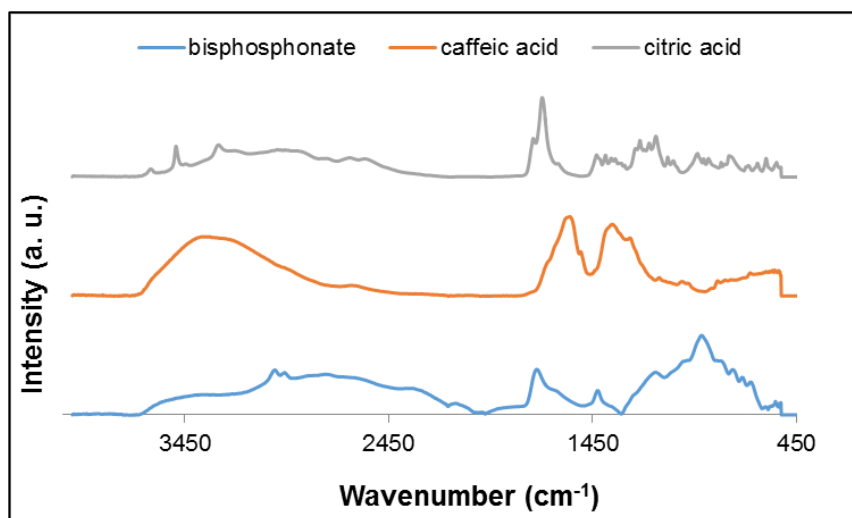


Figure 3.6. ATR-FTIR spectra of nanoparticles modified using previously reported procedures for caffeic acid, the bisphosphonate ligand, and citric acid.

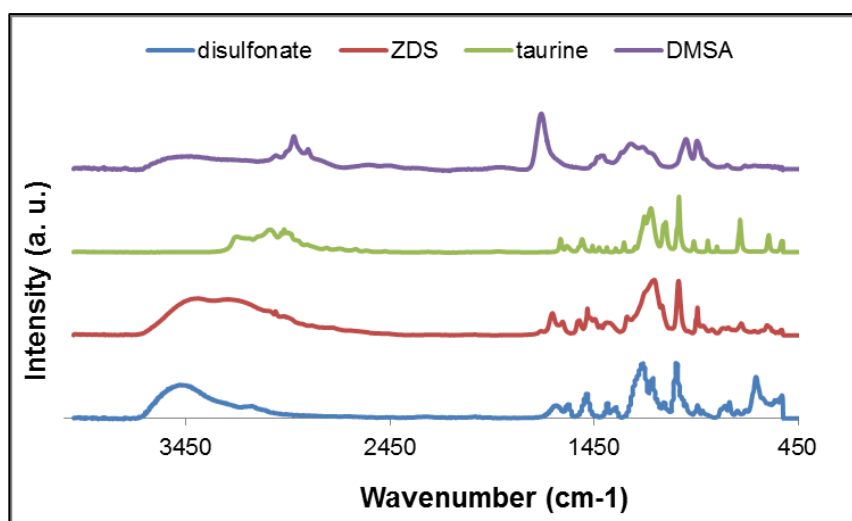


Figure 3.7. ATR-FTIR spectra of nanoparticles modified using previously reported procedures for the disulfonate ligand, ZDS, taurine, and DMSA.

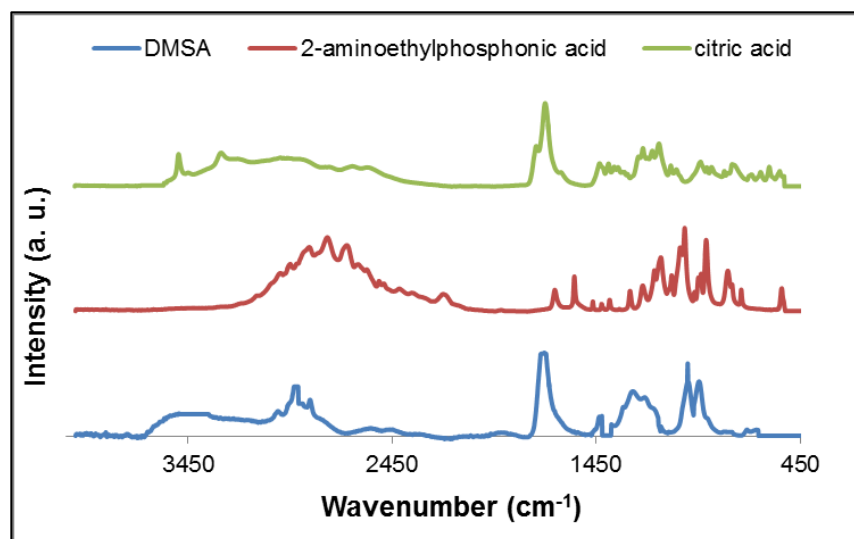


Figure 3.8. ATR-FTIR spectra of nanoparticles modified using a standardized procedure for DMSA, 2-aminoethylphosphonic acid, and citric acid.

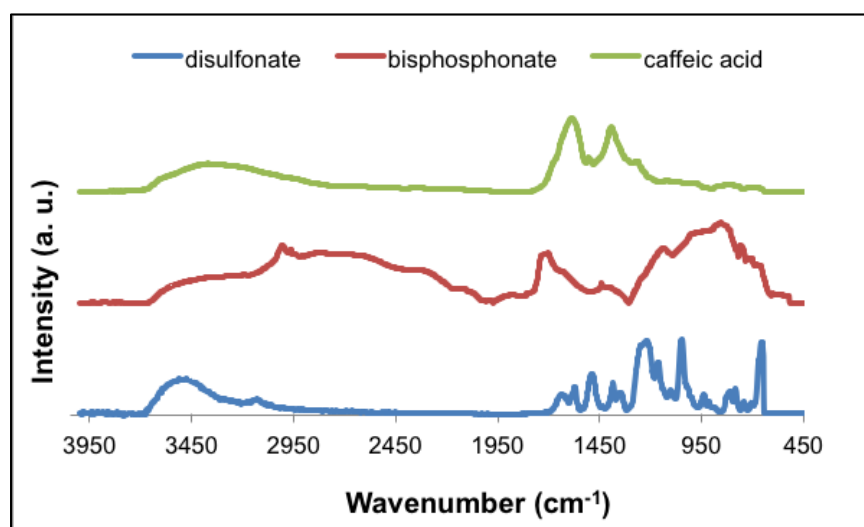


Figure 3.9. ATR-FTIR spectra of nanoparticles modified using a standardized procedure for the disulfonate ligand, the bisphosphonate ligand, and caffeic acid.

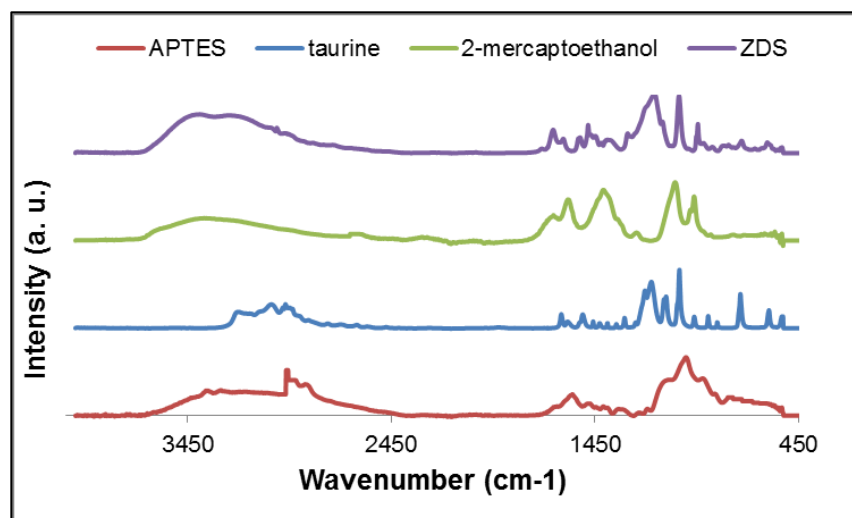


Figure 3.10. ATR-FTIR spectra of nanoparticles modified using a standardized procedure for APTES, taurine, 2-mercaptoethanol, and ZDS.

3.3.4 VSM

VSM was used to verify that the unlabeled particles were magnetic. The results in Figure 3.11 show a saturation magnetization of 40 emu/g. This value is lower than that of bulk magnetite, but comparable to values previously reported for these materials.^{165, 220} The particles were measured well after they were synthesized and stored in solvent which may have evaporated resulting in some oxidation of the particles over time and a decrease in the saturation magnetization.

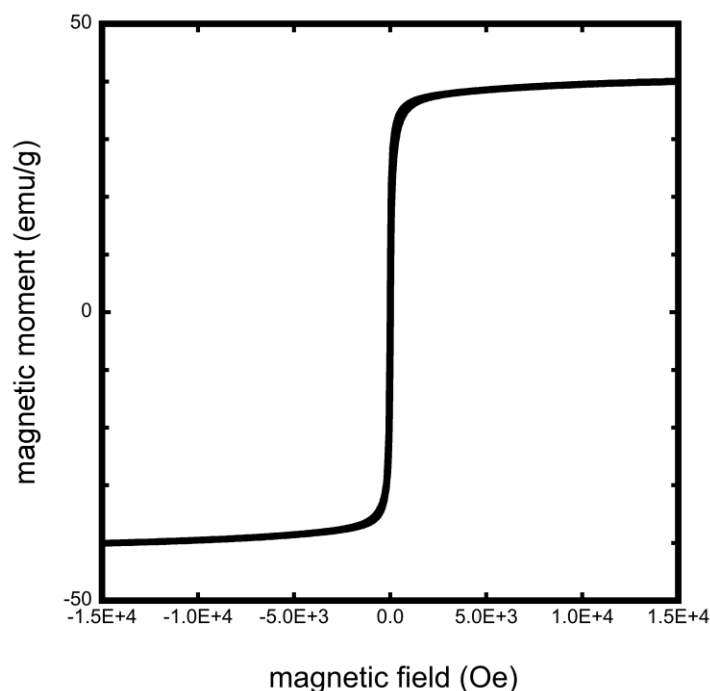


Figure 3.11. VSM hysteresis loop of oleic acid coated, unlabeled nanoparticles.

3.3.5 LSC

The amount of radiolabeled oleic acid remaining after ligand exchange for each sample was determined using LSC. The results for each sample were normalized to the total nanoparticle concentrations of each (based on determination of total Fe via ICP-MS).

The measured activity of each sample was used to calculate the total amount of oleic acid remaining on the particles after exchange using the aforementioned equation. The results of the exchange reactions using previously reported procedures are shown in Figure 3.12.

Although these results are not definitive of a hierarchy of binding moieties, they do indicate effects of binding group and reaction conditions on exchange. Results indicate that the catechol groups (i.e. caffeic acid and ZDS) displaced the greatest amount of oleic acid. This agrees with other reports of catechols binding well and with great affinity to iron oxides.^{15, 107} Furthermore, the bifunctional sulfonate and phosphonate binding

moieties displaced more oleic acid than their monofunctional counterparts. The procedures used for the sulfonate and phosphonate ligands were the same, so these results suggest that multidentate ligands bind more robustly than monodentate ligands. This finding agrees well with previous studies investigating multidenticity of ligands.^{99, 138} Comparison of results of the APTES ligand exchange reactions illustrates that increased reaction time (72 hours) and use of a catalyst (acetic acid) enhanced the displacement of oleic acid greatly. A longer reaction time allows the exchange to approach equilibrium, and a catalyst serves to speed up the reaction; therefore, it is understandable that this procedure was more successful than the 15 minute procedure. Ultimately, these results do not indicate a true binding hierarchy as there are multiple factors which are uncontrolled including the length of the exchange, multidenticity of the anchoring group, solvent conditions, temperature, and presence of catalyst. This is evidenced by the different procedures used for the APTES ligand. Therefore, it was important to further investigate using a standardized procedure to isolate binding affinity as a contributing factor. The standardized procedure allowed for uniform time of exchange, uniform temperature, and use of homogeneous solvent conditions so that the uncontrolled factor was binding moiety. Therefore, a binding hierarchy could be determined and the previously published procedures could be verified.

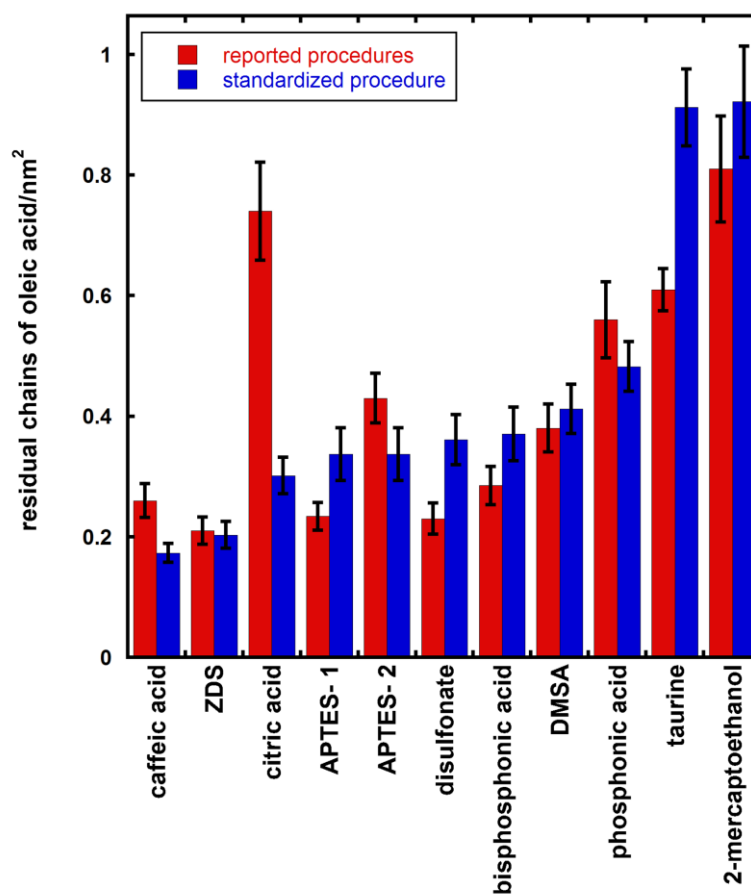


Figure 3.12. Results of ligand exchange reactions using previously reported methods and a standardized procedure.

The results of the modifications using a standardized procedure are shown in Figure 3.12. The standardized procedure allowed for exclusion of other factors, which may contribute to the binding trend. These results reveal a binding hierarchy with catechols displacing the most oleic acid and 2-mercaptoethanol and taurine displacing significantly less than the other ligands. This agrees with the results of the aforementioned ligand exchange reactions thus confirming the robust anchoring of catechols to iron oxide surfaces. The amount of oleic acid remaining after exchange with taurine using the standardized procedure is higher (~ 0.9 chains/nm²) than the amount left after exchange using the

previously reported procedure (~ 0.6 chains/nm²). The differences between these results may be explained by the use of heat and nitrogen by the previously prescribed procedure to catalyze the reaction and prevent oxidation, respectively. Again, it can be seen that the bifunctional sulfonate and phosphonate moieties displaced more oleic acid than the monofunctional phosphonate and sulfonate indicating more effective binding with multidentate ligands. APTES, citric acid, and DMSA displaced a significant amount of oleic acid resulting in particles which were colloiddally stable as indicated by DLS. The results of the APTES and DMSA exchanges using a standard procedure compare well to the use of previously reported methods indicating that variations in reaction parameters did not strongly affect the binding of the ligands. These ligands appear to bind rather robustly to iron oxides regardless of conditions. This is evidenced by the extensive use of these materials to modify iron oxide nanoparticles as indicated in Table 3.1. Finally, increased exchange of citric acid using a standardized procedure compared to the prescribed procedure could possibly be explained by the extended reaction time of the standardized procedure.

Overall, these results show that choice of binding moiety can greatly affect the success of a ligand exchange reaction. Furthermore, even when using a binding moiety with high affinity for iron oxide, there can still be oleic acid remaining after ligand exchange.

Therefore, it is prudent to thoroughly characterize the particles before and after to ensure optimal surface coverage for the desired application. These findings also suggest the importance of reaction reagents, conditions, and parameters. Extending ligand exchange

reaction time and controlling reaction conditions (i.e. catalysts, pH, temperature, stirring/agitation, etc.) may be necessary to optimize the exchange.

3.4 Conclusions

This investigation resulted in sensitive measurement of ligand exchange with small molecule ligands bearing different binding groups under varied reaction conditions. LSC was used to determine the activity of ^{14}C in each of the samples after exchange, and ultimately, calculate the amount of oleic acid remaining after ligand exchange.

Characterization of the unlabeled nanoparticles via DLS and ATR-FTIR confirmed trends observed with LSC. Despite the reaction conditions, catechols displaced more oleic acid compared to the other binding groups. However, even the catechols did not displace 100% of the oleic acid. Bifunctional ligands coated the particles more completely than monofunctional ligands illustrating the robust quality of multidentate ligands.

Furthermore, comparison of the procedures used for the APTES ligand and comparison of the varied procedures and standardized procedure revealed the importance of extending reaction time and use of catalysts to enhance the reaction. Overall, this study allows insight into the manipulation of surface chemistry of these materials and the importance of thorough examination after modification to achieve optimal quantity and quality of the product.

CHAPTER 4: THE EFFECT OF POST-SYNTHESIS AGING ON THE LIGAND EXCHANGE ACTIVITY OF IRON OXIDE NANOPARTICLES

4.1 Introduction

Magnetic nanoparticles hold great promise as a material for applications ranging from biomedical applications such as therapeutics and imaging to environmental remediation.^{1-3, 5-8} These applications would not be possible without robust methods to modify the surface of these materials. One widely used method to alter the surface properties and tailor the surface of metal and metal oxide nanoparticles is ligand exchange. The rate of the ligand exchange can be altered by the structure of the nanoparticle surface including such features as edges, grain boundaries, and defect sites. This structure creates different electron densities and steric accessibilities that affect ligand exchange rates.²²¹⁻²²³ As nanoparticles age these edge effects and defect sites may be subject to change. Furthermore, as iron oxides age they may oxidize from magnetite to maghemite. Oxidation state of iron can affect the binding of certain ligands as evidenced in a study by Amstad et al.¹⁰³ In this study they found that nitrocatechols bind preferentially to Fe²⁺ before binding to Fe³⁺. To the best of the authors knowledge, relatively little research has quantified the effects of iron oxide aging on ligand exchange.

Nonetheless, other metal and metal oxide based nanoparticles have shown appreciable decreases in properties due to aging of their surfaces. Gradual decreases in the ligand exchange reactivity²²⁴ and electrocatalytic activity²²⁵ of gold nanoparticles have been

connected to this surface aging phenomena. Disulfides have been shown to displace short chained thiols at a slower rate when the gold nanoparticles were aged in chlorobenzene solution due to thiol stabilization of defect sites.²²⁴ Aging has also been revealed to have effects on various properties of metal oxides. It has been shown that aging of copper manganese oxides affects the catalytic activity of these materials. For example, copper manganese oxides were prepared by a hydrolysis-coprecipitation method and aged for 20-72 hours post-synthesis.²²⁶ The aged oxides were compared to unaged oxides in a catalytic CO oxidation study. Results showed an increase in catalytic activity with aging due to formation of less-crystallized phases and an increase in surface area during the aging process. Aging of cobalt ferrite nanoparticles was shown to improve crystallinity of the core material,²²⁷ where the properties of surface-passivated and nonpassivated particles were aged at low pH. This caused the formation of an amorphous, iron-rich outer layer and increased the crystallinity of the core. The changes resulted from increased dissolution of the cobalt cations during the passivation process and replacement of those ions with iron cations, thus modifying the Fe/Co cation distribution which altered the magnetic properties of the particles. Dissolution is a time-evolved concern with other iron oxide materials as well.^{228, 229} One study found that dissolution of these materials is “controlled by the coordinative arrangements around the metal centers in the surface lattice.”²²⁸ Therefore, the ligands bound to the surface affect the dissolution of these materials. It was found that binuclear surface complexes formed by phosphate, arsenate, borate, and sulfate are good at inhibiting dissolution of iron oxides. In short,

there is a strong correlation in aging effects on the structural and crystalline properties of these materials, which in turn could affect binding of ligands to their surfaces.

To better understand these relationships, we developed a methodology to quantify the effects of aging on ligand exchange of iron oxide nanoparticles. Nanoparticles were synthesized via thermal decomposition with oleic acid as a stabilizing ligand. The nanoparticles were then mixed with varying concentrations of ^{14}C -labeled oleic acid at either 2, 7, or 30 days following synthesis. To measure the kinetics of exchange at the three different aging times, aliquots of the nanoparticle solutions were collected and the particles were isolated at various time points after exposure to the radiolabeled oleic acid. Liquid scintillation counting (LSC) was used to measure the activity of the samples and calculate the amount of ^{14}C -oleic acid chains present on the nanoparticles in each aliquot. Results of the aging study were further analyzed to elucidate kinetics of the reaction. A follow-up study was done to isolate the effects of oxidation, which can occur over time. In this study, nanoparticles were synthesized via thermal decomposition, and half of the reaction volume was oxidized in air for 15 minutes at 175°C . Mössbauer spectroscopy was utilized to quantify the oxidation of the particles using this procedure. Aliquots of the nanoparticle solutions (oxidized and unoxidized) were collected at various time points during ligand exchange with ^{14}C -oleic acid and measured using LSC.

4.2 Experimental

4.2.1 Materials

Iron (III) acetylacetonate (99%) was purchased from Strem Chemical. Ethanol (anhydrous, histological grade) and acetone (99.9%) were purchased from Fisher Chemical. Oleic acid (90%) was purchased from Alfa Aesar. Hexanes ($\geq 98.5\%$) were purchased from EMD Millipore. Bio-Beads™ SX-1 support (styrene-divinylbenzene copolymer beads) were purchased from Bio-Rad Laboratories, Inc. Optiphase Ultima Gold AB liquid scintillation cocktail and oleic acid [$1-^{14}\text{C}$] ($>97\%$) were purchased from PerkinElmer. Toluene (99.5%) was purchased from BDH Chemicals.

4.2.2 Nanoparticle Synthesis

Iron oxide nanoparticles were synthesized via a method previously reported by Vreeland et al.⁴⁴ To synthesize nanoparticles with a target diameter of 20 nm 1.074 g (3.04 mmol) of iron (III) acetylacetonate and 13.305 g (47.1 mmol) of oleic acid were added to a 3-necked round-bottom flask. The flask was placed in a metal bath heated to 200°C and purged with nitrogen. The solution in the flask was stirred using an overhead stirrer at 400 rpm. After the solution stirred for 10 minutes it was heated to 350°C for 3.5 hours.

The nanoparticles were purified by dispersion in 5 ml of hexane and addition of 15 ml of ethanol and 25 ml of acetone. The solution was shaken, the particles were separated using a handheld magnet, and the remaining solvents were decanted. This process was repeated two more times to ensure removal of excess oleic acid. The particles were

further purified by passage through a gel permeation chromatography (GPC) column containing styrene-divinyl benzene copolymer beads.¹³⁹ The beads were swollen in toluene overnight and poured into a burette to pack the column with the gel. A concentrated sample of nanoparticles in toluene was added to the top of the column and collected at the bottom as a dark band.

4.2.3 Aging Study

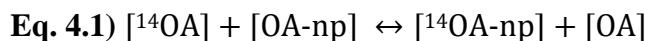
The nanoparticle solutions (20 nm target diameter; ~2 mg/ml of Fe₃O₄) aged for 2, 7, and 30 days were exposed to solutions of ¹⁴C-oleic acid in toluene. The aging was conducted by storing the particles in toluene in a sealed scintillation vial at room temperature.

Aliquots of these solutions were collected and analyzed at different time points to observe effects of aging on ligand exchange. As stated above, the concentration of the stock solution of ¹⁴C-oleic acid as determined by liquid scintillation counting was 414,908 dpm/ml. To create solutions of varying molar concentrations of ¹⁴C-oleic acid, 216.9 μ l, 433.8 μ l, and 650.7 μ l of the stock solution were combined with unlabeled oleic acid and added to the nanoparticle suspensions to obtain 5000 dpm/ml (3.6×10^{-11} mol/ml), 10000 dpm/ml (7.2×10^{-11} mol/ml), and 15000 dpm/ml (1×10^{-10} mol/ml) solutions, respectively. The particle suspensions were placed on a shake plate for approximately 0.5 minutes, 30 minutes, 1 hour, 2 hours, 4 hours, 6 hours, 8 hours, 10 hours, 12 hours, 16 hours, 24 hours, and 32 hours before 1 ml aliquots were removed from the solutions and put into 15 ml centrifuge tubes. The aliquots were mixed with 2 ml of ethanol and 2 ml of acetone to separate the excess oleic acid from the particles then

centrifuged at 9,500 rpm for 10 minutes to insure separation. The supernatant from each tube was removed and placed into separate centrifuge tubes for further analysis. After measurement and analysis of the samples it was determined that the particles should be further purified via passage through a GPC column as previously described. The particles were passed through the column once, and then smaller aliquots were passed through a syringe column (20 ml syringe) containing the same copolymer beads in toluene. The syringe column was plugged with glass wool to prevent the beads from escaping.

4.2.4 Kinetic Modelling

Modelling of the reaction kinetics was used to determine changes in rate constants with respect to aging time. Initial attempts at fitting the adsorption data to first order rate equations did not work as that approach did not account for the reversible adsorption. Modelling was based on a simplified reversible, first order reaction where one labeled oleic acid displaces one unlabeled oleic acid on the surface of the particles described by the equation below:



where $[^{14}\text{OA}]$ is the concentration of the free ^{14}C -oleic acid in the liquid, $[\text{OA-np}]$ is the concentration of the oleic acid bound to the nanoparticles, $[^{14}\text{OA-np}]$ is the ^{14}C -oleic acid bound to the nanoparticles, $[\text{OA}]$ is the unlabeled oleic acid coming off the particles, and

the reaction order is 1 with respect to the concentrations. The rate of change of ^{14}C -oleic acid in the liquid phase can be written as:

$$\text{Eq. 4.2) } \frac{d[^{14}\text{OA}]}{dt} = -k_f[^{14}\text{OA}] + k_r[^{14}\text{OA-np}]$$

Where k_f is the forward rate constant removing ^{14}C -oleic acid from the liquid phase by exchange with stable oleic acid on the nanoparticle surfaces and k_r is the desorption rate of ^{14}C -oleic acid from the nanoparticle surface. Note for convenience $[^{14}\text{OA-np}]$ is written as a liquid phase concentration above to keep the rate constants with the same units but conversion to solid phase concentrations can easily be done by multiplying by the nanoparticle suspension concentration. At time zero, the concentration of ^{14}C -oleic acid on the nanoparticle surface is zero (i.e., $[^{14}\text{OA-np}] = 0$ at time zero). Therefore, the concentration of $[^{14}\text{OA-np}]$ can be written as:

$$\text{Eq. 4.3) } [^{14}\text{OA-np}] = [^{14}\text{OA}]_0 - [^{14}\text{OA}]_t$$

Where $[^{14}\text{OA}]_0$ is the concentration of ^{14}C -oleic acid in the liquid phase at time zero and $[^{14}\text{OA}]_t$ is the concentration of ^{14}C -oleic acid in the liquid phase at time t . Equations 4.2 and 4.3 can be combined to express the reaction rate in terms of the liquid concentration of ^{14}C -oleic acid.

$$\text{Eq. 4.4) } \frac{d[^{14}\text{OA}]}{dt} = (k_f + k_r)[^{14}\text{OA}]_t + k_r[^{14}\text{OA}]_0$$

At equilibrium where the left hand side of equation 4.4 is equal to zero, the equilibrium concentration of aqueous ^{14}C -oleic acid can be written as:

$$\text{Eq. 4.5) } [^{14}\text{OA}]_{\text{eq}} = \frac{k_r}{k_f + k_r} [^{14}\text{OA}]_0$$

Combining equations 4.4 and 4.5 and integrating yields:

$$\text{Eq. 4.6) } [^{14}\text{OA}]_t = [^{14}\text{OA}]_{\text{eq}} + c_1 e^{-(k_f + k_r)t}$$

Finally applying the initial condition that $[^{14}\text{OA}]_t = [^{14}\text{OA}]_0$ at $t = 0$ to determine c_1 , the final analytical solution in equation 4.7 can be determined.

$$\text{Eq. 4.7) } [^{14}\text{OA}] = [^{14}\text{OA}]_{\text{eq}} + ([^{14}\text{OA}]_0 - [^{14}\text{OA}]_{\text{eq}}) e^{-(k_f + k_r)t}$$

Rearranging the terms and taking the natural log of each side yields the linear expression shown below:

$$\text{Eq. 4.8) } \ln \frac{[^{14}\text{OA}] - [^{14}\text{OA}]_{\text{eq}}}{[^{14}\text{OA}]_0 - [^{14}\text{OA}]_{\text{eq}}} = -(k_f + k_r)t$$

where the overall reaction rate constant $(k_f + k_r)$ is the slope and the y-intercept is zero.

The data was plotted in this linear form and analyzed using regression analysis to determine the overall slope. The linear expression (Eq. 4.8) was used to model the loss of ^{14}C -oleic acid from the liquid phase as it sorbed onto the particles as a function of time. The average slope (i.e. overall rate constant) of the plots for each data set was used to plot a model for each. Noting that the data shown below plateaus after > 30 hours, the

final measured aqueous concentration of ^{14}C -oleic acid was used as the input value for $[\text{}^{14}\text{OA}]_{\text{eq}}$. Modelling the ligand concentration on the nanoparticle surface (which was also measured to monitor conservation of mass) required the assumption that for one ligand to adsorb another ligand must desorb. This may not be an accurate description of the exchange observed. Modelling the decrease in ligand concentration from the solution as the ligands adsorb to the particles does not utilize this assumption, and therefore, may be more accurate.

4.2.5 Oxidation Study

Iron oxide nanoparticles with a target diameter of 20 nm were again synthesized according to the previously stated procedure. To oxidize the particles following particle synthesis in a controlled manner, approximately half of the resulting product was oxidized by mechanically stirring at 155°C for 15 minutes in open air. The unoxidized half was allowed to cool to room temperature under nitrogen. Both of the resulting suspensions of nanoparticles (i.e., unoxidized and oxidized) were purified by dispersion in 5 ml of hexane and addition of 15 ml of ethanol and 25 ml of acetone. The suspension was shaken, the particles were separated using a handheld magnet, and the remaining solvents were decanted. This process was repeated five more times to insure removal of the majority of excess oleic acid. Washes 4-6 for the oxidized particles were performed using centrifugation (8000 rpm for 10 minutes) to isolate the particles to prevent loss of material due to the diminished magnetic response. The particles were dispersed in toluene and a solution of oleic acid combined with ^{14}C -oleic acid as a radiotracer in

toluene (1 mol:1 mol of oleic acid to oleic acid initially present in the nanoparticle suspensions). Aliquots were collected, purified, and measured as previously described.

4.2.6 Characterization

Transmission electron microscopy (TEM) was used to determine the core diameter of the nanoparticles and to compare aged particles. The samples were prepared by dilution of the nanoparticle suspensions and application to copper grids with a carbon mesh. TEM images were obtained using a Hitachi H7600 TEM with an accelerating voltage of 120 kV. Image analysis to determine particle size and distribution was performed using ImageJ (National Institutes of Health).

Ultraviolet-visible (UV-VIS) spectroscopic measurements were performed to determine concentration of iron in the nanoparticle suspensions before addition of radiolabeled material.⁴⁴ Approximately 5-10 μ l of each magnetite sample were digested in 0.2 ml of concentrated hydrochloric acid (37%, HCl) at room temperature for 5 minutes. The dissolved iron was then diluted to 10 ml with deionized (DI) water and 0.5, 1.0, 1.5, 2, and 2.5 ml of the HCl/water solutions were pipetted into two separate 15 ml centrifuge tubes. DI water was added to each tube to dilute the solutions to 7 ml followed by addition of 0.2 ml of hydroxylamine hydrochloride aqueous solution (100 g/l), 0.5 ml of 1,10-phenanthroline aqueous solution (3 g/l), and 1.0 ml of an aqueous solution of sodium acetate and acetic acid (200 g/l and 100 g/l, respectively) were added to the centrifuge tubes. Upon addition of these reagents a pink color developed in the solution due to the coordination complex formed by the phenanthroline with iron. The absorbance

of these solutions was then obtained by a PerkinElmer UV/Vis/NIR Spectrometer Lambda 950. The absorbance values were compared to known standards and used to calculate the corresponding gram amounts of iron in the two magnetite samples. The molar relationship between iron and magnetite was then used to find the gram amount of magnetite in the two samples.

Thermogravimetric analysis (TGA) was used to determine surface coverage of the oleic acid on the nanoparticles. 5 to 10 mg of each sample was placed in TGA pan, which was analyzed using a TA Instruments 2950 TGA. The samples were heated at 20 °C/minute under nitrogen purge to 110 °C, held at 110 °C for 30 minutes, then heated at 15 °C/minute to 800 °C. According to a previously reported procedure the weight percent loss of organic material was used in a series of calculation to determine the oleic acid surface coverage of the particles.¹⁵

Inductively coupled plasma mass spectrometry (ICP-MS) was used to determine the iron concentrations of each individual aliquot removed during the aging study. The concentrated HNO₃ used to digest the samples was evaporated and the samples were dispersed in 10 ml of a 2% HNO₃/DI water solution. The samples were measured using a ThermoScientific MS XSeries 2 ICP-MS.

Liquid scintillation counting (LSC) was utilized to determine the amount of ¹⁴C-oleic acid contained in the nanoparticle samples separated from each aliquot solution. 150 µl of each nanoparticle sample in 2% HNO₃ was added to scintillation cocktail in 20 ml

scintillation vials. The samples and background samples were counted for 30 minutes using a PerkinElmer TriCarb 2910 TR LSC instrument. LSC and ICP-MS results were used to calculate the amount of oleic acid remaining on the particles after modification according to a previously reported procedure.¹⁵ The resulting counts per minute (cpm) were used to calculate moles of oleic acid per milliliter of solution using the equation below:

$$\text{Eq. 4.9) } \frac{\text{moles } ^{14}\text{C}}{\text{ml}} = \frac{\text{sample cpm} - \text{background cpm}}{\frac{\ln(2)}{t^{1/2}} \times (6.022 \times 10^{23}) \times \text{ml}} \times \text{counting efficiency}$$

where the numerator represents decays per minute (dpm), the counting efficiency is 0.931, and the denominator is the decay constant ($(\lambda) 2.3 \times 10^{-10} \text{ min.}^{-1}$) multiplied by Avogadro's number and the number of milliliters of the LSC sample. The half-life ($t^{1/2}$) of ^{14}C is 5,730 years. The molar ratio of unlabeled oleic acid to ^{14}C -oleic acid was used to determine the overall amount of oleic acid ligands exchanged onto the nanoparticles.

Mössbauer spectroscopic measurements were first conducted of two samples labelled oxidized and non-oxidized at UNCA's Materials Research Group Laboratory. Each sample received of colloidal suspension containing oleic acid coated iron-oxide nanoparticles was condensed by volatilization of hexanes. The condensed material was loaded into cylindrical polylactide (PLA) containers to a 3 mm depth. Prepared samples in containers were placed in a linear alignment with the oscillating ^{57}Co gamma source and the detector. Mossbauer spectra were recorded in the temperature range $11 \text{ K} < T < 293 \text{ K}$ using a Wissel spectrometer in constant acceleration mode with ^{57}Co source

in Rh matrix. Low temperature measurements were taken by placing the sample in a helium 4 K Cryostat (Advanced Research Systems, Inc.) Temperature probes were placed in the heat column and at the perimeter of the plastic sample container. Fitment was recorded in terms of isomer shift (δ), quadrupole splitting, magnetic hyperfine field (H_{eff}), line width, component area and a statistical criterion (χ^2). Instrumental error for the velocity scale or spectral point +/- 0.5 channel. Reference signal was folded against a standard α -Fe foil absorber at 295K to determine zero shift and optimal peak width.

Vibrating sample magnetometry (VSM) was used to analyze the magnetic properties of the samples. The samples were prepared by adding a few drops of nanoparticle solution onto the end of a cotton swab. The samples were analyzed at 300K in a 3T field with a Quantum Design VSM which runs on the physical property measurement system 6000 (PPMS 6000).

4.3 Results and Discussion

Aging Study

Iron oxide nanoparticles were synthesized via thermal decomposition, aged in toluene for 2, 7, and 30 days. The particles were characterized to determine size, size distribution, ligand surface coverage, and magnetic properties. The particles were employed in ligand exchange reactions with oleic acid and ^{14}C -oleic acid. Aliquots were collected throughout the reactions to monitor the exchange with time of reaction. The particles were characterized to determine size and size distribution, ligand surface coverage, and

magnetic properties. The aliquots were analyzed by LSC to determine the amount of radiolabeled oleic acid present on the surface and in solution (i.e. the supernatant) after exchange. Modelling of the reactions was used to determine kinetic parameters of the ligand adsorption. The results are provided in greater detail below.

4.3.1 TEM (Aging Study)

The synthesized particles were characterized via TEM to determine the particle size distribution. Analysis of the TEM images using ImageJ yielded size distributions (Figure 4.1) of the nanoparticles used in the initial aging study and in the oxidation study. The average diameter of the particles used in the aging study was 17.4 nm with a standard deviation of 1.56. The particles were analyzed via TEM after aging for 7 days and 30 days in toluene to verify that there were no changes in size or morphology due to aging. The particles which were aged for 7 days were on average 17.3 nm with a standard deviation of 1.53 and no significant size difference from the synthesized particles (aged 2 days) (unpaired t-test, $p=0.4283$). The particles which were aged for 30 days were 17.2 nm with a standard deviation of 1.57 and no significant size difference from the synthesized particles (aged 2 days) (unpaired t-test, $p=0.1181$).

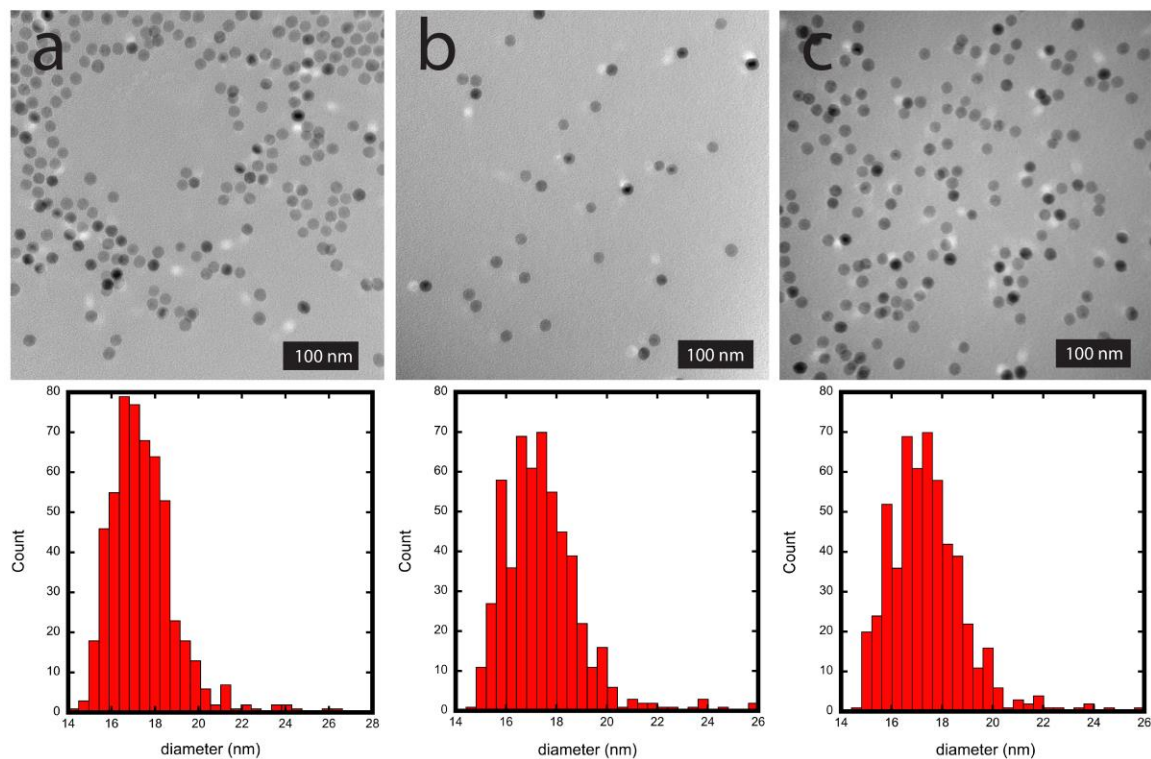


Figure 4.1. TEM image (above) and histogram of size distribution (below) of different aged nanoparticles. a) nanoparticles aged 2 days. b) nanoparticles aged 7 days. c) nanoparticles aged 30 days.

4.3.2 TGA (Aging Study)

The size results were further used to determine ligand surface coverage before modification via TGA. TGA results yielded percent weight loss of organic material on the surface of the nanoparticles before modification (Figure 4.2). Analysis of the data revealed an 85% weight loss between 200-500°C of the organic material on the nanoparticles synthesized and purified for use in the aging study (Table 4.1). This corresponds to a high surface coverage of approximately 180 chains/nm². The particles were further purified through a GPC column to remove the excess ligand. Further purification reduced the amount of organic material to approximately 48 chains/nm².

Although the surface coverage was still high, further purification may have resulted in destabilization of the particles.¹⁴

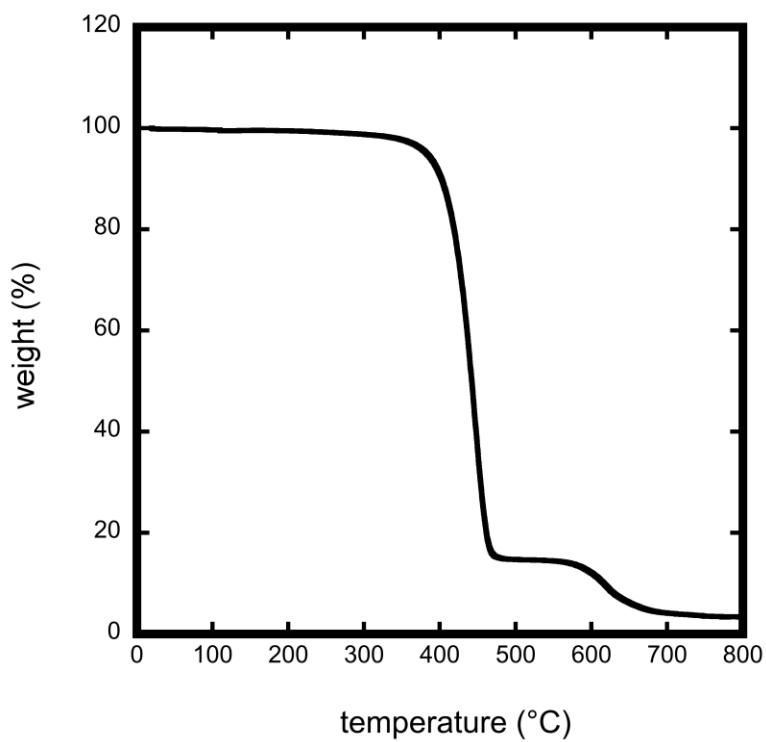


Figure 4.2. TGA of aging study nanoparticles after initial purification.

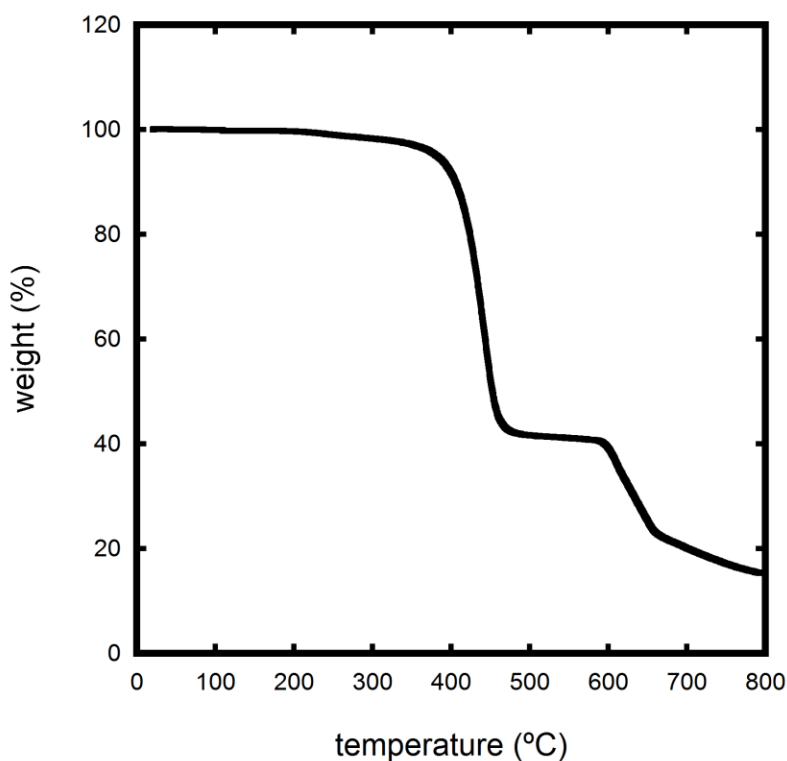


Figure 4.3. TGA of aging study nanoparticles after GPC purification.

Table 4.1. TGA results and surface coverages of nanoparticles used for aging study.

	Before GPC	After GPC
Weight loss (%)	85	63
Surface coverage (chains/nm²)	180	62

4.3.3 VSM (Aging Study)

VSM was used to observe the magnetic properties of the particles used for the aging study. The data was normalized to the iron content in grams which was determined using UV-Vis. The results are shown in Figure 4.4. The graph reveals a saturation

magnetization of 40 emu/g. This value is lower than that of bulk magnetite, but it compares well to other values reported in literature.^{165, 220} The particles were measured well after they were synthesized and employed in the aging study. Loss of solvent during storage and oxidation may have contributed to a decrease in the saturation magnetization.

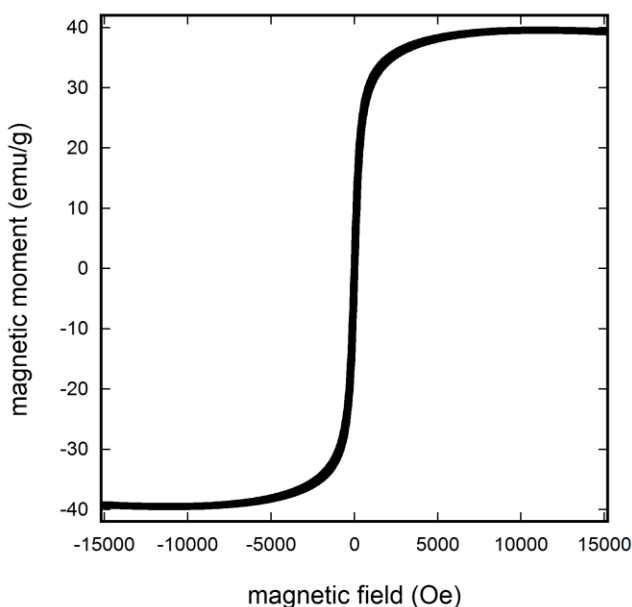


Figure 4.4. VSM results of nanoparticles used for aging study.

4.3.4 LSC (Aging Study)

The amount of radiolabeled oleic acid in each sample was determined using LSC. The data for each sample was normalized to the amount of nanoparticles present in the sample (based on determination of total iron via ICP-MS). The results were used to calculate the amount of radiolabeled oleic acid exchanged onto the surface of the nanoparticles and the amount of radiolabeled ligand remaining free in solution. The results from measurements of the initially cleaned particles (i.e. not purified via a GPC column) were used to

determine the overall amount of oleic acid on the particles and are shown in Figure 4.5. The graph illustrates a large amount of oleic acid on the particles at a 1:1 molar ratio of oleic acid. Additionally, there is some amount of newly introduced oleic acid present on the particles at the onset of the experiment. This seemed unlikely, therefore, the particles were further purified via passage through a GPC column and a syringe column to better remove the excess, unbound oleic acid. The results of the measurements after further purification are shown in Figure 4.6. The figure depicts a more accurate representation of the radiolabeled oleic acid present on the particles during the exchange reactions with 2 day, 7 day, and 30 day aged particles. Further cleaning of the particles decreased the amount of oleic acid on the particles and resulted in fewer outlying data points.

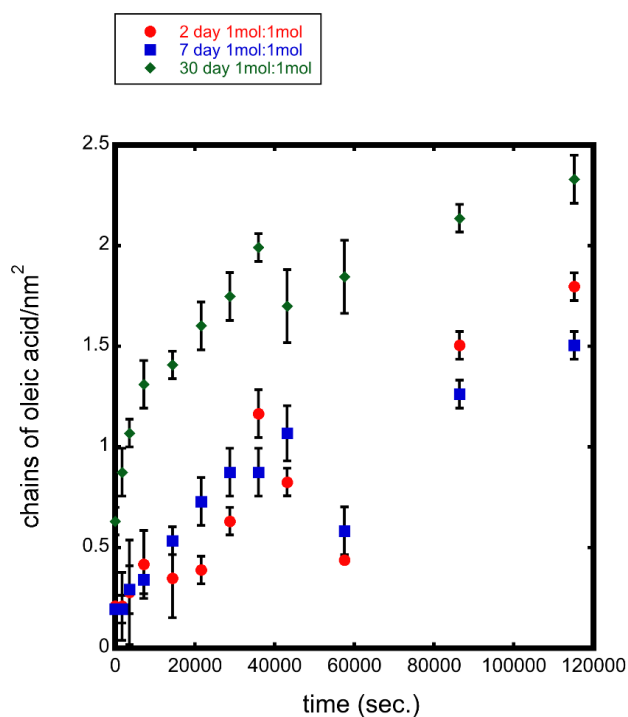


Figure 4.5. Amount of oleic acid (unlabeled and labeled) on the particles during exchange at different aging times and at a 1:1 molar ratio of oleic acid.

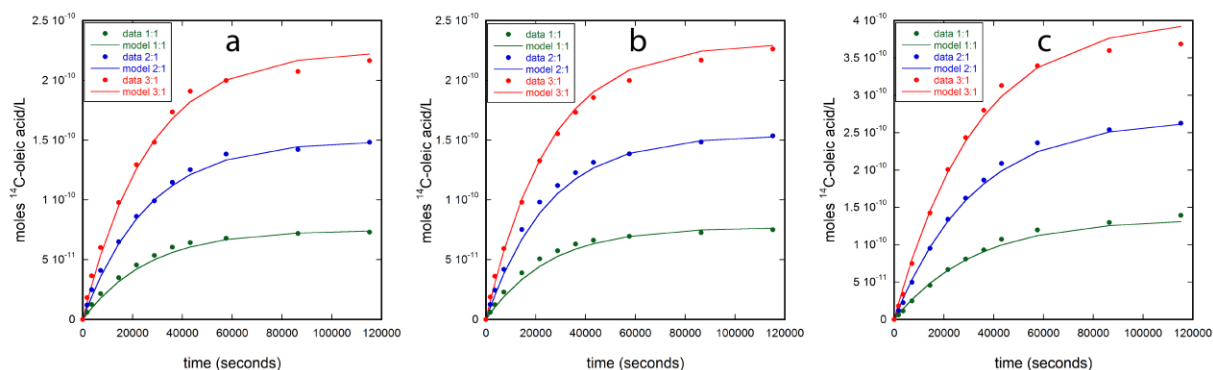


Figure 4.6. Amount of oleic acid exchanged on the 2 days (a), 7 days (b), and 30 days (c) aged nanoparticles at all molar ratios and first-order fits to data. Green lines represent the 1:1 molar ratio, blue is 2:1 molar ratio, and red is the 3:1 molar ratio.

The final results of the ligand exchange reactions of different aged particles are shown in Figure 4.7 and Figure 4.8. The graphs show a decrease in the concentration of radiolabeled oleic acid in the solution which corresponds to an increase in radiolabeled ligands adsorbing onto the surface. The decreases in concentration eventually plateau to a relatively constant concentration indicating an approach to equilibrium. The results revealed the changes in concentration of the ligands free in solution for each molar ratio are closely proportional to the increase in the initial concentration of oleic acid for all samples regardless of age. This indicates that no matter the core particle properties, addition of more ligand is a driving force in the exchange reaction (e.g., considering Le Chatelier's principle applied to equation 1). It is noteworthy that in Eq. 1 ^{14}C -oleic acid was used to track the behavior of all oleic acid (^{14}C labeled and stable) initially in the liquid phase. Results also revealed a large decrease in free ligand concentration after the particles were aged in toluene for 30 days. The aging process, between 7 and 30 days, allowed for increased extent of adsorption. As discussed below, we hypothesize this is

due to the presence of more available binding sites as the surface of the particles have become more oxidized.

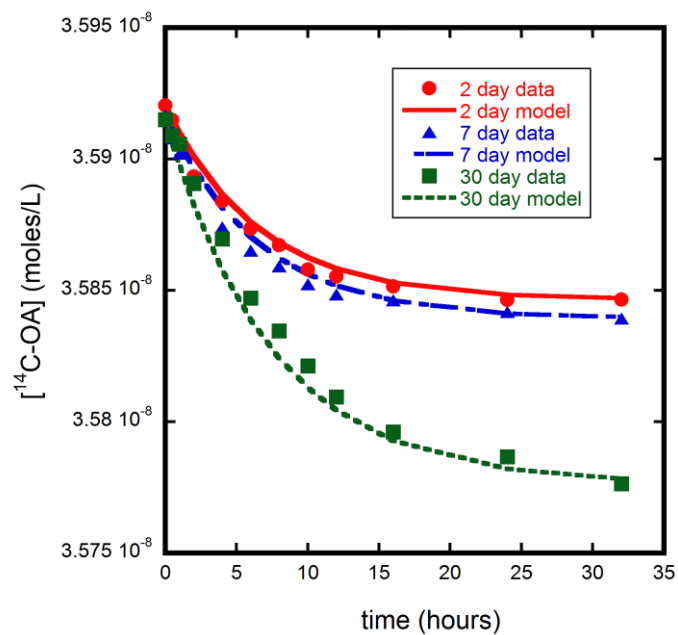


Figure 4.7. Amount of ^{14}C -oleic acid in solution during exchange with the 2 days, 7 days, and 30 days aged nanoparticles at a 1:1 molar ratio and model fits to the data.

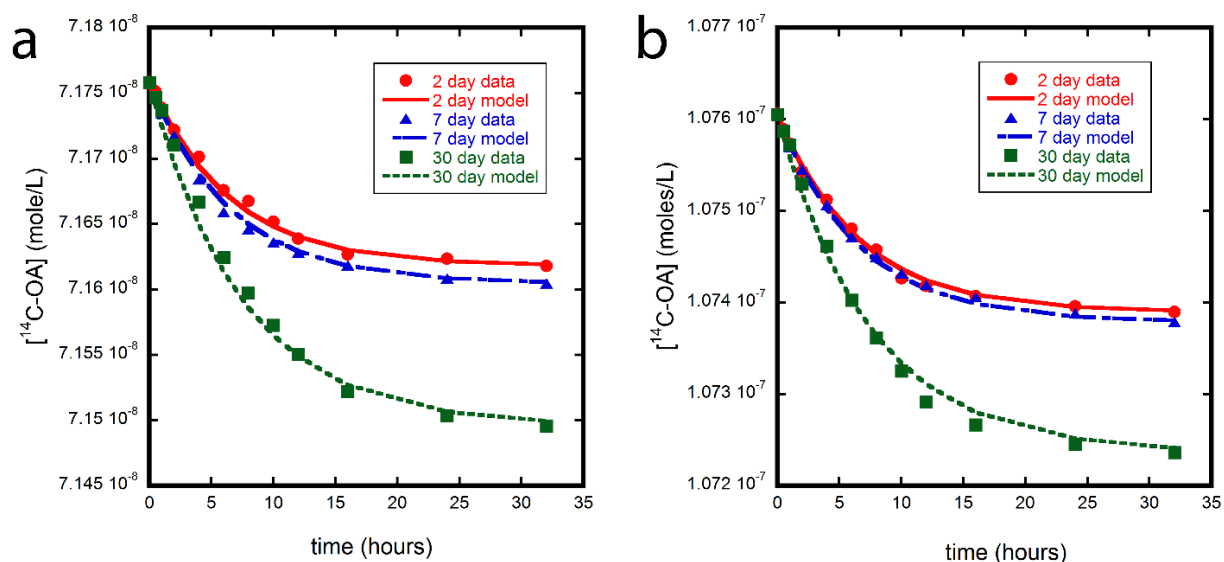


Figure 4.8. Amount of ^{14}C -oleic acid in solution during exchange with the 2 days, 7 days, and 30 days aged nanoparticles at a 2:1 and 3:1 molar ratio and model fits to the data.

4.3.5 Kinetic Modelling

The results as determined from LSC measurements were initially fit to models using differential equations to describe the forward and reverse reactions, or adsorption and desorption, and assuming first order kinetics. Non-linear regression analysis in Excel and the use of Excel solver allowed for modelling of the adsorption kinetics on the particle surface. The results are shown in Figure 4.6. This approach required the assumption that a single ligand was displaced by a single incoming ligand. Modelling the kinetics of loss of the oleic acid from the solution was used to avoid this assumption. In this approach, the data was fit to models using a linearized analytical solution and regression analysis. The kinetic analysis produced overall rate constants for the reversible reactions at 2 days, 7 days, and 30 days and yielded further insight into the true impact of aging on ligand exchange reactivity of oleic acid. Results in Figure 4.7 and Figure 4.8 illustrate the good

fit of the analytical solution to the experimental data. The similar trends and fits of the curves for each molar ratio indicate the reaction is first order and is independent of concentration. The linearized models (based on regression analysis) in Figure 4.9 and Figure 4.10 show a reasonably good fit to the linearized data. The changes in the slopes of the models directly correlates to the changes in overall rate constants shown in Table 4.2. This is illustrated in Equation 8, where the slope (i.e. overall rate constant) is the difference between the forward and reverse rate constants. The plots indicate a slow reaction which begins to level off after 10 hours. This time scale is large (on the order of hours) relative to the reaction rates observed with aged gold nanoparticles (on the order of minutes).²²⁴ This could be due to the fact that the reactions are not competitive exchange reactions. This could also indicate slower adsorption due to some physical barrier close to the particle surface.

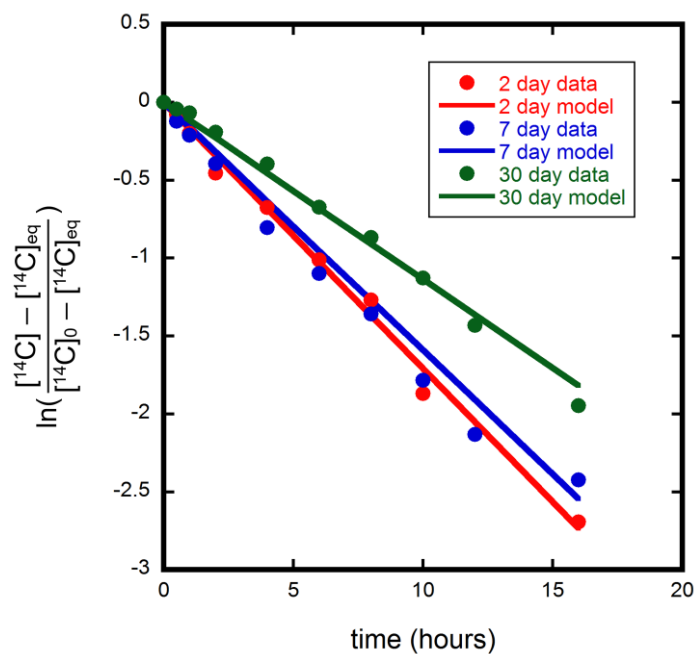


Figure 4.9. Linearized analytical solutions for 2 days, 7 days, and 30 days aged particles at a 1:1 molar ratio and the model fits based on linear regression analysis.

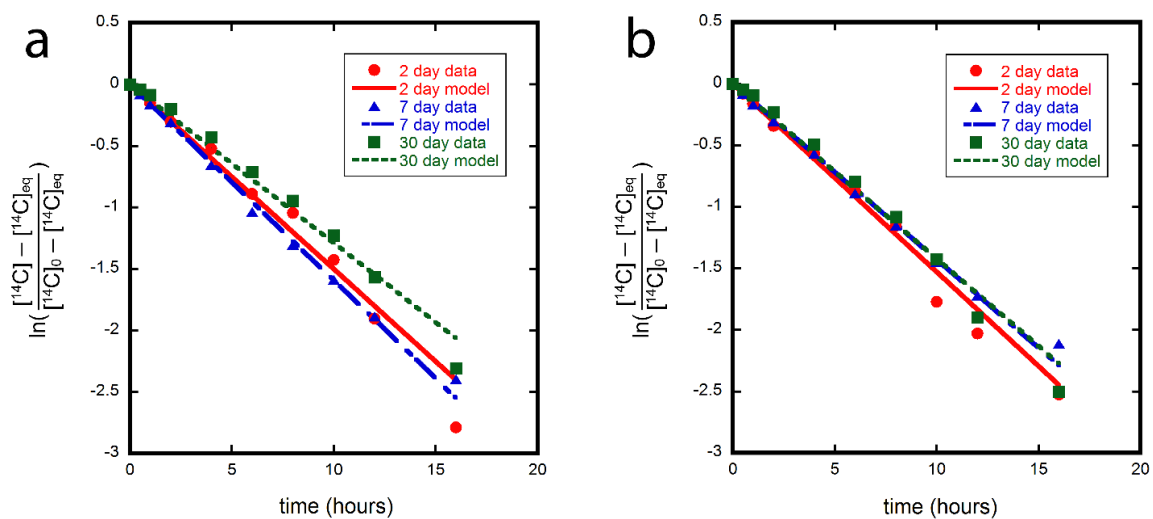


Figure 4.10. Linearized analytical solutions for 2 days, 7 days, and 30 days aged particles at a 2:1 and 3:1 molar ratio and the model fits based on linear regression analysis.

Table 4.2. Rate constants from exchange reactions as determined from modelling.

	2 days	7 days	30 days
Rate constant (sec.⁻¹ x 10⁻⁵)	4.4±0.3	4.2±0.2	3.6±0.4

The rate constants decrease with particle age, and the difference in the 2 day and 30 day constants is statistically significant as determined using an unpaired t-test ($p=0.0470$, $\alpha=0.05$) (Figure 4.11). However, the differences between the 2 day and 7 day constants and the 7 day and 30 day constants are not significant according to unpaired t-tests ($\alpha=0.05$, $p=0.64$ and $p=0.08$ respectively). This indicates that the difference between the forward and reverse rate constants is decreasing with particle age, and thus, the forward and reverse constants are becoming more similar. This could indicate an increase in the desorption rate with aging, assuming the forward rate (adsorption) does not change. This finding and the increase in the number of ligands leaving the liquid phase suggest a change at the surface of the particles has allowed for a larger mass of ligands to adsorb. The model does not yield unique solutions for the forward and reverse constants. Therefore, other possible explanations could be a decrease in the forward rate constant with an unchanging reverse constant or changes in both the forward and reverse rate constants resulting in increased similarity of the values. Overall, a change in ligand exchange reactivity with aging was observed, and further investigation was necessary to elucidate a reason or cause for these behaviors.

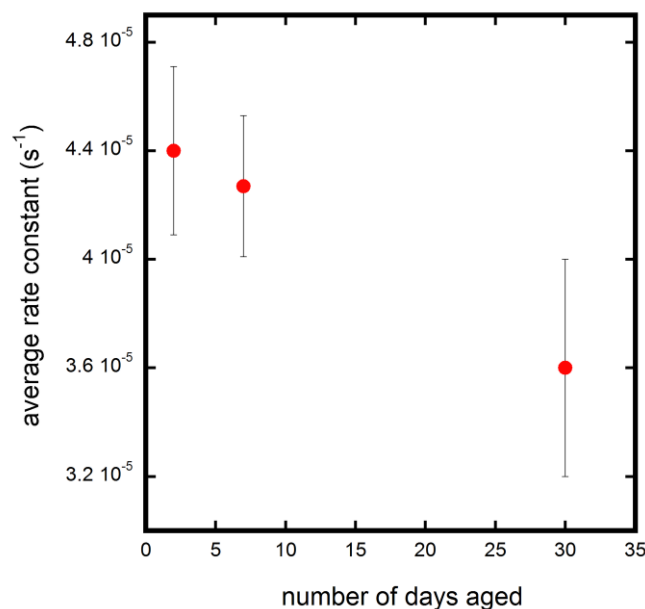


Figure 4.11. Average, overall rate constants for particles aged for 2 days, 7 days, and 30 days.

Oxidation Study

In a follow-up study of oxidation effects on exchange, nanoparticles were synthesized via thermal decomposition, and half of the resulting product was controllably oxidized. The unoxidized and oxidized particles were employed in ligand exchange reactions with oleic acid and ¹⁴C-oleic acid and aliquots were collected throughout the reaction. Again, the particles were characterized as described in detail below to determine size and size distribution, surface coverage of the ligands, and the magnetic properties. LSC was used to determine the amount of radiolabeled oleic acid present on the particles after exchange to address the effects of oxidation on extent of the reaction.

4.3.6 TEM (Oxidation Study)

The nanoparticles used in the oxidation study were measured with TEM before and after oxidation to ensure no changes in morphology and/or size occurred due to the oxidation process (Figure 4.12). Image analysis revealed no significant change with the unoxidized particles having an average diameter of 19.4 nm with a standard deviation of 1.56 and the oxidized particles having an average diameter of 19.3 nm with a standard deviation of 1.48 (unpaired t-test, $p=0.4209$). These findings agree with image analysis results from the aging study. Oxidation during aging does not yield changes in morphology or size which can be detected using standard TEM.

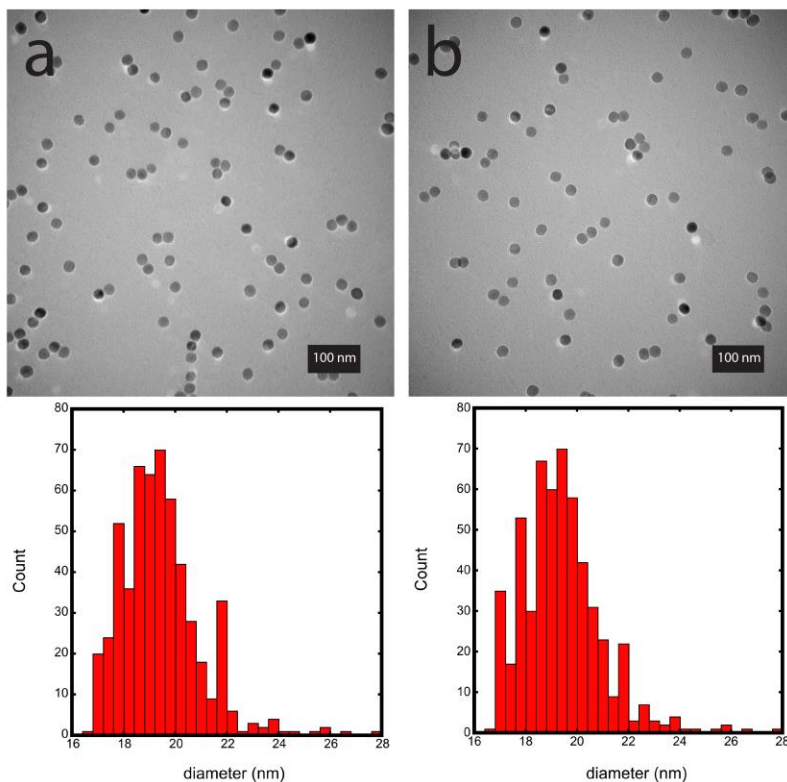


Figure 4.12. TEM images (above) and histograms of size distributions (below) of a) unoxidized and b) oxidized nanoparticles.

4.3.7 TGA (Oxidation Study)

TGA was used to determine surface coverage of the oleic acid on the unoxidized and oxidized particles before ligand exchange. The results yielded percent weight loss of organic material on the surface of the particles before modification (Figures 4.13 and 4.14). Analysis of the results of the unoxidized and oxidized nanoparticles revealed similar surface coverages of 62 chains/nm² and 57 chains/nm² (Table 4.3). Again, although the surface coverages were high, care was taken to not destabilize the particles through further purification.

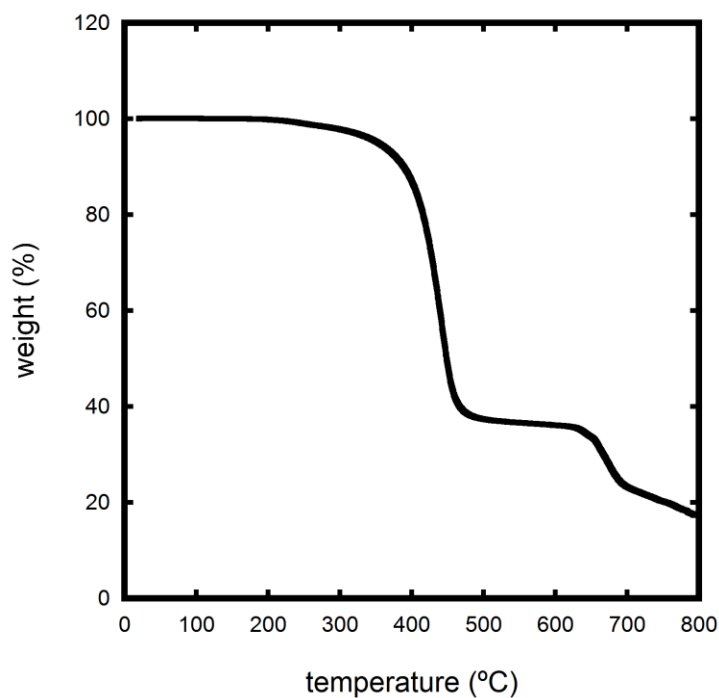


Figure 4.13. TGA results of unoxidized nanoparticles.

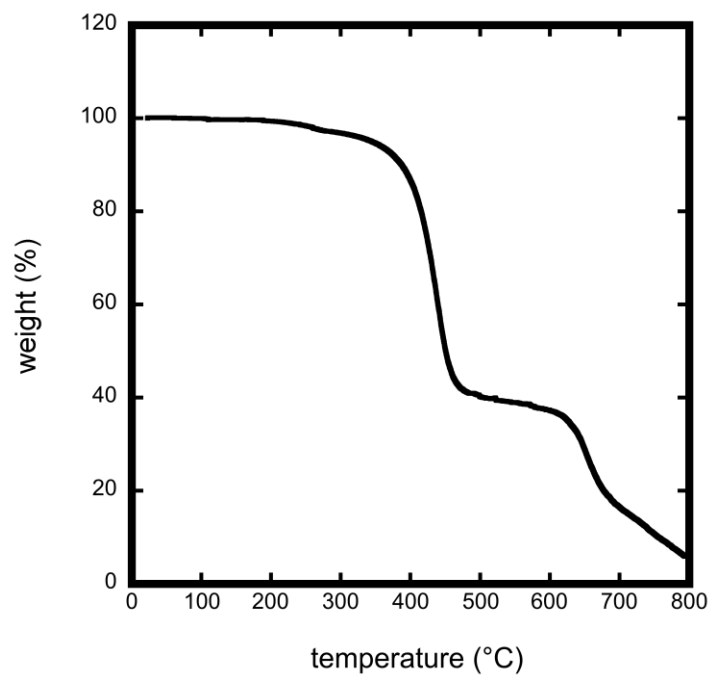


Figure 4.14. TGA results of oxidized nanoparticles.

Table 4.3. TGA results and surface coverages of unoxidized and oxidized nanoparticles.

	Unoxidized	Oxidized
Weight (%)	63	62
Surface coverage (chains/nm²)	60	58

4.3.8 LSC (Oxidation Study)

As previously mentioned, oxidation can affect ligand binding due to preferential binding of certain functional groups to different oxidation states of iron.¹⁰³ Furthermore, it is well known that oxidation of magnetite results in the formation of maghemite, and thus a

change in the ratio of Fe^{2+} and Fe^{3+} .²³⁰⁻²³³ Therefore, in order to investigate this phenomena, nanoparticles were synthesized, oxidized post-synthesis, and employed in a ligand exchange reaction with ^{14}C -oleic acid. Results of the adsorption of ^{14}C -oleic acid onto the particle surface are shown in Figure 4.15. The results reveal an increase in the amount of oleic acid present on the particles with oxidation. This is in agreement with the results in Figure 4.16. This graph indicates that less ^{14}C -oleic acid is in solution after exchange with oxidized nanoparticles compared to the unoxidized nanoparticles, and thus, more ligands adsorbed onto the oxidized particles. This finding suggests that oxidation during the aging process may be a reason for the observed increase in ligand adsorption. Wang and coworkers concluded that oxide shells, formed from oxidation of iron nanoparticles, are defective which creates reactive sites and alters the chemical reactivity of the surface.²³⁴ This could explain the increased availability of binding sites with aging/oxidation. Moreover, formation of defects at the surface could impact ligand binding, which in turn could influence spin canting and the magnetic properties of the particles.^{235, 236} Further characterization of the particle surface structure and oxide shell formation with aging would be necessary to confirm this reasoning. Overall, oxidation of the core could occur during the shelf-life of nanoparticles intended for various applications which could result in decreased stability of the particles depending on the ligand bound or it could promote ligand exchange once the particles are introduced into a competitive environment. Ligand exchange and/or instability of the particles could result in a drastic change of behavior of the particles and thus, an ineffectiveness for many applications.

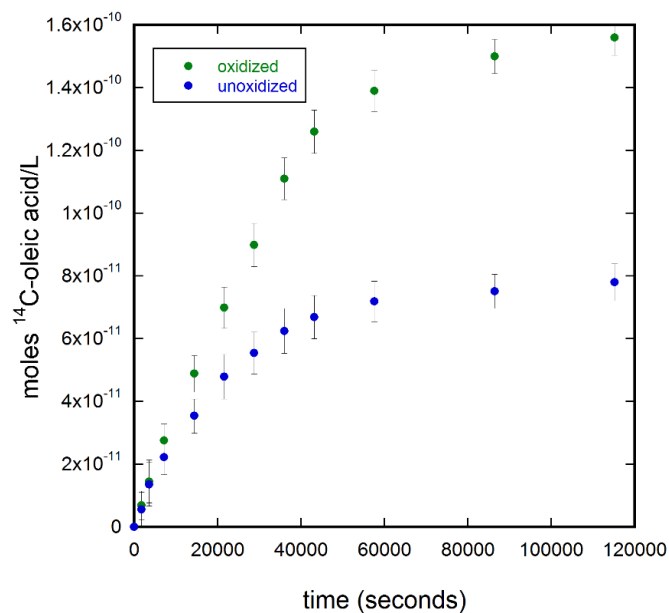


Figure 4.15. Adsorption of ¹⁴C-oleic acid onto the oxidized and unoxidized nanoparticles.

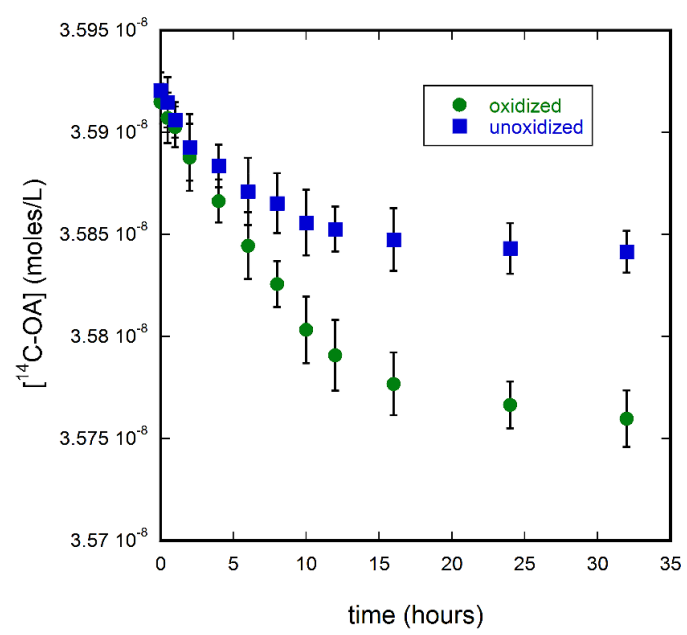


Figure 4.16. Loss of ¹⁴C-oleic acid from the solution during exchange with the unoxidized and oxidized nanoparticles.

4.3.9 Mössbauer Spectroscopy

While fitting the spectra the following components were identified (Table 4.4): two Fe^{3+} in tetrahedral sites (A1, A2), three Fe^{3+} in octahedral sites of non-disturbed nature (B30, B31, B32), two Fe^{3+} in octahedral sites affected by neighboring vacancies (B33, B34), Fe^{2+} in a non-disturbed octahedral site (B22), two Fe^{2+} octahedral sites with vacancy defects in the next nearest environment (B23, B24) and paramagnetic Fe^{2+} low spin state (LOS). Tetrahedrally coordinated sites show smaller values of isomer shifts (IS) compared to octahedral sites. Hyperfine field on Fe^{3+} nuclei in non-disturbed octahedral sites are highest in hematite and lowest in magnetite. Fe^{2+} shows hyperfine field lower by 100 kOe compared to Fe^{3+} because of the corresponding spin values 4/2 and 5/2. Therefore Fe^{2+} can be differentiated from Fe^{3+} if the Mössbauer spectra obtained as components are resolved in the fitting result.

Table 4.4. Results of fitted Mössbauer spectra. The table contains values for the isomeric shift (IS), hyperfine interactions (HI), and the quadrupole splitting (QS).

	IS (mm/s)	HI (kOe)	QS (mm/s)
Fe³⁺(A1)	0.32	523	0.03
Fe³⁺(A2)	0.31	504	0.03
Fe³⁺(B30)	0.51	545	-0.09
Fe³⁺(B31)	0.52	528	-0.02
Fe³⁺(B32)	0.51	506	-0.12
Fe³⁺(B33)	0.55	480	0.08
Fe³⁺(B34)	0.57	455	0.11
Fe²⁺(B22)	1.1	440	-0.10
Fe²⁺(B23)	1.1	420	-0.08
Fe²⁺(B24)	1.1	390	-0.11
Fe²⁺(LOS)	0.10	0	0.65

The coated nanoparticles (oxidized and unoxidized) provided for analysis were found to have iron oxide cores that are comprised principally of magnetite, maghemite and hematite phases (Table 4.5). The samples that were not oxidized demonstrated a moderate amount of ideal magnetite phase included. Evidence of the Verwey transition in nano-crystalline magnetite in nonstoichiometric nanometric powders were demonstrated

and are evidenced as likely in literature.²³⁷ The presence of magnetite in the unoxidized sample was confirmed by the Verwey transition being evident below 150K. When these particles were heated in oxidative conditions they were found to be comprised of mostly maghemite and little or no magnetite, or other oxides are observed. However, no iron was identified as magnetically ordered Fe²⁺ at 11 K which strongly suggests no ideal magnetite exists in the oxidized material. In general, core particles are composed of nano-sized crystallites (grains) of different phases of maghemite or magnetite solid solution with a possibility of less complex structured mineral (hematite or other inverse spinel) with a possible variable volume ratio from particle to particle. Signals appearing as Fe²⁺ doublets (i.e. paramagnetic material) could be unreacted reagent, surface interacting iron, or an iron complexed with carbon chain byproduct, as it may also interact with the pi bond of an olefinic acid's carbon chain or alkane fragment during the synthesis.

Table 4.5. Compositions of representative oxidized and unoxidized nanoparticle samples as determined by Mössbauer spectroscopy.

Sample	α-Hematite Fe₃O₄ (%)	γ-Maghemite Fe_{3-x}O₄ (%)	Magnetite Fe₂O₃ (%)	Other (%)
oxidized	10	87	0	3
unoxidized	18	63	16	3

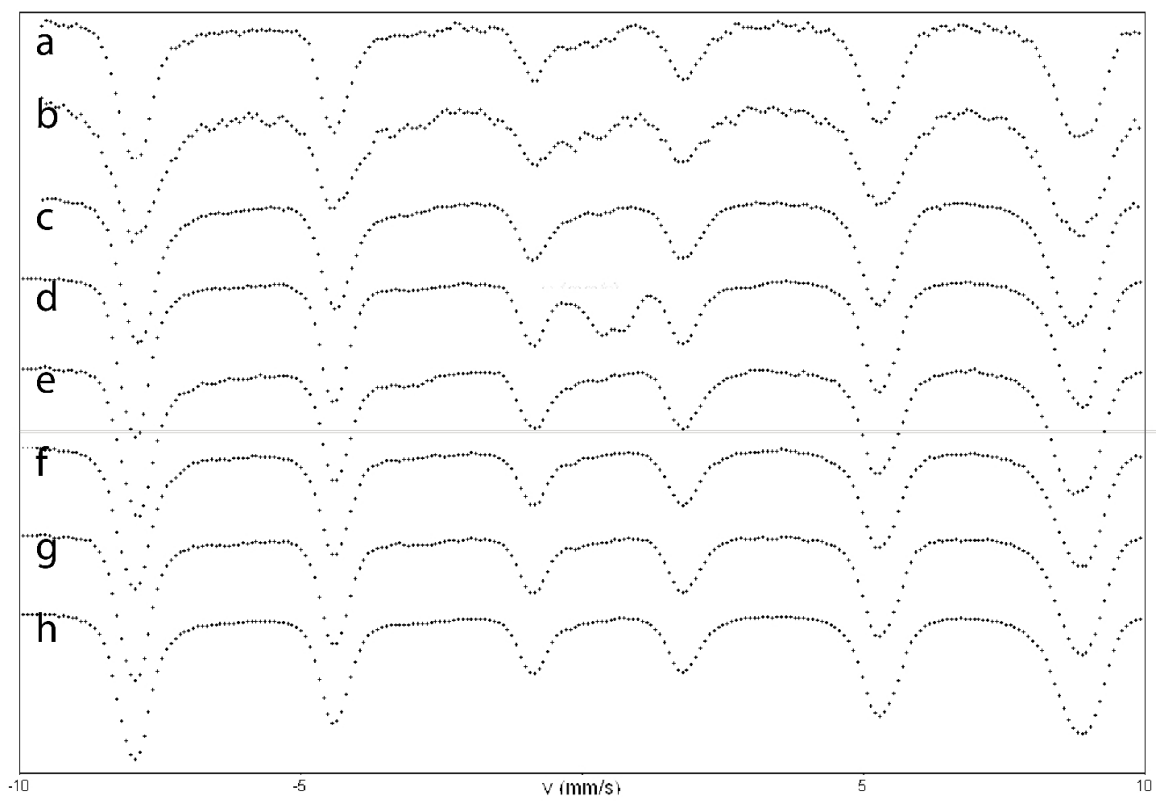


Figure 4.17. Mössbauer spectral results of the unoxidized (b, c, and e) and the oxidized (a, d, f, g, and h) particles at 12 K.

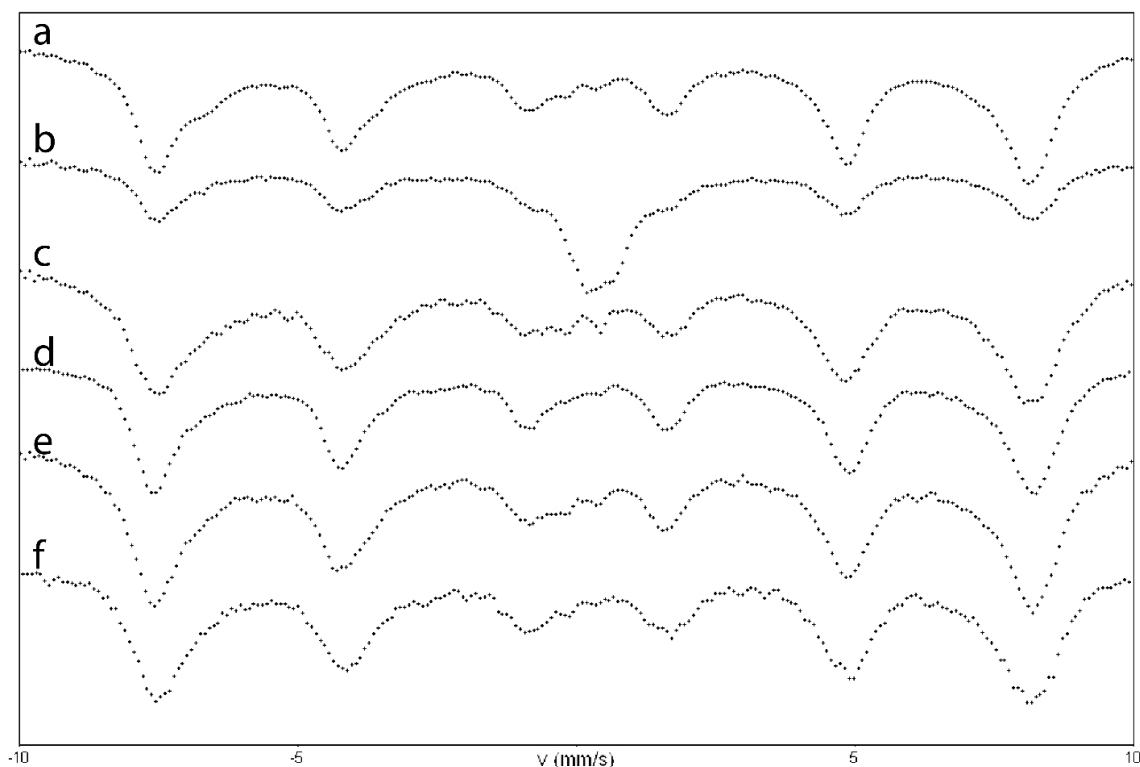


Figure 4.18. Mössbauer spectral results of unoxidized (a and c) and oxidized (b, d, e, and f) samples at 300 K.

4.3.10 VSM (Oxidation Study)

VSM was used to observe changes in the magnetic behavior of the particles with oxidation. Results are shown in Figures 4.19 and 4.20. Results show a high saturation magnetization of 70 emu/g for the unoxidized nanoparticles. However, the saturation magnetization of the oxidized particles is low at 27 emu/g. This is to be expected for the oxidized sample as bulk maghemite has a lower saturation magnetization than bulk magnetite. This further confirms that oxidation is the reason for the lower saturation magnetization of the particles used for the aging study. The difference in values between

the aging study particles and the oxidized particles could indicate a greater extent of oxidation during the oxidation procedure.

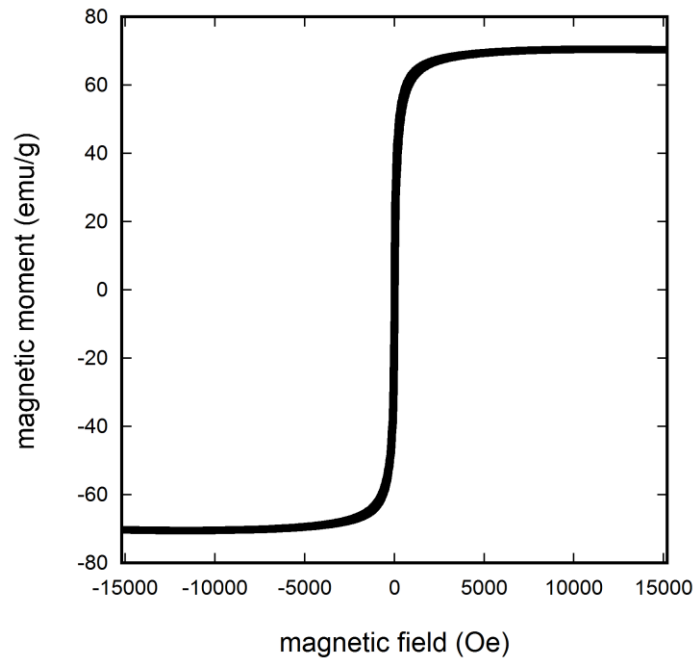


Figure 4.19. VSM results of the unoxidized nanoparticles.

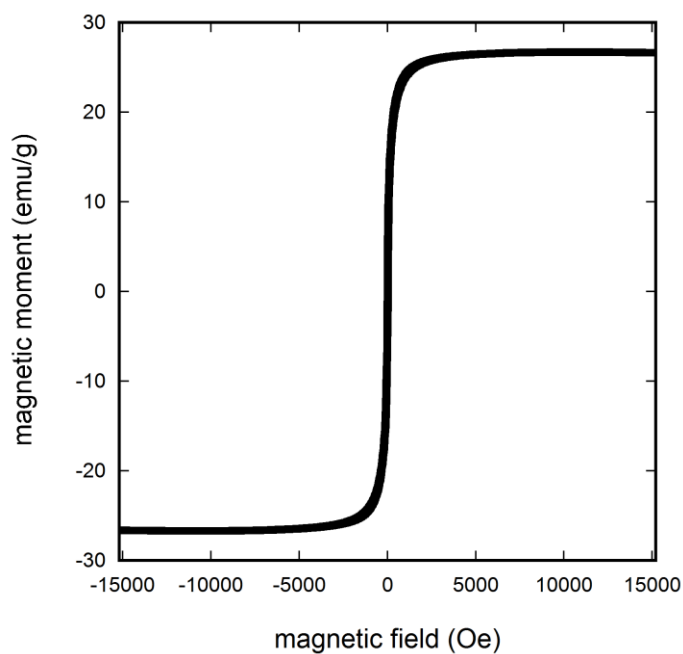


Figure 4.20. VSM results of the oxidized nanoparticles.

4.4 Conclusions

Radioanalytical techniques were successfully used to monitor the effects of aging on ligand exchange of iron oxide nanoparticles. The investigation revealed that aging of the particles results in oxidation which yields an increase of ^{14}C -oleic acid ligands adsorbed onto the particles. Mössbauer spectroscopy, used to confirm the composition of the oxidized and unoxidized nanoparticles, illustrated the oxidized particles are almost entirely maghemite. VSM results agree with this finding as evidenced by the decrease in saturation magnetization of the samples. Kinetic analysis of the results was used to determine how aging affected the overall rate of the reaction. The overall rate constants decreased with particle age, and the change in the constants from 2 to 30 days was significant. The results suggest the formation of a defective surface and an increase in

reactive sites occurs with oxidation which allows for more ligands to bind to the surface. The decrease in rate constants could be related to the larger mass of ligands adsorbing onto the particles or the reasoning may be more complex. This change occurs after a week of storage indicating that shelf-life of these materials could greatly impact the surface chemistry and thus, the stability of these particles. Furthermore, introduction of aged particles into a more competitive environment could result in a change of surface chemistry depending on the affinity of the anchor group for the aged surface. This would largely affect the performance of the particles for a desired application. Further investigation of aging impacts on particle surface structure, stability, and binding affinity and binding constants of various head groups could yield a more definitive understanding of the observed phenomena.

CHAPTER 5: CONCLUSIONS

The surface modification of iron oxide nanoparticles via ligand exchange and the factors which affect exchange were investigated and quantified in this work. Radioanalytical techniques demonstrated to be a useful tool for measuring ligand exchange with polymeric ligands and small molecule ligands. Liquid scintillation counting was used in combination with other common characterization methods to thoroughly quantify and qualify exchange on the surface of these materials. Furthermore, these techniques provided insight into the effects of binding group chemistry, reaction conditions, multidenticity, and nanoparticle aging and oxidation on extent and kinetics of ligand exchange.

In Chapter 2 radiolabeled, iron oxide nanoparticles were synthesized using ^{14}C -oleic acid as a radiotracer. The particles were modified post-synthesis with PEG ligands bearing different functional groups which are often used to bind and modify the surface of these materials. LSC measurements before and after modification of the particles revealed the extent of the exchanges and a binding hierarchy with catechols displacing the greatest amount of oleic acid during exchange. Furthermore, use of LSC exposed the pitfalls of other techniques like TGA to accurately quantify ligand exchange. Thorough characterization is necessary to understand the exchange process and optimize the polymer-particle systems for desired applications.

Chapter 3 revealed an expansion of these studies through inclusion of additional binding groups, comparison of reaction parameters like time, and comparison of monodentate and multidentate ligands. This work explored ligand exchange with some commonly used small molecule ligands bearing different functional groups and compared the corresponding exchange procedures for those ligands with a standardized procedure. LSC and FTIR measurements were used to observe increases in displacement of oleic acid with multidentate ligands bearing sulfonate and phosphonate groups and an increase in APTES ligands exchanged with increased reaction time. Furthermore, use of a standardized exchange procedure allowed for establishment of a binding hierarchy in which, again, catechols displaced the most oleic acid. These findings illustrate the complexity of ligand exchange and the importance of optimizing the many factors which influence it.

In Chapter 4, the effects of the core nanoparticle properties on surface chemistry were investigated. Oleic acid coated, iron oxide nanoparticles were aged in solution for up to 30 days and exposed to a solution of additional oleic acid containing ^{14}C -oleic acid as a radiotracer. LSC measurements of aliquots taken throughout the duration of the exchange reactions revealed an increase in the amount of ^{14}C -oleic acid exchanged onto the surface of the particles with particle age. Kinetic analysis of the data revealed a decrease in the adsorption rate and an increase in the desorption rate with aging. However, the change in the overall rate was not greatly affected by aging. Further investigation revealed oxidation of the particles, which occurs over aging time, led to an increase in the amount of radiolabeled ligands on the particles. These combined results

suggest an increased availability of reactive sites or binding sites with oxidation, possibly because of increasing defective nature of the core shell structure. Further studies of core shell structure, colloidal stability, and binding affinity of various head groups could elucidate a more definitive mechanism.

Overall, this work encompasses a review of our current understanding of ligand exchange of nanomaterials and establishes the utility of radioanalytical techniques to sensitively quantify the effects of various factors which influence ligand exchange. There are many variables to consider when modifying the surfaces of these materials. Good control of these parameters is critical to designing the ideal particle for the application. A thorough understanding of these parameters is necessary to achieve this goal.

CHAPTER 6: FUTURE WORK

This research yielded a better understanding of ligand exchange of iron oxide nanoparticles as it relates to binding group chemistry, aging of the particle core, and some reaction conditions. However, there are many other factors which affect ligand exchange. These factors could be thoroughly investigated and quantified via radioanalytical methods in combination with other specialized methods for determination of binding affinities and colloidal stability. Furthermore, synthesis and use of radiolabeled polymers would allow for further investigation of ligand structure effects on exchange. These methods could be applied to the study of other particle and biological systems.

6.1 Factors Affecting Ligand Exchange

This work has proven that radioanalytical methods are useful for sensitive quantification and monitoring of ligand exchange. There are many factors which remain to be investigated using these techniques. Temperature, ionic strength, pH, chain length, and tail group chemistry have all been shown to impact ligand exchange of nanomaterials.^{18, 238-240} Nanoparticle environment effects like pH and ionic strength are particularly interesting as these factors are very relevant to biological applications of iron oxides. Iron oxide nanoparticles are often dispersed in biological media or buffers for biological applications or research. The ability of the ligands to bind and stabilize the particles in these conditions is very important. Optimizing the pH of the solution has been shown to

be critical to ionizing and deprotonating the head group for better binding strength to the particle.²⁴¹ Furthermore, the presence of salts can impact binding strength especially in the context of charged synthetic and biological ligands where charge screening can take effect.²⁴² Therefore, it would be prudent to investigate effects of solution pH on binding efficacy of various and commonly utilized head groups. It would be particularly interesting to study the changes in extent of ligand exchange with solutions of caffeic acid or other catechols at varying pH values. Caffeic acid is prone to oxidation and is sensitive to pH changes.²⁴³ Additionally, introduction of salts in particle solutions could be explored to determine the effects on binding and dissociation of the ligands. This would be useful to investigate changes in ligand exchange with charged ligands like zwitterionic dopamine sulfonate. Isothermal titration calorimetry (ITC) could be used to determine binding affinities under these variable conditions. Control of these variables can directly impact the practical applications of these materials.

Ligand exchange and ligand binding are governed by thermodynamics. Therefore, it follows that temperature has an impact on these processes.²³⁸ Increased temperatures can have a positive impact on exchange especially in the case of diffusion limited reactions.²⁴⁴ Study of this factor is intriguing as it pertains to the use of iron oxide nanoparticles for magnetic hyperthermia. The particles are exposed to an alternating magnetic field which results in elevation of the temperature (Figure 6.1). Quantitative measurement of ligand coverage before and after exposure to an alternating magnetic field could allow for the understanding of bulk and local heating effects on ligand desorption and stability of the particles. Additionally, this study could be performed with

the particles suspended in biological media or buffers to observe any competitive binding. ITC measurements could also be used to probe thermodynamics of ligand exchange at different temperatures.

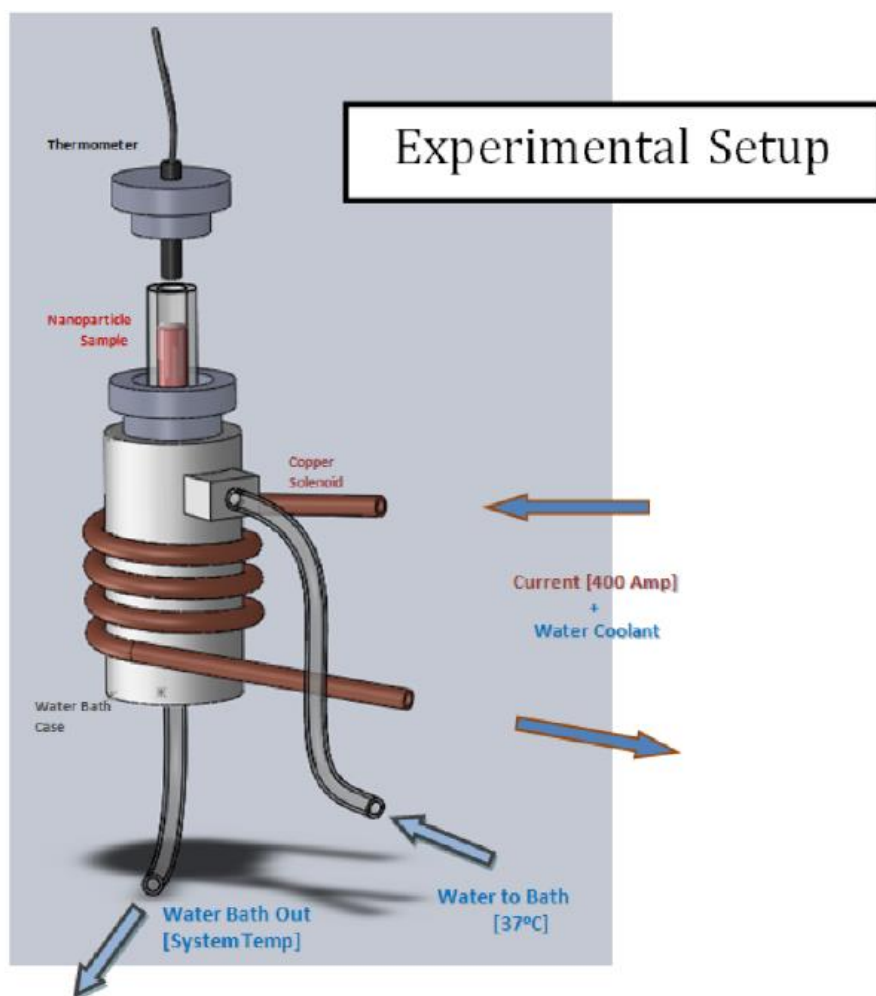


Figure 6.1. Exposure of sample to alternating magnetic field through copper coil. Setup for measuring specific absorption rate.

Ligands of increased chain length have been shown to bind more robustly and improve stability of particles via steric stabilization.^{245, 246} Furthermore, increased length has been

shown to increase acidity of the binding group and thus, the binding strength.²⁴⁷ Correlation of this factor with particle size would be a worthwhile investigation for optimization of polymer-particle systems for a variety of applications. Tail group chemistry has also been shown to affect ligand exchange rates depending on the electronic properties of the substituents.^{239, 248} Therefore, kinetic and thermodynamic studies of exchange with polymeric ligands with the same binding group but different tail groups could allow for greater understanding of this phenomena.

6.2 Radiolabeled Polymers

Polymers are attractive for surface modification of nanomaterials due to the ability to tailor molecular weight and end group chemistries. Synthesis of radiolabeled polymers could improve feasibility of studying the aforementioned factors. This would allow for direct measurement of adsorption of the desired ligand to the surface of the particles. Furthermore, the polymers could be synthesized with specialty chemistries to investigate binding group chemistry, tail group chemistry, and multidenticity. These properties are also desirable for modification of other materials such as drugs and other biological moieties. Conjugation of poly(ethylene glycol) (PEGylation) to drugs is common practice and requires polymers with reactive end groups.^{77, 135} Radiolabeling of the polymers allows for detection of the drug vehicle and, depending of the mechanism of delivery, the drug itself for biodistribution studies.^{249, 250}

Synthesis of ^{14}C -labeled PEG can be achieved either through end group modification of the polymer with a radiolabeled molecule or via synthesis of the polymer with a radiolabeled initiator so that the polymer backbone is inherently labeled. The first synthetic technique has been done using ^{14}C -succinic anhydride to modify PEG and allow for conjugation to doxorubicin. This is described in greater detail in Appendix A. Synthesis of inherently labeled polymer may be achieved via anionic, ring-opening polymerization of ethylene oxide using a radiolabeled initiator. An example of this is shown in Figure 6.2.

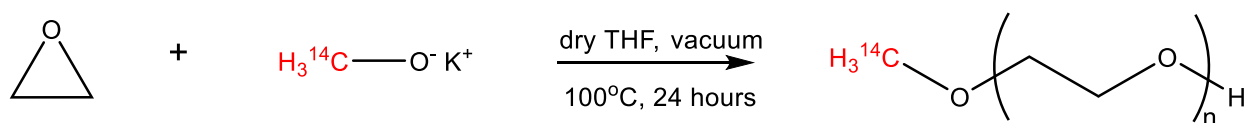


Figure 6.2. Synthesis of radiolabeled PEG via anionic ROP of ethylene oxide with ^{14}C -labeled potassium methoxide.

This method could be used to synthesize polymers which are monofunctional or difunctional for further reaction with drugs and other biological molecules. Furthermore, LSC is a sensitive technique which allows for the use of low activities. Synthesis and use of these materials grants many possibilities for expansion of this research.

6.3 Colloidal Stability Studies

Ligands do not only provide functionalization and impart solubility to nanomaterials but must also provide good colloidal stability for successful application. Colloidal stability is often observed through DLS measurements. Inclusion of colloidal stability

measurements is necessary to fully understand the ability of the ligands to perform as designed. Furthermore, colloidal stability measurements can be used to interpret particle behaviors due to charge interactions and steric and/or charge stabilization in application relevant environments. Observation of stability of the aged particles throughout the ligand exchange reaction or afterwards could illuminate mechanisms of action which resulted in the observed extents and rates of ligand exchange. Aging of the particles resulted in diminished magnetic response which contributes to the overall stability of the particles in solution. Changes in magnetic attractions of the particles could result in flocculation of the particles and thus, changes in the ability of ligands to reach the surface of the particles.

6.4 Other Metal and Metal Oxide Nanoparticles

This work has focused on surface modification of iron oxide nanoparticles, but the techniques developed in this work can be applied to other types of metal and metal oxide nanoparticles. Changes in the composition of the particles mean changes in the head groups which will bind to the particles. Substituted metal ferrites like cobalt and manganese ferrites have attracted interest due to the ability to tune the magnetic, electric, and catalytic properties by controlled introduction of metal ions into the lattice of the particles.²⁵¹ Determining a binding hierarchy of head groups for these types of particles and observing changes due to metal substitution would be of interest for progressing this research forward. Furthermore, use of other metal and metal oxide materials could present opportunities to include other radioisotopes for single or even dual-labeled

measurements. For example, phosphonates have been shown to bind well to titanium oxides.²⁵² ^{32}P could be used to label ligands for quantification of exchange with other ligands, possibly ^{14}C -labeled ligands. Dual-labelling could improve the accuracy of detection advance our knowledge of these complexes.

APPENDIX A

The material in Appendix A was taken from a Clemson University Honors Thesis written by Melanie Ghelardini on work performed by both of us.

RADIOLABELING OF POLYMER-DRUG CONJUGATES FOR EASIER QUANTITATIVE CHARACTERIZATION IN VIVO

Introduction

Polyethylene glycol (PEG) is commonly utilized in drug delivery systems as result of its tunable properties and its safety profile for biological use.²⁵³ This is done through a process known as PEGylation wherein polyethylene glycol is covalently attached to proteins or drugs, as a means to reduce immunogenicity and extend their circulation time in the body.²⁵⁴ For example, there is the PEGylated protein Adagen[®], which serves as an alternative to bone marrow transplants for patients suffering from severe combined immunodeficiency disease (SCID). It acts as an enzyme replacement therapy for the missing adenosine deaminase (ADA) for those suffering from SCID.²⁵⁵ There are also PEGylated small molecules drugs such as Prothecan[®], which is PEGylated in order to improve water solubility and *in vivo* drug circulation time, as camptothecin has poor water solubility and is physiologically unstable.²⁵⁵

Attachment of PEG is beneficial as it increases the size of the drug molecule, reducing kidney filtration. This size increase is based upon the fact that every ethylene glycol unit

is associated with at least two water molecules, making them five to ten times larger than a protein of similar mass.^{256, 257} PEGylation increases biocompatibility, solubility, and hydrophilicity characteristics of the molecule or drug, and protects against recognition and digestion from antibodies.²⁵⁴ PEGylation can be further utilized by bonding branched chains at specific points along the molecule to release PEG when exposed to specific outside stimuli, allowing for de-PEGylation and the release of the drug molecule.²⁵⁴ PEGylation also reduces the cytotoxicity of the drug, results in less leakage, and reduces immunogenicity.^{258, 259} Additionally the longer PEG chains used in PEGylation are not subjected to metabolism. Depending on the molecular weight they are eliminated from the body in two ways. PEG with a molecular weight smaller than 20kDa is removed through the kidneys, while those greater than 50kDa are removed through the liver. Generally renal elimination decreases with increasing PEG size, so larger PEGs will be more likely eliminated through the liver.²⁶⁰

The PEGylation process has undergone several advancements since its inception as a drug delivery and targeting mechanism. The original, first generation of PEGylated molecules resulted in a target molecule which was nonspecifically and permanently linked to linear PEG chains.²⁵⁴ This resulted in the formation of multiple isoforms with varying physiochemical and pharmaceutical features.²⁵⁷ The following, second generation resulted in a molecule which was PEGylated through the addition of branched chains at specific points along the molecule's backbone. This would enable the PEG to be released as a response to outside stimuli.²⁵⁴ It further decreases the amount of impurities and the side products that occur during the PEGylation process. Additionally, the introduction of

branched PEG decreases the molecule's immunogenicity and increases half-life in comparison with the first generation PEGylated molecule. This second generation, branched PEG addition unfortunately reduces the activity of the biomolecules attached to the PEG.²⁵⁷ A third generation of PEGylated biomolecules are currently being researched which do not limit the activity of the biomolecules. This would aim to minimize the trade-off between the strength of the drug and the circulation time, as is the case in second generation PEGylated drugs. Several techniques exist to do this, such as using releasable PEG conjugates as a prodrug approach. Another technique creates customized PEGylation sites on the protein or drug, reducing steric hindrance.²⁵⁷ As of 2011, eleven PEGylated drugs were FDA approved for use.²⁵⁴ In 2015 an additional three PEGylated drugs were approved and available on the market, with over twenty more PEGylated drugs in the process of conducting clinical trials.²⁵⁷ As a result of recent innovations, PEGylated drugs are potentially a multi-billion dollar market.²⁵⁷ This financial outlook, and the beneficial characteristics imparted to a drug through PEG addition, exemplifies the viability of PEGylation and the use of polyethylene glycol in the medical industry.

The polymer-drug conjugate synthesized must be analyzed to ensure its efficacy prior to use. It must be verified that the PEGylated drug is biocompatible and nontoxic to the subject. It is further necessary to know the fate of the PEGylated compound in the subject's body, and also in what quantities and what organs it concentrates. This is done through biodistribution studies, which are designed to inform the need of additional preclinical studies.²⁶¹ It is additionally necessary to meet standards of homogeneity, pyrogenicity, and to verify that the activation and coupling techniques are reproducible.²⁵⁶ Current methods

of biodistribution analysis and quantification have limitations in their effectiveness and in their accuracy. One such method involves the addition of a fluorescent dye such as the NIR fluorophores Cy5,5 and Cy7 as a method of tracking the PEGylated biomolecules in the subject.^{262, 263} Similar attachment and optical tracking can be completed through the use of quantum dots.^{264, 265} Modification with the dye molecule or quantum dots enables the non-invasive, qualitative visualization of the location of the biomolecule through the use of a non-invasive near infrared fluorescence imaging system (NIRF). This further facilitates the creation of an approximate time dependent excretion profile by showing the total NIRF intensity per region in the body, calculated as a function of time.²⁶³ However, modification with a dye molecule or quantum can alter the chemistry and limit the functionalization of the polymer, so other methods of analysis should be considered.

Another method of analyzing the PEGylation and the biodistribution of PEGylated drugs is through a radiolabeling process.^{249, 250, 266-268} Labeling with radioisotopes is advantageous because they are high in sensitivity and easily detectable, allowing for easy visualization, traceability, and quantification.²⁶⁹ In this method, a radiolabeled component is attached to the polymer-drug conjugate, acting as a tracker. These radiolabeled components enable the use of liquid scintillation counting (LSC) and positron emission tomography (PET) imaging to qualitatively and quantitatively analyze the activity, and thus the amount of polymer-drug conjugate in the body. It also provides information regarding which organs contain the polymer-drug conjugate in the greatest quantities. Commonly utilized radiolabeled components are Indium-111, Copper-64, Hydrogen-3, Iodine-125, etc.^{249, 250, 266-268} Similar to the usage of dyes and quantum dots to quantify and track PEG,

the usage of radiolabeled trackers also has shortcomings. The attachment of the radiolabel tracker requires the alteration of the of the polymer-drug conjugate, and has the capability to alter the chemistry and limit functionalization of the system, as the radiolabeled component must bind to a functional group present on the conjugate system.

One method which does not alter the chemistry of the polymer-drug complex is labelling with carbon-14. Recent studies document use of this as a tracking mechanism.²⁷⁰⁻²⁷⁴ Carbon-14 maintains the integrity of the polymer drug conjugate, as radiolabeled carbon-14 can simply be inserted along the backbone of the polymer chain, replacing ordinary carbon-12 groups. As a result, none of the functionalization groups are altered or made unavailable, as is the case in the other methodologies.²⁶⁹ This labeling with carbon-14 is clearly beneficial in comparison with other methods, as it preserves molecular structure through the lack of radiolabeled pendant groups, and produces few changes in chemical or biological properties.²⁶⁹ This direct insertion along the backbone reduces the risk of label cleavage and oxidation. Furthermore, there is a distinct isotopic signature peak present in the mass spectra of the diluted carbon-14 compound, which is beneficial during analysis.²⁶⁹

Utilizing a drug or molecule that is inherently fluorescent is another option used in studies. This is particularly true of the drug doxorubicin.^{272, 275, 276} Doxorubicin belongs to a class of anthracycline drugs, which are often used to monitor the drug's location within the delivery system and as a means of assessing the drug's interactions with DNA and other macromolecules present in the system.²⁷⁷ This assessment is enabled by the chemical structure of the amphiphilic drug, which contains a fluorescent hydroxy-

substituted anthraquinone chromophore and a hydrophilic aminoglycosidic chain.²⁷⁷ As a result of this structure, the doxorubicin is UV-Vis active and presents red fluorescence.²⁷⁸ By utilizing doxorubicin as the drug conjugate, a secondary dye component is not required, because the fluorescence of doxorubicin is inherent. This lack of a dye pendant group means that the chemical structure and thus the integrity of the polymer drug conjugate is maintained and the chemical properties of the system are unaltered.

This study utilizes the beneficial characteristics of carbon-14 labeling and the fluorescent characteristics of doxorubicin as a means of creating a novel tracking and analysis method. It sensitively quantifies the fate and biodistribution of both the polymer and the drug utilized when the conjugate is inserted into a biological system. PEG-methyl ether polymer was modified with labeled succinic anhydride to create a PEG with an overall activity of approximately 200 nCi. This methyl ether component was necessary as previous research has shown that stable linkage between PEG requires either an active carbonate, active ester, aldehyde or tresylate group for successful modification. This reaction created a further carboxylic acid group, which was used in a secondary reaction to attach the doxorubicin. Fourier transform infrared spectroscopy (FTIR) was utilized to confirm the presence of the carboxylic acid group, while liquid scintillation counting (LSC) was used to verify that the desired activity was produced. EDC chemistry was then used to react the primary amine present on doxorubicin with the previously attached carboxylic acid group on the PEG. The chemical components utilized to create this polymer drug conjugate are shown as Figure A1. This compound was dialyzed and later analyzed through FTIR, UV-Vis, and LSC to ensure attachment of the doxorubicin and

that the activity of the sample remained in the desired range. This design is beneficial as it potentially provides two different methods of tracking the polymer drug conjugate in a biological system, through the radiolabeled carbon-14 and the fluorescent doxorubicin, without altering the typical structure or properties of either component.

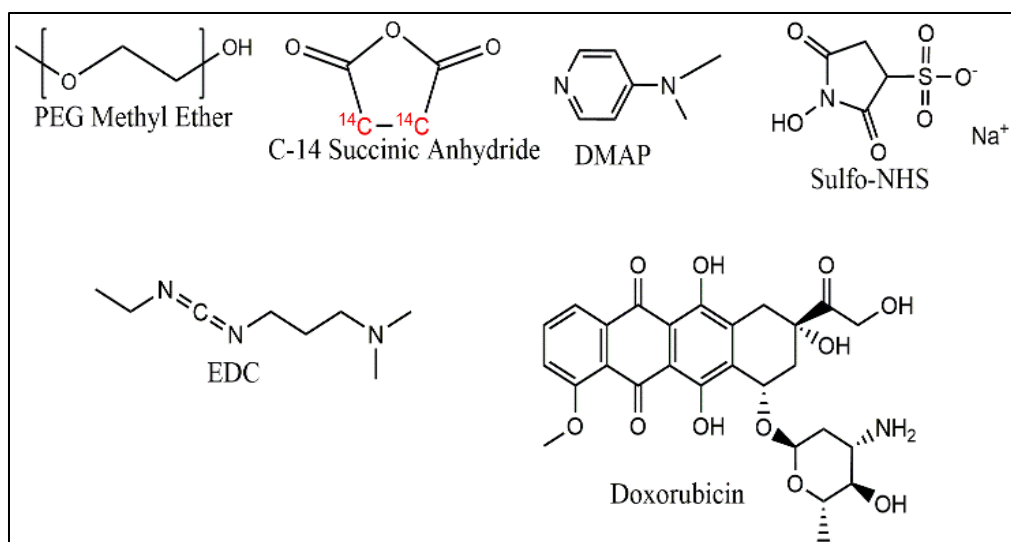


Figure A1. Reagents used for synthesis of ¹⁴C-labeled PEG-doxorubicin.

Experimental

Materials

Poly(ethylene glycol) (PEG) methyl ether (M_n 10,000 g/mol), N-hydroxysulfosuccinimide sodium salt (sulfo-NHS) (98%), 4-dimethylaminopyridine (DMAP) (>99%), 4-(2-hydroxyethyl)-1-piperazineethanesulfonic acid (HEPES) buffer solution (1 M, pH 7.3), and succinic anhydride (>99%) were purchased from Sigma Aldrich. Doxorubicin hydrochloride (>99%) was purchased from LC Laboratories. 1-Ethyl-3-(3-

dimethylaminopropyl) carbodiimide (EDC) was purchased from TCI America. Succinic anhydride (2,3-¹⁴C) was purchased from American Radiolabeled Chemicals. Optiphase 'HISAFE' 3 liquid scintillation cocktail was purchased from Perkin Elmer. Spectra/Por® dialysis membranes (MWCO 1000 Da) were purchased from Spectrum Labs. Tetrahydrofuran (THF; 99%) was purchased from BDH Chemicals.

Synthesis of radiolabeled carboxylic acid functionalized PEG

The first step in creating the polymer-drug conjugate was to form radiolabeled carbon-14 linkages along the backbone of the polymer. This involves the modification of polyethylene glycol (PEG) methyl ether of 10,000 g/mol molecular weight through the addition of carbon-14 radiolabeled succinic anhydride, with a specific activity of 5mCi/mmol. THF was used as a solvent and DMAP was used as a catalyst to promote the reaction. Relative to the PEG methyl ether, the DMAP and succinic anhydride were added in a molar ratio 1.0:0.01:1.1. This resulted in the addition of 1.2 mg PEG (0.12 μmol), 0.16 μg DMAP (1.2 nanomoles), and 700 nCi of ¹⁴C-succinic anhydride (14 μg; 0.14 μmol) to an Erlenmeyer flask. This reaction proceeds according to Figure A2, and results in the formation of two radiolabeled carbon-14 groups along the chain and the creation of a carboxylic acid group, which is necessary for the later attachment of doxorubicin. This radiolabeled polymer was dried, transferred to water and purified through dialysis for use in the next reaction. Dialysis tubing of a molecular weight cut-off of 1000g/mol was utilized in this step, and the polymer was dialyzed for 48 hours. Only a small amount of

polymer was synthesized, so FTIR and LSC characterization were not completed at this point.

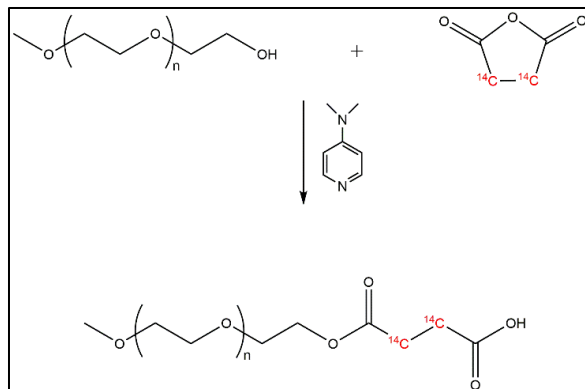


Figure A2. Modification of PEG with labeled succinic anhydride.

PEGylation of doxorubicin

Doxorubicin was attached through EDC chemistry in an aqueous solution. Sulfo-NHS was utilized in conjunction with EDC, in comparison with pure NHS, which is utilized when THF is the solvent. The sulfo-NHS was added in a 1.0:1.2 molar ratio relative to the PEG functionalized with the carboxylic acid, as was the EDC. After allowing this to react for four hours, doxorubicin was added to the solution in a molar ratio of 1.0:1.5 relative to PEG and doxorubicin. Roughly 1.2 mg (0.12 μmol) of the carboxylic acid functionalized PEG was added to a flask, in conjunction with 31 μg (0.14 μmol) sulfo-NHS, 27 μg (0.14 μmol) EDC. This solution was allowed to react for four hours and then 98 μg (0.18 μmol) doxorubicin was added. This two-step reaction proceeds according to Figure A3 and results in the formation of the desired radiolabeled polymer drug conjugate. This component was dialyzed in tubing with a molecular weight cutoff of 8000 g/mol in order to purify the

compound. LSC and UV-Vis were used to determine the activity and amount of doxorubicin conjugated in the recovered sample.

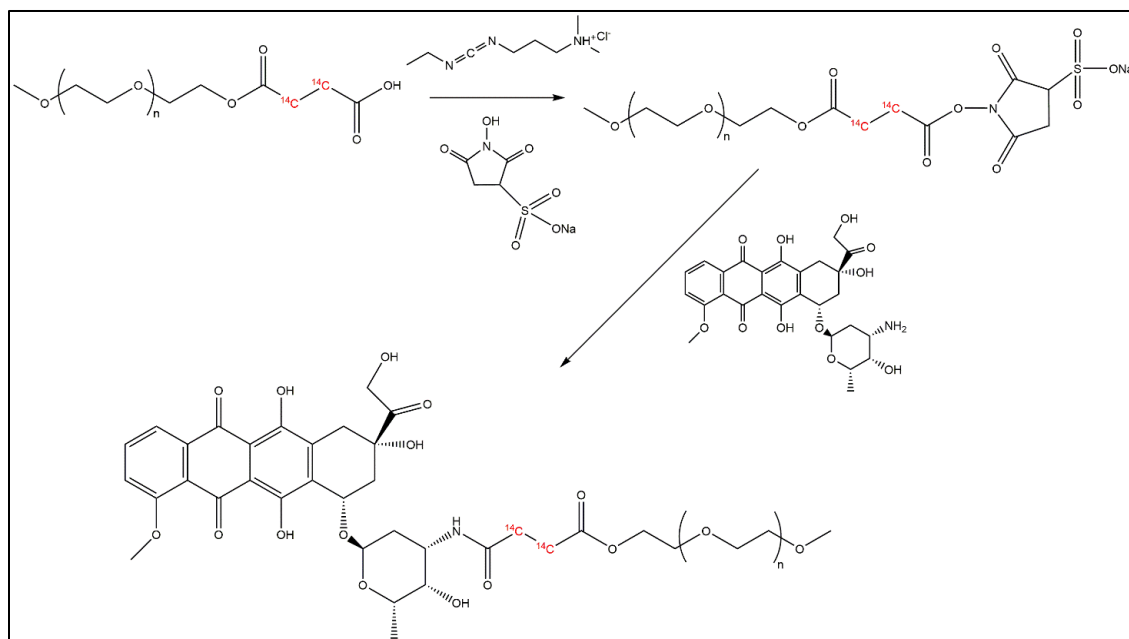


Figure A3. PEGylation of doxorubicin with ^{14}C -labeled PEG-succinic acid.

Synthesis of unlabeled PEG-doxorubicin

Unlabeled PEG-doxorubicin was synthesized separately and combined with the radiolabeled material to control the final specific activity of the sample. The same chemistry was used in this synthesis. For the first step, the attachment of the carboxylic end group, 1.815 g (0.1815 mmol) of PEG methyl ether was added to THF. After this, 19.98 mg (0.200 mmol) of succinic anhydride was added to the same flask representing a 1.0:1.1 ratio between the PEG and the succinic anhydride. 0.2217 mg (1.815 μmol) of DMAP was then added, indicating a 1.0:0.01 molar ratio once again. This compound

was then purified through dialysis as described earlier and dehydrated through a freeze dryer to revert it to a solid polymer rather than a liquid solution.

Attachment of the doxorubicin proceeded through the use of EDC chemistry as previously described. 11.3 mg (1.12 μmol) of the carboxylic acid modified PEG was added to an Erlenmeyer flask. After this sulfo-NHS was added in a ratio of 1.0:1.2 relative to the PEG, such that 0.261 mg (1.343 μmol) was added to the flask.

Subsequently, EDC was added in this same ratio relative to PEG, resulting in the addition of 0.208 mg EDC (1.343 μmol). This reaction was allowed to run for four hours prior to adding doxorubicin in a 1.0:1.5 ratio relative to the PEG functionalized with carboxylic acid. This ratio resulted in the addition of 0.912 mg (1.678 μmol) doxorubicin to the Erlenmeyer flask. After allowing the system to react, the compound was purified through dialysis, after which it was combined in an aqueous mixture with the previously radiolabeled components. This was done by adding the radiolabeled polymer with the unlabeled polymer in an aqueous solution and agitating it. The final polymer-drug conjugate was characterized for future use in a biodistribution study.

Characterization

Several methods of characterization were completed to confirm that the polymer-drug conjugate was properly prepared and had the appropriate chemistry for its end use. The first test completed was FTIR, verifying that the desired chemistry was present. A droplet of the polymer-drug conjugate was placed onto the sample plate and analyzed

through use of the Thermo Scientific Nicolet 6700. By utilizing FTIR it was possible to determine that the structure contained the appropriate peaks, and thus that the desired ether group, aromatic alkene group, and the carbonyl group were present in the final conjugate. This was the first step in verifying the product created through the synthesis steps was representative of the desired conjugate.

After completing FTIR to determine the chemistry of the synthesized product, the presence and concentration of doxorubicin was doubly verified through the use of UV-Vis spectroscopy. UV-Vis determines the compound's valence electrons, in both its excited and ground states. A small sample was examined through the use of a Varian Cary 50 Bio UV-Visible Spectrophotometer. The sample has a distinctive absorbance value, which can be used to calculate the concentration of doxorubicin present in the sample. This is done by comparing the sample's absorbance with a calibration curve created from samples of known doxorubicin concentration. This is a beneficial form of analysis, as it not only verifies the presence of doxorubicin, but also the concentration of the doxorubicin present in the polymer-drug conjugate. This is useful for the dosage determination in the biodistribution study.

The final method of analysis involved the calculation of the sample's activity through LSC calculations. A few microliters of sample were added to a vial containing 7 mL of LSC cocktail and input into the Perkin Elmer TriCarb 2910TR machinery for analysis. This machinery provides information regarding the number decays per minute, which can be converted into a representation of activity per milliliter. This was beneficial as it

verified that the activity of the sample was within the desired 100 nCi range for detection within the biological system. After completing these characterization methods, the sample was then deemed ready for use in the biological subject in the biodistribution study.

Results and Discussion

Several characterization techniques were completed during the synthesis of the polymer-drug conjugate, namely UV-Vis, LSC, and FTIR. FTIR was completed on the unlabeled carboxylic acid functionalized PEG, and on the final product of the combined radiolabeled/unlabeled PEG-Dox conjugate. LSC was completed on the radiolabeled polymer-drug conjugate to verify the radionuclide identity and for calculation of its activity. Finally, UV-Vis was used to determine the success of the dialysis procedure, and in the calculations which determined the combining procedure of the labeled and unlabeled polymer-drug conjugates.

As stated previously, the first method of characterization completed was FTIR. After completing the first modification with the unlabeled succinic anhydride, the success of the modification was determined through FTIR. This was not completed for the radiolabeled carboxylic acid functionalized PEG as a result of the small volume of sample created. The spectra gathered for the unlabeled component served as a comparative, representative spectra for the radiolabeled component. The results of this analysis are shown in Figure A4. The peak around 1114 cm^{-1} represents the ether linkage of $\text{CH}_2\text{-O-CH}_2$ in the polymer

chain backbone, while the peak around 1722 cm^{-1} represents the carbonyl C=O pendant group. The peak present around 2900 cm^{-1} is indicative of background substances or unreacted components of the reaction, and is not vital for further analysis. This FTIR visualized the success of the reaction, and allowed for the next step, the attachment of doxorubicin to be completed.

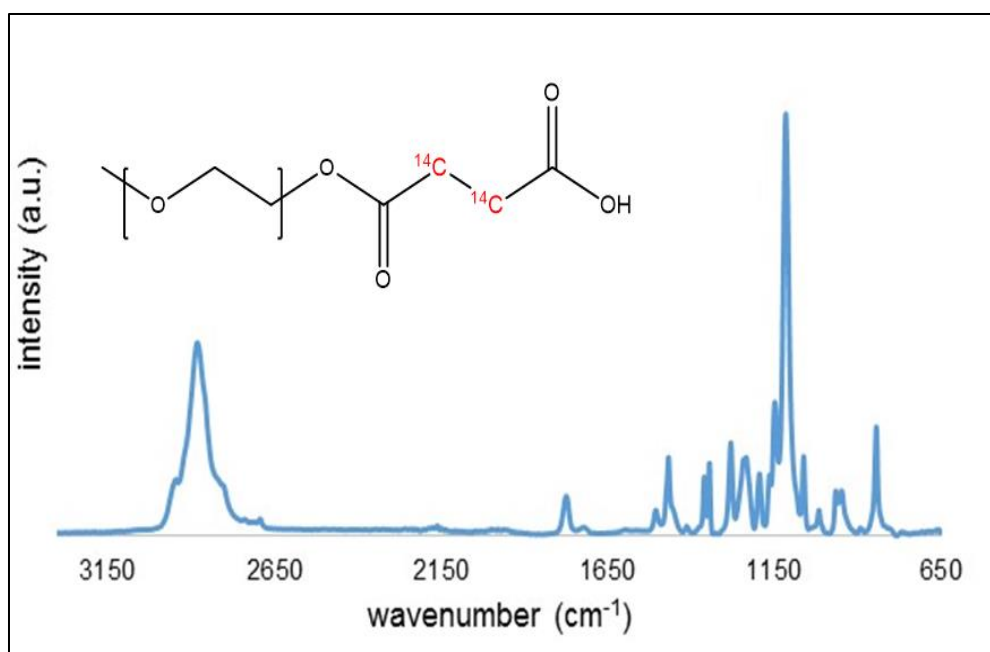


Figure A4. FTIR of PEG-succinic acid.

After completing the attachment of doxorubicin for both the radiolabeled and unlabeled carboxylic acid functionalized PEG, and the subsequent combination of the two components, additional FTIR was completed. It had a very similar spectrum as the one previously conducted for the carboxylic acid modified PEG, with an additional peak indicating the presence of aromatic alkene groups. This is shown in Figure A5 below. The relevant peaks for verification of the presence of doxorubicin and the polymer backbone are depicted at 1114 cm^{-1} , 1774 cm^{-1} , and in the range of $1490\text{-}1526\text{ cm}^{-1}$.

Once again the peak near 1114 cm^{-1} is representative of the ether linkage of the polymer backbone, while the 1722 cm^{-1} peak represents the carbonyl pendant group along the backbone. Finally, the new peak in the range of $1490\text{-}1526\text{ cm}^{-1}$ shows the presence of the aromatic rings in doxorubicin as it indicates an aromatic alkene group. These FTIR results provided verification that the drug-conjugate was synthesized, without providing any information regarding the activity or concentration of doxorubicin present in the system. Further analysis through LSC and UV-VIS were required to gain this information.

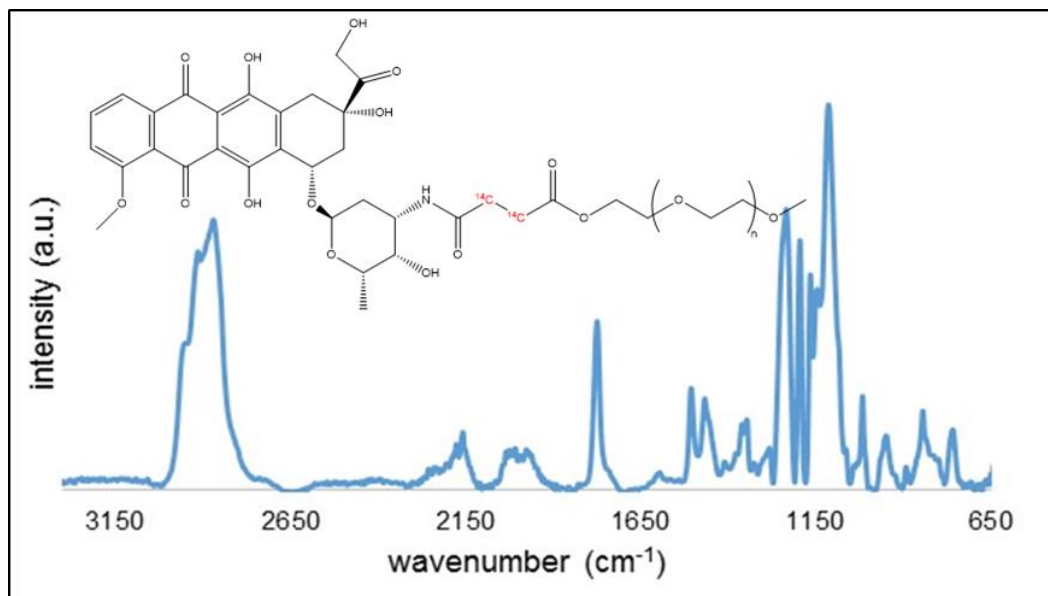


Figure A5. FTIR of the final polymer-drug conjugate (unlabeled and labeled combined).

LSC was utilized to provide information regarding the activity of the final radiolabeled polymer-drug conjugate, prior to combination with the unlabeled radiolabeled polymer drug conjugate. This was viewed through a graphical representation of energy in kiloelectronvolts vs. counts, as shown in Figure A6. This provides qualitative

information capable of identifying the radionuclide used. However, quantitative information, in the form of counts per minute, was used to determine the activity of the sample. This was done by utilizing the fact that the decays per minute can be calculated through a relation between the counts per minute of the sample, the counts per minute of the background, and the counting efficiency, as shown by the following equation:

$$\text{Eq. A1) } dpm = \frac{cpm \text{ sample} - cpm \text{ background}}{\text{counting efficiency}}$$

where dpm is decays per minute, cpm is counts per minute and counting efficiency of ^{14}C is determined by counting a ^{14}C standard.

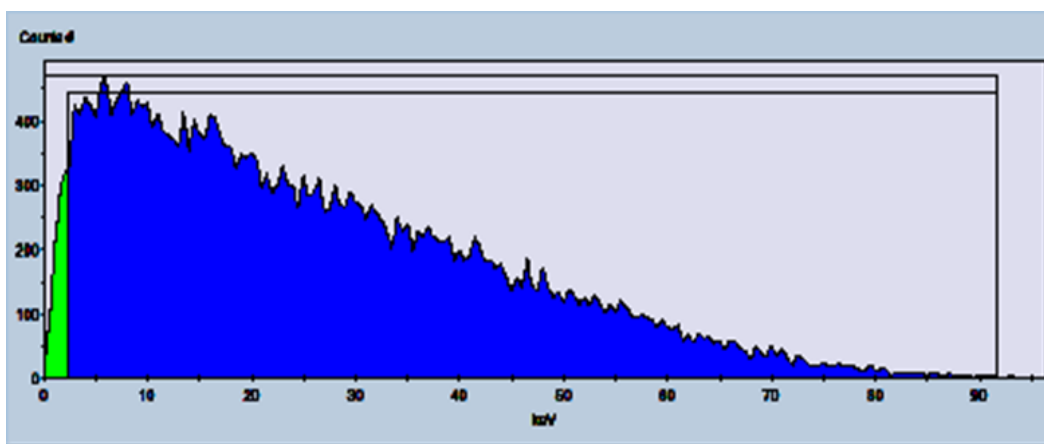


Figure A6. LSC spectrum of final polymer-drug conjugate.

In this instance, the counts per minute of the sample was 1065, while the background sample was 17 counts per minute, and the count efficiency was 0.931. The decays per minute of the sample is about 1125, which can be divided by the volume of the LSC sample (0.03 ml) to obtain 37,522 dpm/ml. This number can be multiplied by the total volume of polymer solution (19.4 ml) to obtain a total dpm of 727,934. Finally, this can

then be converted into nanoCuries (nCi) of sample activity based around the fact that 1 nanoCurie is equivalent to 2200 decays per minute. Utilizing this conversion shows that the sample of the polymer was roughly 330 nCi in activity. Some of the initial activity was lost during the transfer of the product from the dialysis tubing after the first and second modification steps for the radiolabeled synthesis. Regardless of this loss, the 330 nCi activity still provided flexibility when combining the labeled and unlabeled components of the polymer-drug conjugate, as the goal was a specific activity of 200 nCi/mg of dox-equivalent. By combining the labeled and unlabeled polymer-drug conjugate according to the concentration of doxorubicin, it was possible to roughly create this desired specific activity of the polymer-drug conjugate.

UV-Vis was used to determine the concentration of doxorubicin in the final product. A series of standards for doxorubicin was created over varying concentrations to create a calibration curve. The concentration values utilized to calculate this were as follows: 0.04998 mg/ml, 0.009966 mg/ml, 0.004994 mg/ml, and 0.000994 mg/ml. The absorbance value for the corresponding wavelength of doxorubicin, 483 nm, was recorded for each of these concentrations and then plotted to create said calibration curve. The PEGylated samples were measured and the absorbance values at 483 nm were

compared to the calibration curve to determine the concentrations of the samples. This is shown in Figures A7 and A8.

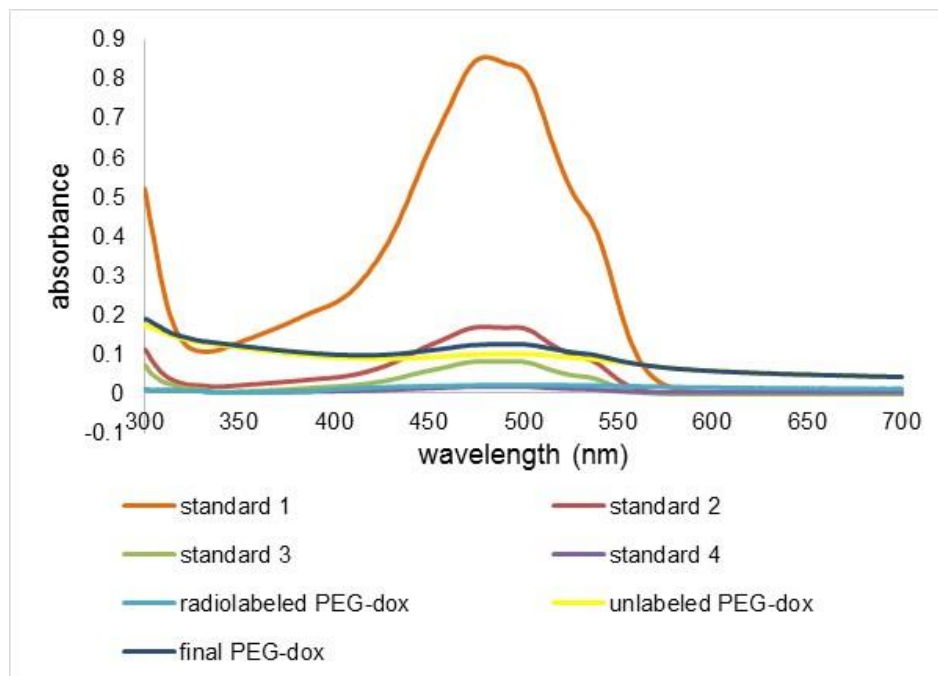


Figure A7. UV-Vis spectra of standards and PEGylated doxorubicin samples.

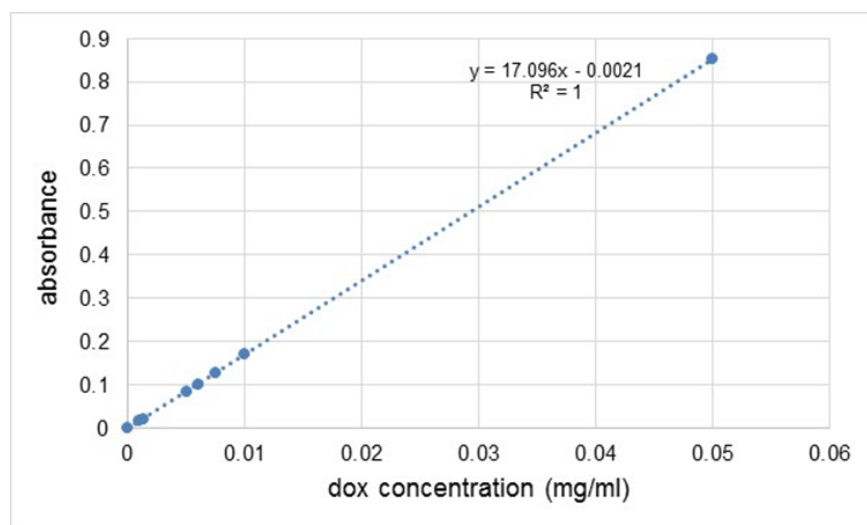


Figure A8. UV-Vis calibration curve.

To achieve a specific activity of 200nCi/mg of dox equivalent, roughly 100 nCi of the radiolabeled polymer was used. The specific activity of the succinic anhydride is 5000 μ Ci/mmol. Using this specific activity, the activity of the polymer, and the molecular weight of doxorubicin it was determined that 100 nCi of the radiolabeled polymer-drug conjugate should contain approximately 0.0108 mg of doxorubicin. This value agrees closely with the total concentration determined by UV-Vis. To reach the desired specific activity, approximately 0.48 mg of unlabeled polymer-drug conjugate was added. The final specific activity of the sample was 204 nCi/mg of dox-equivalent.

Conclusions

This study was designed to create a novel tracking system for biodistribution studies. This consisted of a polymer-drug conjugate which provided qualitative and quantitative data regarding its location in the body and where it concentrates. Furthermore, the accuracy was ensured using a two-part tracking system, as doxorubicin's fluorescent characteristics enable UV-Vis analysis, while the radiolabeled polymer can be tracked through LSC analysis.

In order to create such a polymer-drug conjugate, a multiple step synthesis procedure was followed, for both radiolabeled and unlabeled components. First PEG-methyl ether was modified with labeled or unlabeled succinic anhydride to create a carboxylic acid functionalized group. This carboxylic acid group was capable of reacting with doxorubicin through EDC chemistry to create the desired polymer-drug conjugate. The labeled and unlabeled components were the combined in specific ratios relative to one

another to create a final product with an activity of roughly 200 nCi. During this procedure, several methods of analysis were completed to ensure that the synthesis was proceeding appropriately.

FTIR was utilized to ensure that the desired reactions had occurred by analyzing the observed peaks for the presence of specific functional groups. After verifying that the reactions proceeded appropriately for both the labeled and unlabeled reactions, LSC was completed to determine the activity of the individual labeled polymer-doxorubicin component. This was necessary for the later combination with the unlabeled polymer-doxorubicin component. UV-Vis served as another method of ensuring that doxorubicin was present, as its fluorescence was observed at 483 nm. Furthermore, by creating a calibration curve, the concentration of both the labeled and unlabeled components could be determined. This information enabled the combination of the two systems in specific ratios to create a final polymer-drug conjugate of roughly the desired activity.

Ultimately, this study verified that the synthesis of a potential two-part tracking system was possible through the combination of a radiolabeled polymer-backbone and a fluorescent-active drug conjugate. It further showed the viability of FTIR as a means of ensuring occurrence of reaction, LSC to determine the activity of such a system, and UV-Vis to determine the concentration of doxorubicin in the polymer drug conjugate. This

system is nearly ready for use in a biodistribution study to confirm efficacy of drug delivery and utility of this method for detection of distribution.

References

1. Na, H.; Song, I.; Hyeon, T., Inorganic Nanoparticles for MRI Contrast Agents. *Advanced Materials* **2009**, *21* (21), 2133-2148.
2. Shokrollahi, H., Contrast agents for MRI. *Materials Science and Engineering C- Materials for Biological Applications* **2013**, *33* (8), 4485-4497.
3. Creixell, M.; Bohorquez, A.; Torres-Lugo, M.; Rinaldi, C., EGFR-targeted magnetic nanoparticle heaters kill cancer cells without a perceptible temperature rise. *ACS Nano* **2011**, *5* (9), 7124-7129.
4. Stone, R.; Willi, T.; Rosen, Y.; Mefford, O. T.; Alexis, F., Targeted magnetic hyperthermia. *Therapeutic Delivery* **2011**, *2* (6), 815-838.
5. Alexiou, C.; Jurgons, R.; Schmid, R.; Bergemann, C.; Henke, J.; Erhardt, W.; Huenges, E.; Parak, F., Magnetic drug targeting - Biodistribution of the magnetic carrier and the chemotherapeutic agent mitoxantrone after locoregional cancer treatment. *Journal of Drug Targeting* **2003**, *11* (3), 139-149.
6. Wang, A.; Bagalkot, V.; Vasilliou, C.; F., G.; Alexis, F.; Zhang, L.; Shaikh, M.; Yuet, K.; Cima, M.; Langer, R.; Kantoff, P.; Bander, N.; Jon, S.; Farokhzad, O., Superparamagnetic iron oxide nanoparticle-aptamer bioconjugates for combined prostate cancer imaging and therapy. *Chemmedchem* **2008**, *3* (9), 1311-1315.
7. Larimi, Y.; Mallah, M.; Moosavian, M.; Safdari, J., Fabrication of a magmolecule using nanoparticle and evaluation of its adsorption capacity for selenium ions from nuclear wastewater. *Journal of Radioanalytical and Nuclear Chemistry* **2013**, *298* (3), 1511-1518.
8. Kilianova, M.; Pucek, R.; Filip, J.; Kolarik, J.; Kvitek, L.; Panacek, A.; Tucek, J.; Zboril, R., Remarkable efficiency of ultrafine superparamagnetic iron(III) oxide nanoparticles toward arsenate removal from aqueous environment. *Chemosphere* **2013**, *93* (11), 2690-2697.
9. Wu, W.; He, Q. G.; Jiang, C. Z., Magnetic Iron Oxide Nanoparticles: Synthesis and Surface Functionalization Strategies. *Nanoscale Research Letters* **2008**, *3* (11), 397-415.
10. Yu, W. W.; Falkner, J. C.; Yavuz, C. T.; Colvin, V. L., Synthesis of monodisperse iron oxide nanocrystals by thermal decomposition of iron carboxylate salts. *Chemical Communications* **2004**, (20), 2306-2307.
11. Boal, A. K.; Das, K.; Gray, M.; Rotello, V. M., Monolayer exchange chemistry of gamma-Fe₂O₃ nanoparticles. *Chemistry of Materials* **2002**, *14* (6), 2628-2636.
12. Hofmann, A.; Thierbach, S.; Semisch, A.; Hartwig, A.; Taupitz, M.; Ruehl, E.; Graf, C., Highly monodisperse water-dispersible iron oxide nanoparticles for biomedical applications. *Journal of Materials Chemistry* **2010**, *20* (36), 7842-7853.
13. Lattuada, M.; Hatton, T. A., Functionalization of monodisperse magnetic nanoparticles. *Langmuir* **2007**, *23*, 2158-2168.

14. Bloemen, M.; Brullot, W.; Tai Thien, L.; Geukens, N.; Gils, A.; Verbiest, T., Improved functionalization of oleic acid-coated iron oxide nanoparticles for biomedical applications. *Journal of Nanoparticle Research* **2012**, *14* (9).
15. Davis, K.; Witmer, M.; Qi, B.; Powell, B. A.; Kitchens, C. L.; Mefford, O. T., Quantitative measurement of ligand exchange on iron oxides via radiolabeled oleic acid. *Langmuir* **2014**, *30*, 10918-10925.
16. Azevedo, R. B.; Alves Valois, C. R.; Chaves, S. B.; Silva, J. R.; Garcia, M. P., Leukocyte transepithelial migration in lung induced by DMSA functionalized magnetic nanoparticles. *Cell Adhesion & Migration* **2011**, *5* (1), 29-33.
17. Barrera, C.; Herrera, A. P.; Bezares, N.; Fachini, E.; Olayo-Valles, R.; Hinestroza, J. P.; Rinaldi, C., Effect of poly(ethylene oxide)-silane graft molecular weight on the colloidal properties of iron oxide nanoparticles for biomedical applications. *Journal of Colloid and Interface Science* **2012**, *377*, 40-50.
18. Miles, W. C.; Huffstetler, P. P.; Goff, J. D.; Chen, A. Y.; Riffle, J. S.; Davis, R. M., Design of Stable Polyether-Magnetite Complexes in Aqueous Media: Effects of the Anchor Group, Molecular Weight, and Chain Density. *Langmuir* **2011**, *27* (9), 5456-5463.
19. Guo, R.; Song, Y.; Wang, G. L.; Murray, R. W., Does core size matter in the kinetics of ligand exchanges of monolayer-protected Au clusters? *Journal of the American Chemical Society* **2005**, *127* (8), 2752-2757.
20. Murray, R. W., Nanoelectrochemistry: Metal nanoparticles, nanoelectrodes, and nanopores. *Chemical Reviews* **2008**, *108* (7), 2688-2720.
21. Hostetler, M. J.; Wingate, J. E.; Zhong, C. J.; Harris, J. E.; Vachet, R. W.; Clark, M. R.; Londono, J. D.; Green, S. J.; Stokes, J. J.; Wignall, G. D.; Glish, G. L.; Porter, M. D.; Evans, N. D.; Murray, R. W., Alkanethiolate gold cluster molecules with core diameters from 1.5 to 5.2 nm: Core and monolayer properties as a function of core size. *Langmuir* **1998**, *14* (1), 17-30.
22. Huhn, J.; Carrillo-Carrion, C.; Soliman, M. G.; Pfeiffer, C.; Valdeperez, D.; Masood, A.; Chakraborty, I.; Zhu, L.; Gallego, M.; Yue, Z.; Carril, M.; Feliu, N.; Escudero, A.; Alkilany, A. M.; Pelaz, B.; del Pino, P.; Parak, W. J., Selected Standard Protocols for the Synthesis, Phase Transfer, and Characterization of Inorganic Colloidal Nanoparticles. *Chemistry of Materials* **2017**, *29* (1), 399-461.
23. Cano, M.; Nunez-Lozano, R.; Lumberras, R.; Gonzalez-Rodriguez, V.; Delgado-Garcia, A.; Jimenez-Hoyuela, J. M.; de la Cueva-Mendez, G., Partial PEGylation of superparamagnetic iron oxide nanoparticles thinly coated with amine-silane as a source of ultrastable tunable nanosystems for biomedical applications. *Nanoscale* **2017**, *9* (2), 812-822.
24. Korpany, K. V.; Majewski, D. D.; Chiu, C. T.; Cross, S. N.; Blum, A. S., Iron Oxide Surface Chemistry: Effect of Chemical Structure on Binding in Benzoic Acid and Catechol Derivatives. *Langmuir* **2017**, *33* (12), 3000-3013.
25. Penke, Y. K.; Anantharaman, G.; Ramkumar, J.; Kar, K. K., Aluminum Substituted Cobalt Ferrite (Co-Al-Fe) Nano Adsorbent for Arsenic Adsorption in Aqueous Systems and Detailed Redox Behavior Study with XPS. *Acs Applied Materials & Interfaces* **2017**, *9* (13), 11587-11598.

26. Walter, A.; Garofalo, A.; Bonazza, P.; Meyer, F.; Martinez, H.; Fleutot, S.; Billotey, C.; Taleb, J.; Felder-Flesch, D.; Begin-Colin, S., Effect of the Functionalization Process on the Colloidal, Magnetic Resonance Imaging, and Bioelimination Properties of Mono- or Bisphosphonate-Anchored Dendronized Iron Oxide Nanoparticles. *Chempluschem* **2017**, 82 (4), 647-659.
27. Xiao, D. L.; Lu, T.; Zeng, R.; Bi, Y. P., Preparation and highlighted applications of magnetic microparticles and nanoparticles: a review on recent advances. *Microchimica Acta* **2016**, 183 (10), 2655-2675.
28. Sharifi, I.; Shokrollahi, H.; Amiri, S., Ferrite-based magnetic nanofluids used in hyperthermia applications. *Journal of Magnetism and Magnetic Materials* **2012**, 324 (6), 903-915.
29. Laurent, S.; Forge, D.; Port, M.; Roch, A.; Robic, C.; Elst, L. V.; Muller, R. N., Magnetic iron oxide nanoparticles: Synthesis, stabilization, vectorization, physicochemical characterizations, and biological applications. *Chemical Reviews* **2008**, 108 (6), 2064-2110.
30. Jolivet, J. P.; Chaneac, C.; Tronc, E., Iron oxide chemistry. From molecular clusters to extended solid networks. *Chemical Communications* **2004**, (5), 481-487.
31. Massart, R., PREPARATION OF AQUEOUS MAGNETIC LIQUIDS IN ALKALINE AND ACIDIC MEDIA. *Ieee Transactions on Magnetics* **1981**, 17 (2), 1247-1248.
32. Braz, S. V.; Monge-Fuentes, V.; da Silva, J. R.; Tomaz, C.; Tavares, M. C.; Garcia, M. P.; Bao, S. N.; Lozzi, S. P.; de Azevedo, R. B., Morphological Analysis of Reticuloendothelial System in Capuchin Monkeys (*Sapajus* spp.) after Meso-2,3-Dimercaptosuccinic Acid (DMSA) Coated Magnetic Nanoparticles Administration. *Plos One* **2015**, 10 (11).
33. Fauconnier, N.; Pons, J. N.; Roger, J.; Bee, A., Thiolation of maghemite nanoparticles by dimercaptosuccinic acid. *Journal of Colloid and Interface Science* **1997**, 194, 427-433.
34. Bee, A.; Massart, R.; Neveu, S., SYNTHESIS OF VERY FINE MAGHEMITE PARTICLES. *Journal of Magnetism and Magnetic Materials* **1995**, 149 (1-2), 6-9.
35. Butt, F. A.; Jafri, S. M. M., Effect of nucleating agents and stabilisers on the synthesis of Iron-Oxide Nanoparticles-XRD analysis. *Advances in Nano Research* **2015**, 3 (3), 169-176.
36. Salunkhe, A. B.; Khot, V. M.; Ruso, J. M.; Patil, S. I., Water dispersible superparamagnetic Cobalt iron oxide nanoparticles for magnetic fluid hyperthermia. *Journal of Magnetism and Magnetic Materials* **2016**, 419, 533-542.
37. Markiewicz, K. H.; Seiler, L.; Misztalewska, I.; Winkler, K.; Harrisson, S.; Wilczewska, A. Z.; Destarac, M.; Marty, J. D., Advantages of poly(vinyl phosphonic acid)-based double hydrophilic block copolymers for the stabilization of iron oxide nanoparticles. *Polymer Chemistry* **2016**, 7 (41), 6391-6399.
38. Singh, M.; Sviridenkova, N.; Timur, N.; Savchenko, A.; Shetinin, I.; Majouga, A., Synthesis and Characterization of Stable Iron Oxide Nanoparticle with Amino Covalent Binding on the Surface for Biomedical Application. *Journal of Cluster Science* **2016**, 27 (4), 1383-1393.

39. Ma, M.; Zhang, Y.; Yu, W.; Shen, H. Y.; Zhang, H. Q.; Gu, N., Preparation and characterization of magnetite nanoparticles coated by amino silane. *Colloids and Surfaces a-Physicochemical and Engineering Aspects* **2003**, *212* (2-3), 219-226.
40. Kim, D. K.; Zhang, Y.; Voit, W.; Rao, K. V.; Muhammed, M., Synthesis and characterization of surfactant-coated superparamagnetic monodispersed iron oxide nanoparticles. *Journal of Magnetism and Magnetic Materials* **2001**, *225* (1-2), 30-36.
41. Hyeon, T.; Lee, S. S.; Park, J.; Chung, Y.; Bin Na, H., Synthesis of highly crystalline and monodisperse maghemite nanocrystallites without a size-selection process. *Journal of the American Chemical Society* **2001**, *123* (51), 12798-12801.
42. Sun, S. H.; Zeng, H., Size-controlled synthesis of magnetite nanoparticles. *Journal of the American Chemical Society* **2002**, *124* (28), 8204-8205.
43. Park, J.; An, K. J.; Hwang, Y. S.; Park, J. G.; Noh, H. J.; Kim, J. Y.; Park, J. H.; Hwang, N. M.; Hyeon, T., Ultra-large-scale syntheses of monodisperse nanocrystals. *Nature Materials* **2004**, *3* (12), 891-895.
44. Vreeland, E. C.; Watt, J.; Schober, G. B.; Hance, B. G.; Austin, M. J.; Price, A. D.; Fellows, B. D.; Monson, T. C.; Hudak, N. S.; Maldonado-Camargo, L.; Bohorquez, A. C.; Rinaldi, C.; Huber, D. L., Enhanced nanoparticle size control by extending LaMer's mechanism. *Chemistry of Materials* **2014**, *27* (17), 6059-6066.
45. Chen, D.; Xu, R., Hydrothermal synthesis and characterization of nanocrystalline Fe₃O₄ powders. *Materials Research Bulletin* **1998**, *33* (7), 1015-1021.
46. Xu, Z. C.; Shen, C. M.; Hou, Y. L.; Gao, H. J.; Sun, S. S., Oleylamine as Both Reducing Agent and Stabilizer in a Facile Synthesis of Magnetite Nanoparticles. *Chemistry of Materials* **2009**, *21* (9), 1778-1780.
47. Takami, S.; Sato, T.; Mousavand, T.; Ohara, S.; Umetsu, M.; Adschiri, T., Hydrothermal synthesis of surface-modified iron oxide nanoparticles. *Materials Letters* **2007**, *61* (26), 4769-4772.
48. Bersani, D.; Lottici, P. P.; Montenero, A., Micro-Raman investigation of iron oxide films and powders produced by sol-gel syntheses. *Journal of Raman Spectroscopy* **1999**, *30* (5), 355-360.
49. Cui, H. T.; Liu, Y.; Ren, W. Z., Structure switch between alpha-Fe₂O₃, gamma-Fe₂O₃ and Fe₃O₄ during the large scale and low temperature sol-gel synthesis of nearly monodispersed iron oxide nanoparticles. *Advanced Powder Technology* **2013**, *24* (1), 93-97.
50. Moghaddam, F. M.; Ayati, S. E.; Firouzi, H. R.; Ghorbani, F., Immobilization of copper ions onto alpha-amidotriazole-functionalized magnetic nanoparticles and their application in the synthesis of triazole derivatives in water. *Applied Organometallic Chemistry* **2016**, *30* (6), 488-493.
51. Oz, Y.; Arslan, M.; Gevrek, T. N.; Sanyal, R.; Sanyal, A., Modular Fabrication of Polymer Brush Coated Magnetic Nanoparticles: Engineering the Interface for Targeted Cellular Imaging. *Acs Applied Materials & Interfaces* **2016**, *8* (30), 19813-19826.
52. Toulemon, D.; Pichon, B. P.; Leuvre, C.; Zafeiratos, S.; Papaefthimiou, V.; Cattoen, X.; Begin-Colin, S., Fast Assembling of Magnetic Iron Oxide Nanoparticles by Microwave-Assisted Copper(I) Catalyzed Alkyne-Azide Cycloaddition (CuAAC). *Chemistry of Materials* **2013**, *25* (14), 2849-2854.

53. Choi, D.; Son, B.; Park, T. H.; Hong, J., Controlled surface functionality of magnetic nanoparticles by layer-by-layer assembled nano-films. *Nanoscale* **2015**, *7* (15), 6703-6711.
54. Wang, M.; Hou, X. C.; Wiraja, C.; Sun, L. B.; Xu, Z. J.; Xu, C. J., Smart Magnetic Nanosensors Synthesized through Layer-by-Layer Deposition of Molecular Beacons for Noninvasive and Longitudinal Monitoring of Cellular mRNA. *Acs Applied Materials & Interfaces* **2016**, *8* (9), 5877-5886.
55. Eyiler, E.; Walters, K. B., Magnetic iron oxide nanoparticles grafted with poly(itaconic acid)-block-poly(N-isopropylacrylamide). *Colloids and Surfaces a-Physicochemical and Engineering Aspects* **2014**, *444*, 321-325.
56. Zhou, Y.; Wang, S. X.; Ding, B. J.; Yang, Z. M., Modification of magnetite nanoparticles via surface-initiated atom transfer radical polymerization (ATRP). *Chemical Engineering Journal* **2008**, *138* (1-3), 578-585.
57. Ourry, L.; Toulemon, D.; Ammar, S.; Mammeri, F., Methods for preparing polymer-decorated single exchange-biased magnetic nanoparticles for application in flexible polymer-based films. *Beilstein Journal of Nanotechnology* **2017**, *8*, 408-417.
58. Xie, Y. H.; Sougrat, R.; Nunes, S. P., Synthesis and Characterization of Polystyrene Coated Iron Oxide Nanoparticles and Asymmetric Assemblies by Phase Inversion. *Journal of Applied Polymer Science* **2015**, *132* (5).
59. Dutta, S.; Parida, S.; Maiti, C.; Banerjee, R.; Mandal, M.; Dhara, D., Polymer grafted magnetic nanoparticles for delivery of anticancer drug at lower pH and elevated temperature. *Journal of Colloid and Interface Science* **2016**, *467*, 70-80.
60. Prai-In, Y.; Boonthip, C.; Rutnakornpituk, B.; Wichai, U.; Montembault, V.; Pascual, S.; Fontaine, L.; Rutnakornpituk, M., Recyclable magnetic nanocluster crosslinked with poly(ethylene oxide)-block-poly(2-vinyl-4,4-dimethylazlactone) copolymer for adsorption with antibody. *Materials Science & Engineering C-Materials for Biological Applications* **2016**, *67*, 285-293.
61. Shao, C.; Li, X. M.; Pei, Z. C.; Liu, D. D.; Wang, L.; Dong, H.; Pei, Y. X., Facile fabrication of glycopolymer-based iron oxide nanoparticles and their applications in the carbohydrate-lectin interaction and targeted cell imaging. *Polymer Chemistry* **2016**, *7* (6), 1337-1344.
62. Decher, G., Fuzzy nanoassemblies: Toward layered polymeric multicomposites. *Science* **1997**, *277* (5330), 1232-1237.
63. Caruso, F.; Susha, A. S.; Giersig, M.; Mohwald, H., Magnetic core-shell particles: Preparation of magnetite multilayers on polymer latex microspheres. *Advanced Materials* **1999**, *11* (11), 950-+.
64. Carageorghopol, A.; Chechik, V., Mechanistic aspects of ligand exchange in Au nanoparticles. *Physical Chemistry Chemical Physics* **2008**, *10* (33), 5029-5041.
65. Palma, S. I. C. J.; Marciello, M.; Carvalho, A.; Veintemillas-Verdaguer, S.; del Puerto Morales, M.; Roque, A. C. A., Effects of phase transfer ligands on monodisperse iron oxide magnetic nanoparticles. *Journal of Colloid and Interface Science* **2015**, *437*, 147-155.

66. Herrera, A. P.; Barrera, C.; Zayas, Y.; Rinaldi, C., Monitoring colloidal stability of polymer-coated magnetic nanoparticles using AC susceptibility measurements. *Journal of Colloid and Interface Science* **2010**, *342* (2), 540-549.
67. Wyss, P. P.; Lamichhane, S.; Rauber, M.; Thomann, R.; Kraemer, K. W.; Shastri, V. P., Tripod USPIOs with high aspect ratio show enhanced T2 relaxation and cytocompatibility. *Nanomedicine* **2016**, *11* (9), 1017-1030.
68. Park, Y. C.; Paulsen, J.; Nap, R. J.; Whitaker, R. D.; Mathiyazhagan, V.; Song, Y.-Q.; Huerlimann, M.; Szeleifer, I.; Wong, J. Y., Adsorption of Superparamagnetic Iron Oxide Nanoparticles on Silica and Calcium Carbonate Sand. *Langmuir* **2014**, *30* (3), 784-792.
69. Ruiz, A.; Salas, G.; Calero, M.; Hernandez, Y.; Villanueva, A.; Herranz, F.; Veintemillas-Verdaguer, S.; Martinez, E.; Barber, D. F.; Morales, M. P., Short-chain PEG molecules strongly bound to magnetic nanoparticle for MRI long circulating agents. *Acta Biomaterialia* **2013**, *9* (5), 6421-6430.
70. Ruiz, A.; Hernandez, Y.; Cabal, C.; Gonzalez, E.; Veintemillas-Verdaguer, S.; Martinez, E.; Morales, M. P., Biodistribution and pharmacokinetics of uniform magnetite nanoparticles chemically modified with polyethylene glycol. *Nanoscale* **2013**, *5* (23), 11400-11408.
71. Sanaeifar, N.; Rabiee, M.; Abdolrahim, M.; Tahriri, M.; Vashae, D.; Tayebi, L., A novel electrochemical biosensor based on Fe₃O₄ nanoparticles-polyvinyl alcohol composite for sensitive detection of glucose. *Analytical Biochemistry* **2017**, *519*, 19-26.
72. Oanh, V. T. K.; Lam, T. D.; Thu, V. T.; Lu, L. T.; Nam, P. H.; Tam, L. T.; Manh, D. H.; Phuc, N. X., A Novel Route for Preparing Highly Stable Fe₃O₄ Fluid with Poly(Acrylic Acid) as Phase Transfer Ligand. *Journal of Electronic Materials* **2016**, *45* (8), 4010-4017.
73. Gogoi, M.; Deb, P.; Vasani, G.; Keil, P.; Kostka, A.; Erbe, A., Direct monophasic replacement of fatty acid by DMSA on SPION surface. *Applied Surface Science* **2012**, *258* (24), 9685-9691.
74. Zhang, L.; Wang, X.; Zou, J.; Liu, Y.; Wang, J., DMSA-Coated Iron Oxide Nanoparticles Greatly Affect the Expression of Genes Coding Cysteine-Rich Proteins by Their DMSA Coating. *Chemical Research in Toxicology* **2015**, *28* (10), 1961-1974.
75. Pang, Y. L.; Lim, S.; Ong, H. C.; Chong, W. T., Research progress on iron oxide-based magnetic materials: Synthesis techniques and photocatalytic applications. *Ceramics International* **2016**, *42* (1), 9-34.
76. Caliceti, P.; Veronese, F. M., Pharmacokinetic and biodistribution properties of poly(ethylene glycol)-protein conjugates. *Advanced Drug Delivery Reviews* **2003**, *55* (10), 1261-1277.
77. Li, W. J.; Zhan, P.; De Clercq, E.; Lou, H. X.; Liu, X. Y., Current drug research on PEGylation with small molecular agents. *Progress in Polymer Science* **2013**, *38* (3-4), 421-444.
78. Hong, H. J.; Jeong, H. S.; Kim, B. G.; Hong, J.; Park, I. S.; Ryu, T.; Chung, K. S.; Kim, H.; Ryu, J., Highly stable and magnetically separable alginate/Fe₃O₄ composite for the removal of strontium (Sr) from seawater. *Chemosphere* **2016**, *165*, 231-238.

79. Chi, F. H.; Amy, G. L., Kinetic study on the sorption of dissolved natural organic matter onto different aquifer materials: the effects of hydrophobicity and functional groups. *Journal of Colloid and Interface Science* **2004**, *274* (2), 380-391.
80. Dhoble, R. M.; Lunge, S.; Bhole, A. G.; Rayalu, S., Magnetic binary oxide particles (MBOP): A promising adsorbent for removal of As (III) in water. *Water Research* **2011**, *45* (16), 4769-4781.
81. Stephen, Z. R.; Gebhart, R. N.; Jeon, M.; Blair, A. A.; Ellenbogen, R. G.; Silber, J. R.; Zhang, M. Q., pH-Sensitive O6-Benzylguanosine Polymer Modified Magnetic Nanoparticles for Treatment of Glioblastomas. *Bioconjugate Chemistry* **2017**, *28* (1), 194-202.
82. Verwey, E. J. W., THEORY OF THE STABILITY OF LYOPHOBIC COLLOIDS. *Journal of Physical and Colloid Chemistry* **1947**, *51* (3), 631-636.
83. Mefford, O. T.; Vadala, M. L.; Goff, J. D.; Carroll, M. R. J.; Mejia-Ariza, R.; Caba, B. L.; St Pierre, T. G.; Woodward, R. C.; Davis, R. M.; Riffle, J. S., Stability of polydimethylsiloxane-magnetite nanoparticle dispersions against flocculation: Interparticle interactions of polydisperse materials. *Langmuir* **2008**, *24* (9), 5060-5069.
84. Napper, D. H., FLOCCULATION STUDIES OF STERICALLY STABILIZED DISPERSIONS. *Journal of Colloid and Interface Science* **1970**, *32* (1), 106-&.
85. Napper, D. H.; Netschey, A., STUDIES OF STERIC STABILIZATION OF COLLOIDAL PARTICLES. *Journal of Colloid and Interface Science* **1971**, *37* (3), 528-&.
86. Napper, D. H., STERIC STABILIZATION. *Journal of Colloid and Interface Science* **1977**, *58* (2), 390-407.
87. Coral, D. F.; Mendoza Zelis, P.; Marciello, M.; del Puerto Morales, M.; Craievich, A.; Sanchez, F. H.; Fernandez van Raap, M. B., Effect of Nanoclustering and Dipolar Interactions in Heat Generation for Magnetic Hyperthermia. *Langmuir* **2016**, *32* (5), 1201-1213.
88. de Montferrand, C.; Hu, L.; Lalatonne, Y.; Lievre, N.; Bonnin, D.; Brioude, A.; Motte, L., SiO₂ versus chelating agent@ iron oxide nanoparticles: interactions effect in nanoparticles assemblies at low magnetic field. *Journal of Sol-Gel Science and Technology* **2015**, *73* (3), 572-579.
89. Calero, M.; Gutierrez, L.; Salas, G.; Luengo, Y.; Lazaro, A.; Acedo, P.; Morales, M. P.; Miranda, R.; Villanueva, A., Efficient and safe internalization of magnetic iron oxide nanoparticles: Two fundamental requirements for biomedical applications. *Nanomedicine-Nanotechnology Biology and Medicine* **2014**, *10* (4), 733-743.
90. Mou, Y.; Zhou, J.; Xiong, F.; Li, H.; Sun, H.; Han, Y.; Gu, N.; Wang, C., Effects of 2,3-dimercaptosuccinic acid modified Fe₂O₃ nanoparticles on microstructure and biological activity of cardiomyocytes. *Rsc Advances* **2015**, *5* (25), 19493-19501.
91. Kuruva, P.; Matteppanavar, S.; Srinath, S.; Thomas, T., Size Control and Magnetic Property Trends in Cobalt Ferrite Nanoparticles Synthesized Using an Aqueous Chemical Route. *Ieee Transactions on Magnetics* **2014**, *50* (1).
92. de Montferrand, C.; Hu, L.; Milosevic, V.; Bonnin, D.; Motte, L.; Brioude, A.; Lalatonne, Y., Iron oxide nanoparticles with sizes, shapes and composition resulting in

- different magnetization signatures as potential labels for multiparametric detection. *Acta Biomaterialia* **2013**, *9* (4), 6150-6157.
93. Li, P. Z.; Chevallier, P.; Ramrup, P.; Biswas, D.; Vuckovich, D.; Fortin, M. A.; Oh, J. K., Mussel-Inspired Multidentate Block Copolymer to Stabilize Ultrasmall Superparamagnetic Fe₃O₄ for Magnetic Resonance Imaging Contrast Enhancement and Excellent Colloidal Stability. *Chemistry of Materials* **2015**, *27* (20), 7100-7109.
94. Sperling, R. A.; Parak, W. J., Surface modification, functionalization and bioconjugation of colloidal inorganic nanoparticles. *Therapeutic Innovation & Regulatory Science* **2013**, *47* (1), 1333-1383.
95. Gaponik, N.; Talapin, D. V.; Rogach, A. L.; Eychmuller, A.; Weller, H., Efficient phase transfer of luminescent thiol-capped nanocrystals: From water to nonpolar organic solvents. *Nano Letters* **2002**, *2* (8), 803-806.
96. Zhao, S. Y.; Chen, S. H.; Wang, S. Y.; Li, D. G.; Ma, H. Y., Preparation, phase transfer, and self-assembled monolayers of cubic Pt nanoparticles. *Langmuir* **2002**, *18* (8), 3315-3318.
97. Yang, J.; Deivaraj, T. C.; Too, H. P.; Lee, J. Y., An alternative phase-transfer method of preparing alkylamine-stabilized platinum nanoparticles. *Journal of Physical Chemistry B* **2004**, *108* (7), 2181-2185.
98. Calero, M.; Chiappi, M.; Lazaro-Carrillo, A.; Jose Rodriguez, M.; Javier Chichon, F.; Crosbie-Staunton, K.; Prina-Mello, A.; Volkov, Y.; Villanueva, A.; Carrascosa, J. L., Characterization of interaction of magnetic nanoparticles with breast cancer cells. *Journal of Nanobiotechnology* **2015**, *13*.
99. Goff, J. D.; Huffstetler, P. P.; Miles, W. C.; Pothayee, N.; Reinholz, C. M.; Ball, S.; Davis, R. M.; Riffle, J. S., Novel Phosphonate-Functional Poly(ethylene oxide)-Magnetite Nanoparticles Form Stable Colloidal Dispersions in Phosphate-Buffered Saline. *Chemistry of Materials* **2009**, *21* (20), 4784-4795.
100. Amstad, E.; Gillich, T.; Bilecka, I.; Textor, M.; Reimhult, E., Ultrastable Iron Oxide Nanoparticle Colloidal Suspensions Using Dispersants with Catechol-Derived Anchor Groups. *Nano Letters* **2009**, *9* (12), 4042-4048.
101. Saville, S. L.; Stone, R. C.; Qi, B.; Mefford, O. T., Investigation of the stability of magnetite nanoparticles functionalized with catechol based ligands in biological media. *Journal of Materials Chemistry* **2012**, *22* (47), 24909-24917.
102. Portet, D.; Denizot, B.; Rump, E.; Lejeune, J. J.; Jallet, P., Nonpolymeric coatings of iron oxide colloids for biological use as magnetic resonance imaging contrast agents. *Journal of Colloid and Interface Science* **2001**, *238* (1), 37-42.
103. Amstad, E.; Gehring, A. U.; Fischer, H.; Nagaiyanallur, V. V.; Hahner, G.; Textor, M.; Reimhult, E., Influence of electronegative substituents on the binding affinity of catechol-derived anchors to Fe₃O₄ nanoparticles. *Journal of Physical Chemistry* **2011**, *115*, 683-691.
104. Zhang, T. L.; Han, B. H., The Visualized Polarity-Sensitive Magnetic Nanoparticles. *Langmuir* **2010**, *26* (11), 8893-8900.
105. Chechik, V., Reduced reactivity of aged Au nanoparticles in ligand exchange reactions. *Journal of the American Chemical Society* **2004**, *126* (25), 7780-7781.

106. Soler, M. A. G.; Lima, E. C. D.; Nunes, E. S.; Silva, F. L. R.; Oliveira, A. C.; Azevedo, R. B.; Morais, P. C., Spectroscopic Study of Maghemite Nanoparticles Surface-Grafted with DMSA. *Journal of Physical Chemistry A* **2011**, *115* (6), 1003-1008.
107. Amstad, E.; Gehring, A. U.; Fischer, H.; Nagaiyanallur, V. V.; Hahner, G.; Textor, M.; Reimhult, E., Influence of Electronegative Substituents on the Binding Affinity of Catechol-Derived Anchors to Fe₃O₄ Nanoparticles. *Journal of Physical Chemistry C* **2011**, *115* (3), 683-691.
108. Montalti, M.; Prodi, L.; Zaccheroni, N.; Baxter, R.; Teobaldi, G.; Zerbetto, F., Kinetics of place-exchange reactions of thiols on gold nanoparticles. *Langmuir* **2003**, *19* (12), 5172-5174.
109. Hostetler, M. J.; Templeton, A. C.; Murray, R. W., Dynamics of place-exchange reactions on monolayer-protected gold cluster molecules. *Langmuir* **1999**, *15* (11), 3782-3789.
110. Song, Y.; Murray, R. W., Dynamics and extent of ligand exchange depend on electronic charge of metal nanoparticles. *Journal of the American Chemical Society* **2002**, *124* (24), 7096-7102.
111. Casey, W. H.; Swaddle, T. W., Why small? The use of small inorganic clusters to understand mineral surface and dissolution reactions in geochemistry. *Reviews of Geophysics* **2003**, *41* (2).
112. Swaddle, T. W., ACTIVATION PARAMETERS AND REACTION-MECHANISM IN OCTAHEDRAL SUBSTITUTION. *Coordination Chemistry Reviews* **1974**, *14* (3), 217-268.
113. Grant, M.; Jordan, R. B., KINETICS OF SOLVENT WATER EXCHANGE ON IRON(III). *Inorganic Chemistry* **1981**, *20* (1), 55-60.
114. Tofan-Lazar, J.; Al-Abadleh, H. A., Kinetic ATR-FTIR Studies on Phosphate Adsorption on Iron (Oxyhydr)oxides in the Absence and Presence of Surface Arsenic: Molecular-Level Insights into the Ligand Exchange Mechanism. *Journal of Physical Chemistry A* **2012**, *116* (41), 10143-10149.
115. Parikh, S. J.; Chorover, J., ATR-FTIR spectroscopy reveals bond formation during bacterial adhesion to iron oxide. *Langmuir* **2006**, *22* (20), 8492-8500.
116. De Palma, R.; Peeters, S.; Van Bael, M. J.; Van den Rul, H.; Bonroy, K.; Laureyn, W.; Mullens, J.; Borghs, G.; Maes, G., Silane ligand exchange to make hydrophobic superparamagnetic nanoparticles water-dispersible. *Chemistry of Materials* **2007**, *19* (7), 1821-1831.
117. Peak, D.; Ford, R. G.; Sparks, D. L., An in situ ATR-FTIR investigation of sulfate bonding mechanisms on goethite. *Journal of Colloid and Interface Science* **1999**, *218* (1), 289-299.
118. Gulley-Stahl, H.; Hogan, P. A., II; Schmidt, W. L.; Wall, S. J.; Buhrlage, A.; Bullen, H. A., Surface Complexation of Catechol to Metal Oxides: An ATR-FTIR, Adsorption, and Dissolution Study. *Environmental Science & Technology* **2010**, *44* (11), 4116-4121.
119. Guenin, E.; Lalatonne, Y.; Bolley, J.; Milosevic, I.; Platas-Iglesias, C.; Motte, L., Catechol versus bisphosphonate ligand exchange at the surface of iron oxide

- nanoparticles: towards multi-functionalization. *Journal of Nanoparticle Research* **2014**, *16* (11).
120. Maboudi, S. A.; Shojaosadati, S. A.; Arpanaei, A., Synthesis and characterization of multilayered nanobiohybrid magnetic particles for biomedical applications. *Materials & Design* **2017**, *115*, 317-324.
121. Muthukumaran, T.; Philip, J., Effect of phosphate and oleic acid capping on structure, magnetic properties and thermal stability of iron oxide nanoparticles. *Journal of Alloys and Compounds* **2016**, *689*, 959-968.
122. Durdureanu-Angheluta, A.; Dascalu, A.; Fifere, A.; Coroaba, A.; Pricop, L.; Chiriac, H.; Tura, v.; Pinteala, M.; Simionescu, B. C., Progress in the synthesis and characterization of magnetite nanoparticles with amino groups on the surface. *Journal of Magnetism and Magnetic Materials* **2012**, *324* (9), 1679-1689.
123. Lam, T.; Avti, P. K.; Pouliot, P.; Maafi, F.; Tardif, J. C.; Rheume, E.; Lesage, F.; Kakkar, A., Fabricating Water Dispersible Superparamagnetic Iron Oxide Nanoparticles for Biomedical Applications through Ligand Exchange and Direct Conjugation. *Nanomaterials* **2016**, *6* (6).
124. Qu, H. O.; Caruntu, D.; Liu, H. X.; O'Connor, C. J., Water-Dispersible Iron Oxide Magnetic Nanoparticles with Versatile Surface Functionalities. *Langmuir* **2011**, *27* (6), 2271-2278.
125. Zhu, K. C.; Duan, Y. Y.; Wang, F.; Gao, P.; Jia, H. Z.; Ma, C. Y.; Wang, C. Y., Silane-modified halloysite/Fe₃O₄ nanocomposites: Simultaneous removal of Cr(VI) and Sb(V) and positive effects of Cr(VI) on Sb(V) adsorption. *Chemical Engineering Journal* **2017**, *311*, 236-246.
126. Belachew, N.; Devi, D. R.; Basavaiah, K., Facile green synthesis of L-methionine capped magnetite nanoparticles for adsorption of pollutant Rhodamine B. *Journal of Molecular Liquids* **2016**, *224*, 713-720.
127. Huo, L. J.; Zeng, X. B.; Su, S. M.; Bai, L. Y.; Wang, Y. N., Enhanced removal of As (V) from aqueous solution using modified hydrous ferric oxide nanoparticles. *Scientific Reports* **2017**, *7*.
128. Muniz-Miranda, M.; Gellini, C.; Giorgetti, E.; Margheri, G., Bifunctional Fe₃O₄/Ag nanoparticles obtained by two-step laser ablation in pure water. *Journal of Colloid and Interface Science* **2017**, *489*, 100-105.
129. Tajabadi, M.; Khosroshahi, M. E.; Bonakdar, S., An efficient method of SPION synthesis coated with third generation PAMAM dendrimer. *Colloids and Surfaces a-Physicochemical and Engineering Aspects* **2013**, *431*, 18-26.
130. Xu, P. F.; Shen, Z. W.; Zhang, B. L.; Wang, J.; Wu, R. H., Synthesis and characterization of superparamagnetic iron oxide nanoparticles as calcium-responsive MRI contrast agents. *Applied Surface Science* **2016**, *389*, 560-566.
131. Larsen, E. K. U.; Nielsen, T.; Wittenborn, T.; Birkedal, H.; Vorup-Hensen, T.; Jakobsen, M. H.; Ostergaard, L.; Horsman, M. R.; Besenbacher, F.; Howard, K. A.; Kjems, J., Size-dependent accumulation of PEGylated silane-coated magnetic iron oxide nanoparticles in murine tumors. *ACS Nano* **2009**, *3* (7), 1947-1951.
132. Bailon, P.; Berthold, W., Polyethylene glycol-conjugated pharmaceutical proteins. *Pharmaceutical Science & Technology Today* **1998**, *1* (8), 352-356.

133. Nucci, M. L.; Shorr, R.; Abuchowski, A., THE THERAPEUTIC VALUE OF POLY(ETHYLENE GLYCOL)-MODIFIED PROTEINS. *Advanced Drug Delivery Reviews* **1991**, *6* (2), 133-151.
134. Kozlowski, A.; Harris, J. M., Improvements in protein PEGylation: pegylated interferons for treatment of hepatitis C. *Journal of Controlled Release* **2001**, *72* (1-3), 217-224.
135. Veronese, F. M.; Mero, A., The impact of PEGylation on biological therapies. *Biodrugs* **2008**, *22* (5), 315-329.
136. Birks, J. B., *The Theory and Practice of Scintillation Counting*. Pergamon Press: Long Island City, NY, 1964.
137. Horrocks, D. L., *Applications of Liquid Scintillation Counting*. Academic Press Inc.: New York, NY, 1975.
138. Stone, R. C.; Fellows, B. D.; Qi, B.; Trebatoski, D.; Jenkins, B.; Raval, Y.; Tzeng, T. R.; Bruce, T. F.; McNealy, T.; Austin, M. J.; Monson, T. C.; Huber, D. L.; Mefford, O. T., Highly stable multi-anchored magnetic nanoparticles for optical imaging within biofilms. *Journal of Colloid and Interface Science* **2015**, *459*, 175-182.
139. Shen, Y.; Gee, M. Y.; Tan, R.; Pellechia, P. J.; Greytak, A. B., Purification of Quantum Dots by Gel Permeation Chromatography and the Effect of Excess Ligands on Shell Growth and Ligand Exchange. *Chemistry of Materials* **2013**, *25* (14), 2838-2848.
140. De Jaeger, N.; Demeyer, H.; Finsy, R.; Sneyers, R.; Vanderdeelen, J.; van der Meer, P.; van Laethem, M., Particle Sizing by Photon Correlation Spectroscopy Part 1: Monodisperse Lattices- Influence of Scattering Angle and Concentration of Dispersed Material. *Particle and Particle Systems Characterization* **1991**, *8* (3), 179-186.
141. Saville, S. L.; Woodward, R. C.; House, M. J.; Tokarev, A.; Hammers, J.; Qi, B.; Shaw, J.; Saunders, M.; Varsani, R. R.; St Pierre, T. G.; Mefford, O. T., The effect of magnetically induced linear aggregates on proton transverse relaxation rates of aqueous suspensions of polymer coated magnetic nanoparticles. *Nanoscale* **2013**, *5* (5), 2152-2163.
142. Baaziz, W.; Pichon, B. P.; Fleutot, S.; Liu, Y.; Lefevre, C.; Greneche, J. M.; Toumi, M.; Mhiri, T.; Begin-Colin, S., Magnetic Iron Oxide Nanoparticles: Reproducible Tuning of the Size and Nanosized-Dependent Composition, Defects, and Spin Canting. *Journal of Physical Chemistry C* **2014**, *118* (7), 3795-3810.
143. Lalatonne, Y.; Paris, C.; Serfaty, J. M.; Weinmann, P.; Lecouvey, M.; Motte, L., Bis-phosphonates - ultra small superparamagnetic iron oxide nanoparticles: a platform towards diagnosis and therapy. *Chemical Communications* **2008**, (22), 2553-2555.
144. Feng, B.; Hong, R. Y.; Wang, L. S.; Guo, L.; Li, H. Z.; Ding, J.; Zheng, Y.; Wei, D. G., Synthesis of Fe₃O₄/APTES/PEG diacid functionalized magnetic nanoparticles for MR imaging. *Colloids and Surfaces a-Physicochemical and Engineering Aspects* **2008**, *328* (1-3), 52-59.
145. Wei, H.; Insin, N.; Lee, J.; Han, H. S.; Cordero, J. M.; Liu, W. H.; Bawendi, M. G., Compact Zwitterion-Coated Iron Oxide Nanoparticles for Biological Applications. *Nano Letters* **2012**, *12* (1), 22-25.

146. Wei, H.; Bruns, O. T.; Chen, O.; Bawendi, M. G., Compact zwitterion-coated iron oxide nanoparticles for in vitro and in vivo imaging. *Integrative Biology* **2013**, *5* (1), 108-114.
147. Sahoo, Y.; Pizem, H.; Fried, T.; Golodnitsky, D.; Burstein, L.; Sukenik, C. N.; Markovich, G., Alkyl phosphonate/phosphate coating on magnetite nanoparticles: A comparison with fatty acids. *Langmuir* **2001**, *17* (25), 7907-7911.
148. Yee, C.; Kataby, G.; Ulman, A.; Prozorov, T.; White, H.; King, A.; Rafailovich, M.; Sokolov, J.; Gedanken, A., Self-assembled monolayers of alkanesulfonic and -phosphonic acids on amorphous iron oxide nanoparticles. *Langmuir* **1999**, *15* (21), 7111-7115.
149. Wang, Y. F.; Zeiri, O.; Neyman, A.; Stellacci, F.; Weinstock, I. A., Nucleation and Island Growth of Alkanethiolate Ligand Domains on Gold Nanoparticles. *Acs Nano* **2012**, *6* (1), 629-640.
150. Smith, A. M.; Johnston, K. A.; Crawford, S. E.; Marbella, L. E.; Millstone, J. E., Ligand density quantification on colloidal inorganic nanoparticles. *Analyst* **2017**, *142* (1), 11-29.
151. Demers, L. M.; Mirkin, C. A.; Mucic, R. C.; Reynolds, R. A.; Letsinger, R. L.; Elghanian, R.; Viswanadham, G., A fluorescence-based method for determining the surface coverage and hybridization efficiency of thiol-capped oligonucleotides bound to gold thin films and nanoparticles. *Analytical Chemistry* **2000**, *72* (22), 5535-5541.
152. Davis, K.; Cole, B.; Ghelardini, M.; Powell, B. A.; Mefford, O. T., Quantitative Measurement of Ligand Exchange with Small-Molecule Ligands on Iron Oxide Nanoparticles via Radioanalytical Techniques. *Langmuir* **2016**, *32* (51), 13716-13727.
153. Maurizi, L.; Bisht, H.; Bouyer, F.; Millot, N., Easy Route to Functionalize Iron Oxide Nanoparticles via Long-Term Stable Thiol Groups. *Langmuir* **2009**, *25* (16), 8857-8859.
154. Maltas, E.; Ertekin, B., Binding of actin to thioglycolic acid modified superparamagnetic nanoparticles for antibody conjugation. *International Journal of Biological Macromolecules* **2015**, *72*, 984-989.
155. Chung, Y. C.; Huang, J. Y., Water-borne composite coatings using nanoparticles modified with dopamine derivatives. *Thin Solid Films* **2014**, *570*, 376-382.
156. Cowger, T. A.; Tang, W.; Zhen, Z. P.; Hu, K.; Rink, D. E.; Todd, T. J.; Wang, G. D.; Zhang, W. Z.; Chen, H. M.; Xie, J., Casein-Coated Fe₃O₂ Nanoparticles with Superior r(2) Relaxivity for Liver-Specific Magnetic Resonance Imaging. *Theranostics* **2015**, *5* (11), 1225-1232.
157. Huang, C. J.; Wang, L. C., Bio-inspired multifunctional catecholic assembly for photo-programmable biointerface. *Colloids and Surfaces B-Biointerfaces* **2015**, *134*, 247-253.
158. Huang, C. J.; Wang, L. C.; Shyue, J. J.; Chang, Y. C., Developing Antifouling Biointerfaces Based on Bioinspired Zwitterionic Dopamine through pH-Modulated Assembly. *Langmuir* **2014**, *30* (42), 12638-12646.
159. Kostevsek, N.; Sturm, S.; Sersa, I.; Sepe, A.; Bloemen, M.; Verbiest, T.; Kobe, S.; Rozman, K. Z., "Single-" and "multi-core" FePt nanoparticles: from controlled synthesis

- via zwitterionic and silica bio-functionalization to MRI applications. *Journal of Nanoparticle Research* **2015**, *17* (12).
160. Mondini, S.; Leonzino, M.; Drago, C.; Ferretti, A. M.; Usseglio, S.; Maggioni, D.; Tornese, P.; Chini, B.; Ponti, A., Zwitterion-Coated Iron Oxide Nanoparticles: Surface Chemistry and Intracellular Uptake by Hepatocarcinoma (HepG2) Cells. *Langmuir* **2015**, *31* (26), 7381-7390.
161. Sim, S.; Miyajima, D.; Niwa, T.; Taguchi, H.; Aida, T., Tailoring Micrometer-Long High-Integrity 1D Array of Superparamagnetic Nanoparticles in a Nanotubular Protein Jacket and Its Lateral Magnetic Assembling Behavior. *Journal of the American Chemical Society* **2015**, *137* (14), 4658-4661.
162. Zhou, Z. J.; Liu, H. Y.; Chi, X. Q.; Chen, J. H.; Wang, L. R.; Sun, C. J.; Chen, Z.; Gao, J. H., A Protein-Corona-Free T-1-T-2 Dual-Modal Contrast Agent for Accurate Imaging of Lymphatic Tumor Metastasis. *Acs Applied Materials & Interfaces* **2015**, *7* (51), 28286-28293.
163. Zhou, Z. J.; Wang, L. R.; Chi, X. Q.; Bao, J. F.; Yang, L. J.; Zhao, W. X.; Chen, Z.; Wang, X. M.; Chen, X. Y.; Gao, J. H., Engineered Iron-Oxide-Based Nanoparticles as Enhanced T-1 Contrast Agents for Efficient Tumor Imaging. *Acs Nano* **2013**, *7* (4), 3287-3296.
164. Zhou, Z. J.; Wu, C. Q.; Liu, H. Y.; Zhu, X. L.; Zhao, Z. H.; Wang, L. R.; Xu, Y.; Ai, H.; Gao, J. H., Surface and Interfacial Engineering of Iron Oxide Nanoplates for Highly Efficient Magnetic Resonance Angiography. *Acs Nano* **2015**, *9* (3), 3012-3022.
165. Lopez-Cruz, A.; Barrera, C.; Calero-DdelC, V. L.; Rinaldi, C., Water dispersible iron oxide nanoparticles coated with covalently linked chitosan. *Journal of Materials Chemistry* **2009**, *19* (37), 6870-6876.
166. De La Cruz-Montoya, E.; Rinaldi, C., Influence of Nanoparticle Surface Chemistry on the Thermomechanical and Magnetic Properties of Ferromagnetic Nanocomposites. *Journal of Polymer Science Part B-Polymer Physics* **2011**, *49* (16), 1163-1172.
167. Monsalve, A.; Bohorquez, A. C.; Rinaldi, C.; Dobson, J., Remotely Triggered Activation of TGF-beta With Magnetic Nanoparticles. *Ieee Magnetism Letters* **2015**, *6*.
168. Barrera, C.; Herrera, A. P.; Rinaldi, C., Colloidal dispersions of monodisperse magnetite nanoparticles modified with poly(ethylene glycol). *Journal of Colloid and Interface Science* **2009**, *329* (1), 107-113.
169. Neves, H. R.; Bini, R. A.; Barbosa, J. H. O.; Salmon, C. E. G.; Varanda, L. C., Dextran-Coated Antiferromagnetic MnO Nanoparticles for a T-1-MRI Contrast Agent with High Colloidal Stability. *Particle & Particle Systems Characterization* **2016**, *33* (3), 167-176.
170. Chatrabhuti, S.; Chirachanchai, S., Single step coupling for multi-responsive water-based chitin/chitosan magnetic nanoparticles. *Carbohydrate Polymers* **2013**, *97* (2), 441-450.
171. Qi, Y.; Shao, C.; Gu, W.; Li, F.; Deng, Y.; Li, H.; Ye, L., Carboxylic silane-exchanged manganese ferrite nanoclusters with high relaxivity for magnetic resonance imaging. *Journal of Materials Chemistry B* **2013**, *1* (13), 1846-1851.

172. Trekker, J.; Jans, K.; Damm, H.; Mertens, D.; Nuytten, T.; Vanacken, J.; Moshchalkov, V.; D'Haen, J.; Stakenborg, T.; Van Roy, W.; Himmelreich, U.; Lagae, L., Synthesis of PEGylated Magnetic Nanoparticles With Different Core Sizes. *Ieee Transactions on Magnetics* **2013**, *49* (1), 219-226.
173. Carron, S.; Bloemen, M.; Elst, L. V.; Laurent, S.; Verbiest, T.; Parac-Vogt, T. N., Potential theranostic and multimodal iron oxide nanoparticles decorated with rhenium-bipyridine and -phenanthroline complexes. *Journal of Materials Chemistry B* **2015**, *3* (21), 4370-4376.
174. Georgiadou, V.; Dendrinou-Samara, C., Impact of the Presence of Octadecylamine on the Properties of Hydrothermally Prepared CoFe₂O₄ Nanoparticles. *European Journal of Inorganic Chemistry* **2014**, (23), 3645-3656.
175. Iatridi, Z.; Georgiadou, V.; Menelaou, M.; Dendrinou-Samara, C.; Bokias, G., Application of hydrophobically modified water-soluble polymers for the dispersion of hydrophobic magnetic nanoparticles in aqueous media. *Dalton Transactions* **2014**, *43* (23), 8633-8643.
176. Albero, J.; Riente, P.; Clifford, J. N.; Pericas, M. A.; Palomares, E., Improving CdSe Quantum Dot/Polymer Solar Cell Efficiency Through the Covalent Functionalization of Quantum Dots: Implications in the Device Recombination Kinetics. *Journal of Physical Chemistry C* **2013**, *117* (26), 13374-13381.
177. Mauricio, M. R.; de Barros, H. R.; Guilherme, M. R.; Radovanovic, E.; Rubira, A. F.; de Carvalho, G. M., Synthesis of highly hydrophilic magnetic nanoparticles of Fe₃O₄ for potential use in biologic systems. *Colloids and Surfaces a-Physicochemical and Engineering Aspects* **2013**, *417*, 224-229.
178. Vamvakidis, K.; Katsikini, M.; Vourlias, G.; Angelakeris, M.; Paloura, E. C.; Dendrinou-Samara, C., Composition and hydrophilicity control of Mn-doped ferrite (Mn_xFe_{3-x}O₄) nanoparticles induced by polyol differentiation. *Dalton Transactions* **2015**, *44* (12), 5396-5406.
179. Shao, C.; Li, S.; Gu, W.; Gong, N.; Zhang, J.; Chen, N.; Shi, X.; Ye, L., Multifunctional Gadolinium-Doped Manganese Carbonate Nanoparticles for Targeted MR/Fluorescence Imaging of Tiny Brain Gliomas. *Analytical Chemistry* **2015**, *87* (12), 6251-6257.
180. Li, S.; Shao, C.; Gu, W.; Wang, R.; Zhang, J.; Lai, J.; Li, H.; Ye, L., Targeted imaging of brain gliomas using multifunctional Fe₃O₄/MnO nanoparticles. *Rsc Advances* **2015**, *5* (42), 33639-33645.
181. Jiang, Z.-Q.; Song, S.; Dou, H.-J.; Sun, K.; Wang, Y.-M.; Huang, C.-F.; Wei, Z.-H.; Qu, G.-X., Synthesis of Polycarboxylic Ligand Capped Fe₃O₄ Nanoparticles with Excellent Water-dispersibility via a Ligand-exchange Approach. *Chemical Journal of Chinese Universities-Chinese* **2012**, *33* (12), 2609-2616.
182. Zhu, R.; Luo, K.; Xu, X.; Wu, Y.; He, B.; Gu, Z., Poly(L-glutamic acid) dendron based pH sensitive drug carrier with magnetic nanoparticle core. *Acta Polymerica Sinica* **2011**, (6), 679-686.
183. Wang, W.; Dong, H.; Pacheco, V.; Willbold, D.; Zhang, Y.; Offenhaeusser, A.; Hartmann, R.; Weirich, T. E.; Ma, P.; Krause, H.-J.; Gu, Z., Relaxation Behavior Study

- of Ultrasmall Superparamagnetic Iron Oxide Nanoparticles at Ultralow and Ultrahigh Magnetic Fields. *Journal of Physical Chemistry B* **2011**, *115* (49), 14789-14793.
184. Chen, Z. P.; Xu, R. Z.; Zhang, Y.; Gu, N., Effects of Proteins from Culture Medium on Surface Property of Silanes- Functionalized Magnetic Nanoparticles. *Nanoscale Research Letters* **2009**, *4* (3), 204-209.
185. Palma, S. I. C. J.; Carvalho, A.; Silva, J.; Martins, P.; Marciello, M.; Fernandes, A. R.; del Puerto Morales, M.; Roque, A. C. A., Covalent coupling of gum arabic onto superparamagnetic iron oxide nanoparticles for MRI cell labeling: physicochemical and in vitro characterization. *Contrast Media & Molecular Imaging* **2015**, *10* (4), 320-328.
186. Menelaou, M.; Georgoula, K.; Simeonidis, K.; Dendrinou-Samara, C., Evaluation of nickel ferrite nanoparticles coated with oleylamine by NMR relaxation measurements and magnetic hyperthermia. *Dalton Transactions* **2014**, *43* (9), 3626-3636.
187. Varganici, C.-D.; Durdureanu-Angheluta, A.; Rosu, D.; Pinteala, M.; Simionescu, B. C., Thermal degradation of magnetite nanoparticles with hydrophilic shell. *Journal of Analytical and Applied Pyrolysis* **2012**, *96*, 63-68.
188. Gyergyek, S.; Drofenik, M.; Makovec, D., The Magnetic and Colloidal Properties of CoFe₂O₄ Nanoparticles Synthesized by Co-precipitation. *Acta Chimica Slovenica* **2014**, *61* (3), 488-496.
189. Nap, R. J.; Park, Y.; Wong, J. Y.; Szleifer, I., Adsorption of Acid and Polymer Coated Nanoparticles: A Statistical Thermodynamics Approach. *Langmuir* **2013**, *29* (47), 14482-14493.
190. Dan, M.; Scott, D. F.; Hardy, P. A.; Wydra, R. J.; Hilt, J. Z.; Yokel, R. A.; Bae, Y., Block Copolymer Cross-Linked Nanoassemblies Improve Particle Stability and Biocompatibility of Superparamagnetic Iron Oxide Nanoparticles. *Pharmaceutical Research* **2013**, *30* (2), 552-561.
191. Hardiansyah, A.; Huang, L.-Y.; Yang, M.-C.; Liu, T.-Y.; Tsai, S.-C.; Yang, C.-Y.; Kuo, C.-Y.; Chan, T.-Y.; Zou, H.-M.; Lian, W.-N.; Lin, C.-H., Magnetic liposomes for colorectal cancer cells therapy by high-frequency magnetic field treatment. *Nanoscale Research Letters* **2014**, *9*.
192. Bellusci, M.; Aliotta, C.; Fiorani, D.; La Barbera, A.; Padella, F.; Peddis, D.; Pilloni, M.; Secci, D., Manganese iron oxide superparamagnetic powder by mechanochemical processing. Nanoparticles functionalization and dispersion in a nanofluid. *Journal of Nanoparticle Research* **2012**, *14* (6).
193. Vardhan, P. V.; Suganthi, K. S.; Manikandan, S.; Rajan, K. S., Nanoparticle Clustering Influences Rheology and Thermal Conductivity of Nano-Manganese Ferrite Dispersions in Ethylene Glycol and Ethylene Glycol-Water Mixture. *Nanoscience and Nanotechnology Letters* **2014**, *6* (12), 1095-1101.
194. Aishwarya, V.; Suganthi, K. S.; Rajan, K. S., Transport properties of nano manganese ferrite-propylene glycol dispersion (nanofluids): new observations and discussion. *Journal of Nanoparticle Research* **2013**, *15* (7).
195. Nawara, K.; Romiszewski, J.; Kijewska, K.; Szczytko, J.; Twardowski, A.; Mazur, M.; Kryszinski, P., Adsorption of Doxorubicin onto Citrate-Stabilized Magnetic Nanoparticles. *Journal of Physical Chemistry C* **2012**, *116* (9), 5598-5609.

196. Park, Y.; Whitaker, R. D.; Nap, R. J.; Paulsen, J. L.; Mathiyazhagan, V.; Doerr, L. H.; Song, Y.-Q.; Huerlimann, M. D.; Szleifer, I.; Wong, J. Y., Stability of Superparamagnetic Iron Oxide Nanoparticles at Different pH Values: Experimental and Theoretical Analysis. *Langmuir* **2012**, *28* (15), 6246-6255.
197. Lin, J.-F.; Tsai, C.-C.; Lee, M.-Z., Linear birefringence and dichroism in citric acid coated Fe₃O₄ magnetic nanoparticles. *Journal of Magnetism and Magnetic Materials* **2014**, *372*, 147-158.
198. Lin, J. F.; Sheu, J. J., Modeling and prediction of retardance in citric acid coated ferrofluid using artificial neural network. *Journal of Magnetism and Magnetic Materials* **2016**, *407*, 201-208.
199. Palma, S. I. C. J.; Rodrigues, C. A. V.; Carvalho, A.; del Puerto Morales, M.; Freitas, F.; Fernandes, A. R.; Cabral, J. M. S.; Roque, A. C. A., A value-added exopolysaccharide as a coating agent for MRI nanoprobe. *Nanoscale* **2015**, *7* (34), 14272-14283.
200. Chiappi, M.; Javier Conesa, J.; Pereiro, E.; Sanchez Sorzano, C. O.; Josefa Rodriguez, M.; Henzler, K.; Schneider, G.; Javier Chichon, F.; Carrascosa, J. L., Cryo-soft X-ray tomography as a quantitative three-dimensional tool to model nanoparticle:cell interaction. *Journal of Nanobiotechnology* **2016**, *14*.
201. Oh, Y.; Lee, N.; Kang, H. W.; Oh, J., In vitro study on apoptotic cell death by effective magnetic hyperthermia with chitosan-coated MnFe₂O₄. *Nanotechnology* **2016**, *27* (11).
202. Lee, J.-H.; Huh, Y.-M.; Jun, Y.-w.; Seo, J.-w.; Jang, J.-t.; Song, H.-T.; Kim, S.; Cho, E.-J.; Yoon, H.-G.; Suh, J.-S.; Cheon, J., Artificially engineered magnetic nanoparticles for ultra-sensitive molecular imaging. *Nature Medicine* **2007**, *13* (1), 95-99.
203. Kim, D.-H.; Tamada, Y.; Ono, T.; Bader, S. D.; Rozhkova, E. A.; Novosad, V., The Effect of Ligands on FePt-Fe₃O₄ Core-Shell Magnetic Nanoparticles. *Journal of Nanoscience and Nanotechnology* **2014**, *14* (3), 2648-2652.
204. Roca, A. G.; Veintemillas-Verdaguer, S.; Port, M.; Robic, C.; Serna, C. J.; Morales, M. P., Effect of nanoparticle and aggregate size on the relaxometric properties of MR contrast agents based on high quality magnetic nanoparticles. *Journal of Physical Chemistry B* **2009**, *113*, 7033-7039.
205. Qi, M.; Zhang, K.; Li, S.; Wu, J.; Pham-Huy, C.; Diao, X.; Xiao, D.; He, H., Superparamagnetic Fe₃O₄ nanoparticles: synthesis by a solvothermal process and functionalization for a magnetic targeted curcumin delivery system. *New Journal of Chemistry* **2016**, *40* (5), 4480-4491.
206. Gutierrez, L.; Mejias, R.; Lazaro, F. J.; Serna, C. J.; Barber, D. F.; Puerto Morales, M., Effect of Anesthesia on Magnetic Nanoparticle Biodistribution After Intravenous Injection. *Ieee Transactions on Magnetism* **2013**, *49* (1), 398-401.
207. Hu, L.; de Montferrand, C.; Lalatonne, Y.; Motte, L.; Brioude, A., Effect of Cobalt Doping Concentration on the Crystalline Structure and Magnetic Properties of Monodisperse Co_xFe_{3-x}O₄ Nanoparticles within Nonpolar and Aqueous Solvents. *Journal of Physical Chemistry C* **2012**, *116* (7), 4349-4355.
208. Muscas, G.; Singh, G.; Glomm, W. R.; Mathieu, R.; Kumar, P. A.; Concas, G.; Agostinelli, E.; Peddis, D., Tuning the Size and Shape of Oxide Nanoparticles by

- Controlling Oxygen Content in the Reaction Environment: Morphological Analysis by Aspect Maps. *Chemistry of Materials* **2015**, 27 (6), 1982-1990.
209. Cheng, Q.; Li, Y.; Liu, S.; Sui, J.; Cai, W., Synthesis of a novel bifunctional nanocomposite with tunable upconversion emission and magnetic properties. *Rsc Advances* **2015**, 5 (113), 93547-93553.
210. Chen, L.; Zhou, Q.; Xiong, Q.; Li, W.; Liu, J.; Yang, X., Shape-Evolution and Growth Mechanism of Fe₃O₄ Polyhedrons. *Advances in Materials Science and Engineering* **2015**.
211. Chen, J.; Duncan, B.; Wang, Z.; Wang, L.-S.; Rotello, V. M.; Nugen, S. R., Bacteriophage-based nanoprobe for rapid bacteria separation. *Nanoscale* **2015**, 7 (39), 16230-16236.
212. Yang, W.; Yu, Y.; Wang, L.; Yang, C.; Li, H., Controlled synthesis and assembly into anisotropic arrays of magnetic cobalt-substituted magnetite nanocubes. *Nanoscale* **2015**, 7 (7), 2877-2882.
213. Tadic, M.; Kralj, S.; Jagodic, M.; Hanzel, D.; Makovec, D., Magnetic properties of novel superparamagnetic iron oxide nanoclusters and their peculiarity under annealing treatment. *Applied Surface Science* **2014**, 322, 255-264.
214. Batool, A.; Kanwal, F.; Abbas, A.; Riaz, S.; Naseem, S., Novel Method to Synthesize Highly Conducting Polyaniline/Nickel Sulfide Nanocomposite Films and the Study of Their Structural, Magnetic, and Electrical Properties. *Ieee Transactions on Magnetics* **2014**, 50 (8).
215. Lartigue, L.; Oumzil, K.; Guari, Y.; Larionova, J.; Guerin, C.; Montero, J.-L.; Barragan-Montero, V.; Sangregorio, C.; Caneschi, A.; Innocenti, C.; Kalaivani, T.; Arosio, P.; Lascialfari, A., Water-Soluble Rhamnose-Coated Fe₃O₄ Nanoparticles. *Organic Letters* **2009**, 11 (14), 2992-2995.
216. Lartigue, L.; Innocenti, C.; Kalaivani, T.; Awwad, A.; Duque, M. d. M. S.; Guari, Y.; Larionova, J.; Guerin, C.; Montero, J.-L. G.; Barragan-Montero, V.; Arosio, P.; Lascialfari, A.; Gatteschi, D.; Sangregorio, C., Water-Dispersible Sugar-Coated Iron Oxide Nanoparticles. An Evaluation of their Relaxometric and Magnetic Hyperthermia Properties. *Journal of the American Chemical Society* **2011**, 133 (27), 10459-10472.
217. Paolini, A.; Guarch, C. P.; Ramos-Lopez, D.; de Lapuente, J.; Lascialfari, A.; Guari, Y.; Larionova, J.; Long, J.; Nano, R., Rhamnose-coated superparamagnetic iron-oxide nanoparticles: an evaluation of their in vitro cytotoxicity, genotoxicity and carcinogenicity. *Journal of Applied Toxicology* **2016**, 36 (4), 510-520.
218. Briceno, S.; Silva, P.; Bramer-Escamilla, W.; Zabala, J.; Alcalá, O.; Guari, Y.; Larionova, J.; Long, J., Magnetic water-soluble rhamnose-coated Mn₁-XCoXFe₂O₄ nanoparticles as potential heating agents for hyperthermia. *Biointerface Research in Applied Chemistry* **2015**, 5 (1), 910-915.
219. O'Brien, R. W.; Midmore, B. R.; Lamb, A.; Hunter, R. J., Electroacoustic studies of moderately concentrated colloidal suspensions. *Faraday Discussions* **1990**, 90, 301-312.
220. Teng, Z.; Li, J.; Yan, F.; Zhao, R.; Yang, W., Highly magnetizable superparamagnetic iron oxide nanoparticles embedded mesoporous silica spheres and

- their application for efficient recovery of DNA from agarose gel. *Journal of Materials Chemistry* **2009**, *19* (13), 1811-1815.
221. Ivanisevic, A.; McCumber, K. V.; Mirkin, C. A., Site-Directed Exchange Studies with Combinatorial Libraries of Nanostructures. *Journal of the American Chemical Society* **2002**, *124*, 11997-12001.
222. Baralia, G. G.; Duwez, A.-S.; Nysten, B.; Jonas, A. M., Kinetics of Exchange of Alkanethiol Monolayers Self-Assembled on Polycrystalline Gold. *Langmuir* **2005**, *21*, 6825-6829.
223. Hong, R.; Fernandez, J. M.; Nakade, H.; Arvizo, R.; Emrick, T.; Rotello, V. M., In situ observation of place exchange reactions of gold nanoparticles. Correlation of monolayer structure and stability. *Chem Commun (Camb)* **2006**, (22), 2347-9.
224. Chechik, V., Reduced Reactivity of Aged Au Nanoparticles in Ligand Exchange Reactions. *Journal of the American Chemical Society* **2004**, *126* (25), 7780-7781.
225. Kang, H. J.; Patra, S.; Das, J.; Aziz, A.; Jo, J.; Yang, H., Effect of aging on the electrocatalytic activity of gold nanoparticles. *Electrochemistry Communications* **2010**, *12* (9), 1245-1248.
226. Einaga, H.; Kiya, A., Effect of aging on the CO oxidation properties of copper manganese oxides prepared by hydrolysis-coprecipitation using tetramethyl ammonium hydroxide. *Reaction Kinetics Mechanisms and Catalysis* **2016**, *117* (2), 521-536.
227. Soler, M. A.; Lima, E. C.; da Silva, S. W.; Melo, T. F.; Pimenta, A. C.; Sinnecker, J. P.; Azevedo, R. B.; Garg, V. K.; Oliveira, A. C.; Novak, M. A.; Morais, P. C., Aging investigation of cobalt ferrite nanoparticles in low pH magnetic fluid. *Langmuir* **2007**, *23* (19), 9611-7.
228. Biber, M. V.; Afonso, M. D. S.; Stumm, W., The Coordination Chemistry of Weathering: IV. Inhibition of the Dissolution of Oxide Minerals. *Geochimica et Cosmochimica Acta* **1994**, *58* (9), 1999-2010.
229. Bondietti, G.; Sinniger, J.; Stumm, W., The Reactivity of Fe(III) (hydr)Oxides: Effects of Ligands in Inhibiting the Dissolution. *Colloids and Surfaces A: Physicochemical and Engineering Aspects* **1993**, *79*, 157-167.
230. Gallagher, K. J.; Feitknecht, W.; Mannweiler, U., Mechanism of oxidation of magnetite to γ -Fe₂O₃. *Nature* **1968**, *217*, 1118-1121.
231. Laurent, S.; Forge, D.; Port, M.; Roch, A.; Robic, C.; Vander Elst, L.; Muller, R. N., Magnetic iron oxide nanoparticles: synthesis, stabilization, vectorization, physicochemical characterizations, and biological applications. *Chemical Reviews* **2008**, *108*, 2064-2110.
232. David, I.; Welch, J. E., The oxidation of magnetite and related spinels. *Transactions of the Faraday Society* **1956**, *52*, 1642-1650.
233. Shebanova, O. N.; Lazor, P., Raman study of magnetite (Fe₃O₄): laser-induced thermal effects and oxidation. *Journal of Raman Spectroscopy* **2003**, *34*, 845-852.
234. Wang, C. M.; Baer, D. R.; Amonette, J. E.; Engelhard, M. H.; Antony, J.; Qiang, Y., Morphology and Electronic Structure of the Oxide Shell on the Surface of Iron Nanoparticles. *Journal of the American Chemical Society* **2009**, *131* (25), 8824-8832.
235. Rebodos, R. L.; Vikesland, P. J., Effects of Oxidation on the Magnetization of Nanoparticulate Magnetite. *Langmuir* **2010**, *26* (22), 16745-16753.

236. Kandasamy, G.; Maity, D., Recent advances in superparamagnetic iron oxide nanoparticles (SPIONs) for in vitro and in vivo cancer nanotheranostics. *International Journal of Pharmaceutics* **2015**, *496* (2), 191-218.
237. daCosta, G. M.; DeGrave, E.; deBakker, P. M. A.; Vandenberghe, R. E., Influence of nonstoichiometry and the presence of maghemite on the Mossbauer spectrum of magnetite. *Clays and Clay Minerals* **1995**, *43* (6), 656-668.
238. Ravi, V.; Binz, J. M.; Rioux, R. M., Thermodynamic Profiles at the Solvated Inorganic-Organic Interface: The Case of Gold-Thiolate Monolayers. *Nano Letters* **2013**, *13* (9), 4442-4448.
239. Donkers, R. L.; Song, Y.; Murray, R. W., Substituent effects on the exchange dynamics of ligands on 1.6 nm diameter gold nanoparticles. *Langmuir* **2004**, *20* (11), 4703-4707.
240. Pazik, R.; Andersson, R.; Kepinski, L.; Nedelec, J. M.; Kessler, V. G.; Seisenbaeva, G. A., Surface Functionalization of the Metal Oxide Nanoparticles with Biologically Active Molecules Containing Phosphonate Moieties. Case Study of BaTiO₃. *Journal of Physical Chemistry C* **2011**, *115* (20), 9850-9860.
241. Woehrle, G. H.; Brown, L. O.; Hutchison, J. E., Thiol-functionalized, 1.5-nm gold nanoparticles through ligand exchange reactions: Scope and mechanism of ligand exchange. *Journal of the American Chemical Society* **2005**, *127* (7), 2172-2183.
242. Troiano, J. M.; Olenick, L. L.; Kuech, T. R.; Melby, E. S.; Hu, D. H.; Lohse, S. E.; Mensch, A. C.; Dogangun, M.; Vartanian, A. M.; Torelli, M. D.; Ehimiaghe, E.; Walter, S. R.; Fu, L.; Anderton, C. R.; Zhu, Z. H.; Wang, H. F.; Orr, G.; Murphy, C. J.; Hamers, R. J.; Pedersen, J. A.; Geiger, F. M., Direct Probes of 4 nm Diameter Gold Nanoparticles Interacting with Supported Lipid Bilayers. *Journal of Physical Chemistry C* **2015**, *119* (1), 534-546.
243. Almajano, M. P.; Carbo, R.; Delgado, M. E.; Gordon, M. H., Effect of pH on the antimicrobial activity and oxidative stability of oil-in-water emulsions containing caffeic acid. *Journal of Food Science* **2007**, *72* (5), C258-C263.
244. Wang, B.; Cheng, X. H., Enhancement of binding kinetics on affinity substrates by laser point heating induced transport. *Analyst* **2016**, *141* (5), 1807-1813.
245. Mulvihill, M. J.; Habas, S. E.; Jen-La Plante, H.; Wan, J. M.; Mokari, T., Influence of Size, Shape, and Surface Coating on the Stability of Aqueous Suspensions of CdSe Nanoparticles. *Chemistry of Materials* **2010**, *22* (18), 5251-5257.
246. Hong, R.; Fernandez, J. M.; Nakade, H.; Arvizo, R.; Emrick, T.; Rotello, V. M., In situ observation of place exchange reactions of gold nanoparticles. Correlation of monolayer structure and stability. *Chemical Communications* **2006**, (22), 2347-2349.
247. Martell, A. E.; Smith, R. M., *Critical Stability Constants*. Plenum Press: New York, 1977; Vol. 3.
248. Guo, R.; Murray, R. W., Substituent effects on redox potentials and optical gap energies of molecule-like Au-38(SPhX)(24) nanoparticles. *Journal of the American Chemical Society* **2005**, *127* (34), 12140-12143.
249. Abellan-Pose, R.; Rodriguez-Evora, M.; Vicente, S.; Csaba, N.; Evora, C.; Alonso, M. J.; Delgado, A., Biodistribution of radiolabeled polyglutamic acid and PEG-

- polyglutamic acid nanocapsules. *European Journal of Pharmaceutics and Biopharmaceutics* **2017**, *112*, 155-163.
250. Harrington, K. J.; Mohammadtaghi, S.; Uster, P. S.; Glass, D.; Peters, A. M.; Vile, R. G.; Stewart, J. S. W., Effective targeting of solid tumors in patients with locally advanced cancers by radiolabeled pegylated liposomes. *Clinical Cancer Research* **2001**, *7* (2), 243-254.
251. Jauhar, S.; Kaur, J.; Goyal, A.; Singhal, S., Tuning the properties of cobalt ferrite: a road towards diverse applications. *Rsc Advances* **2016**, *6* (100), 97694-97719.
252. de los Reyes, M.; Majewski, P. J.; Scales, N.; Luca, V., Hydrolytic Stability of Mesoporous Zirconium Titanate Frameworks Containing Coordinating Organic Functionalities. *Acs Applied Materials & Interfaces* **2013**, *5* (10), 4120-4128.
253. D'Souza, A. A.; Shegokar, R., Polyethylene glycol (PEG): a versatile polymer for pharmaceutical applications. *Expert Opinion on Drug Delivery* **2016**, *13* (9), 1257-1275.
254. Ikeda, Y.; Nagasaki, Y., PEGylation Technology in Nanomedicine. *Polymers in Nanomedicine* **2012**, *247*, 115-140.
255. Joralemon, M. J.; McRae, S.; Emrick, T., PEGylated polymers for medicine: from conjugation to self-assembled systems. *Chemical Communications* **2010**, *46* (9), 1377-1393.
256. Harris, J. M.; Martin, N. E.; Modi, M., Pegylation - A novel process for modifying pharmacokinetics. *Clinical Pharmacokinetics* **2001**, *40* (7), 539-551.
257. Swierczewska, M.; Lee, K. C.; Lee, S., What is the future of PEGylated therapies? *Expert Opinion on Emerging Drugs* **2015**, *20* (4), 531-536.
258. Ratner, B. D.; Bryant, S. J., Biomaterials: Where we have been and where we are going. *Annual Review of Biomedical Engineering* **2004**, *6*, 41-75.
259. Li, Z.; Xing, D.; Wang, C.; Xin, Y.; Liu, J.; Sun, Z., RECENT PROGRESS IN APPLICATION OF PEGYLATED NANOCARRIERS FOR ANTITUMOR DRUG DELIVERY SYSTEMS. *Drugs of the Future* **2016**, *41* (3), 177-184.
260. Jevsevar, S.; Kunstelj, M., Half-Life Extension through PEGylation. In *Therapeutic Proteins: Strategies to Modulate their Plasma Half-Lives*, Kontermann, R., Ed. Wiley-Blackwell: Weinheim, Germany, 2012; p 22.
261. Huang, Y.; Havert, M.; Gavin, D.; Serabian, M.; Ong, L. L.; McIntyre, M. C.; Ferry, N.; Kume, A.; Petrin, D.; Fu, Y. H.; Marti, A.; Oliveira, F.; Pavittranon, S.; Shin, W., Biodistribution studies: understanding international expectations. *Molecular Therapy-Methods & Clinical Development* **2016**, *3*.
262. Yang, K.; Zhang, S. A.; Zhang, G. X.; Sun, X. M.; Lee, S. T.; Liu, Z. A., Graphene in Mice: Ultrahigh In Vivo Tumor Uptake and Efficient Photothermal Therapy. *Nano Letters* **2010**, *10* (9), 3318-3323.
263. Choi, K. Y.; Min, K. H.; Yoon, H. Y.; Kim, K.; Park, J. H.; Kwon, I. C.; Choi, K.; Jeong, S. Y., PEGylation of hyaluronic acid nanoparticles improves tumor targetability in vivo. *Biomaterials* **2011**, *32* (7), 1880-1889.
264. Ballou, B.; Lagerholm, B. C.; Ernst, L. A.; Bruchez, M. P.; Waggoner, A. S., Noninvasive imaging of quantum dots in mice. *Bioconjugate Chemistry* **2004**, *15* (1), 79-86.

265. Schipper, M. L.; Iyer, G.; Koh, A. L.; Cheng, Z.; Ebenstein, Y.; Aharoni, A.; Keren, S.; Bentolila, L. A.; Li, J. Q.; Rao, J. H.; Chen, X. Y.; Banin, U.; Wu, A. M.; Sinclair, R.; Weiss, S.; Gambhir, S. S., Particle Size, Surface Coating, and PEGylation Influence the Biodistribution of Quantum Dots in Living Mice. *Small* **2009**, *5* (1), 126-134.
266. Xie, H. A.; Wang, Z. J.; Bao, A. D.; Goins, B.; Phillips, W. T., In vivo PET imaging and biodistribution of radiolabeled gold nanoshells in rats with tumor xenografts. *International Journal of Pharmaceutics* **2010**, *395* (1-2), 324-330.
267. Gabizon, A.; Horowitz, A. T.; Goren, D.; Tzemach, D.; Shmeeda, H.; Zalipsky, S., In vivo fate of folate-targeted polyethylene-glycol liposomes in tumor-bearing mice. *Clinical Cancer Research* **2003**, *9* (17), 6551-6559.
268. Guillaudeu, S. J.; Fox, M. E.; Haidar, Y. M.; Dy, E. E.; Szoka, F. C.; Frechet, J. M. J., PEGylated dendrimers with core functionality for biological applications. *Bioconjugate Chemistry* **2008**, *19* (2), 461-469.
269. Krauser, J. A., A perspective on tritium versus carbon-14: ensuring optimal label selection in pharmaceutical research and development. *Journal of Labelled Compounds & Radiopharmaceuticals* **2013**, *56* (9-10), 441-446.
270. Sonopo, M. S.; Venter, K.; Boyle, G.; Winks, S.; Marjanovic-Painter, B.; Zeevaart, J. R., Carbon-14 radiolabeling and in vivo biodistribution of a potential anti-TB compound. *Journal of Labelled Compounds & Radiopharmaceuticals* **2015**, *58* (2), 23-29.
271. Gifford, A. N.; Espaillat, M. P.; Gatley, S. J., Biodistribution of radiolabeled ethanol in rodents. *Drug Metabolism and Disposition* **2008**, *36* (9), 1853-1858.
272. Ambruosi, A.; Khalansky, A. S.; Yamamoto, H.; Gelperina, S. E.; Begley, D. J.; Kreuter, J., Biodistribution of polysorbate 80-coated doxorubicin-loaded C-14 - poly(butyl cyanoacrylate) nanoparticles after intravenous administration to glioblastoma-bearing rats. *Journal of Drug Targeting* **2006**, *14* (2), 97-105.
273. Calvo, P.; Gouritin, B.; Chacun, H.; Desmaele, D.; D'Angelo, J.; Noel, J. P.; Georgin, D.; Fattal, E.; Andreux, J. P.; Couvreur, P., Long-circulating PEGylated polycyanoacrylate nanoparticles as new drug carrier for brain delivery. *Pharmaceutical Research* **2001**, *18* (8), 1157-1166.
274. Peracchia, M. T.; Fattal, E.; Desmaele, D.; Besnard, M.; Noel, J. P.; Gomis, J. M.; Appel, M.; d'Angelo, J.; Couvreur, P., Stealth (R) PEGylated polycyanoacrylate nanoparticles for intravenous administration and splenic targeting. *Journal of Controlled Release* **1999**, *60* (1), 121-128.
275. Zhu, S. J.; Hong, M. H.; Tang, G. T.; Qian, L. L.; Lin, J. Y.; Jiang, Y. Y.; Pei, Y. Y., Partly PEGylated polyamidoamine dendrimer for tumor-selective targeting of doxorubicin: The effects of PEGylation degree and drug conjugation style. *Biomaterials* **2010**, *31* (6), 1360-1371.
276. Han, X. P.; Li, Z. B.; Sun, J.; Luo, C.; Li, L.; Liu, Y. H.; Du, Y. Q.; Qiu, S. H.; Ai, X. Y.; Wu, C. N.; Lian, H.; He, Z. G., Stealth CD44-targeted hyaluronic acid supramolecular nanoassemblies for doxorubicin delivery: Probing the effect of uncovalent pegylation degree on cellular uptake and blood long circulation. *Journal of Controlled Release* **2015**, *197*, 29-40.

277. Karukstis, K. K.; Thompson, E. H. Z.; Whiles, J. A.; Rosenfeld, R. J., Deciphering the fluorescence signature of daunomycin and doxorubicin. *Biophysical Chemistry* **1998**, *73* (3), 249-263.
278. Chen, A. M.; Zhang, M.; Wei, D. G.; Stueber, D.; Taratula, O.; Minko, T.; He, H. X., Co-delivery of Doxorubicin and Bcl-2 siRNA by Mesoporous Silica Nanoparticles Enhances the Efficacy of Chemotherapy in Multidrug-Resistant Cancer Cells. *Small* **2009**, *5* (23), 2673-2677.